Experimental investigation of a low pressure capacitively-coupled discharge

S. Kechkar

January 2015

PhD

Experimental investigation of a low pressure capacitively-coupled discharge

A thesis for the degree of

PHILOSOPHIAE DOCTOR

Presented to

DUBLIN CITY UNIVERSITY

By

Samir Kechkar. B.Sc
School of Physical Sciences
Dublin City University

Research Supervisors:
Dr Paul Swift
Dr Jim Conway

January 2015

Declaration

I hereby certify that this material, which I now submit for assessment on the programme of study leading to the award of Philosophiae of Doctorate is entirely my own work, that I have exercised reasonable care to ensure that the work is original, and does not to the best of my knowledge breach any law of copyright, and has not been taken from the work of others save and to the extent that such work has been cited and acknowledged within the text of my work.

Signed:_____ (Candidate) ID No.:_____ Date:_____

Acknowledgements

It is my pleasure to recognize some colleagues, friends and family who have made this work possible and supported me over the past few years. Firstly, I would like to thank Dr Paul Swift for much time and effort in supervising my research throughout the past few years. I would also like to thank Dr Jim Conway for co-supervising my PhD and for lots of encouragement and advice throughout my time at DCU. I am sincerely grateful to Dr Stephen Daniels and Prof Miles Turner since without their leadership my research opportunity at DCU would not be possible. In addition, I would like to thank many of my colleagues (past and present) such as Cezar, Bernard, Niall Mac Gearailt, Niall O'Connor, Nina, Sean, Aidan, Huw, Conor Murphy, Zhenning, Sharath, Guru, Sarvesh, Mubarak, Nishant, Yang, David Gahan, Conor Coyle and Chanel Hayden that have assisted me in any way over the past four years. Thanks to the administrative staff Samantha, Sheila, Lisa, Sarah, Fionna, Trish and Susan who have been very supportive to me during my time at DCU.

Much commitment, time and effort is required to complete a PhD, however, some 'time away' from plasma physics is also necessary; so I owe many thanks to friends such as Owen, Aidan, Davy, Darren, Mark, Kav, Colm, Alex, Simon and Philip and TEK United FC for providing an outlet for me for life outside work. I am particularly grateful to to my parents for much financial support throughout not just my PhD but my whole academic career. Last, and certainly not least, a special thanks goes to Emma for much support and encouragement throughout my PhD.

Contents

List of Figures

List of Symbols

T_e	electron temperature (K)	22
T_i	ion temperature (K)	22
T_g	gas temperature (K)	22
n_i	ion density (m^{-3})	26
n_e	electron density (m^{-3})	26
R	laser excitation rate (s^{-1})	37
A	fluorescence rate (s^{-1})	37
P	photo-ionization rate (s^{-1})	37
S	amplified spontaneous emission rate (s^{-1})	37
Q	collisional quenching rate (s^{-1})	37
C	rate of alternative excitation processes (s^{-1})	37
e	absolute electron charge ($\simeq 1.6022 \times 10^{-19}$ C)	76
E	electric field ($V{\cdot}m^{-1}$)	129
I_e	electron current (A)	76
I_i	positive ion current (A)	78

Abstract

In this thesis, a low-pressure, capacitively-coupled plasma (CCP) was investigated using the well established techniques of actinometry, two-photon laser-induced fluorescence (TALIF), appearance potential mass spectrometry (APMS), Langmuir and hairpin probes. The behaviour of atomic oxygen density in mixtures of O_2/SF_6 was investigated using TALIF and a Langmuir probe. A significant five-fold increase of [O] was observed when O_2 plasma was diluted with SF_6 (5 - 10%). This was attributed to a combination of a change in surface conditions and also due to a shift in the effective electron temperature, T_{eff}. It was found that T_{eff} dramatically increased from $\approx$ 1 to 8 eV as the SF_6 content varied from 0 - 60% which consequently resulted in a threefold increase in the atomic oxygen production rate. [O] increased by over a factor of three after fluorinating the walls with SF_6 plasma. Electron energy distribution functions, EEDFs, required for calculating excitation rate constants needed for actinometry were measured with a Langmuir probe. When compared to TALIF measurements; actinometry showed excellent quantitative agreement in pure O_2 plasma but did not predict the rapid rise of [O] with SF_6 addition and grossly overestimated [O] in O_2 plasma containing SF_6. However, reasonable qualitative agreement was shown for mixtures in the range of 10 to 60% SF_6.

A Langmuir probe was used to investigate various electron heating phenomena in O_2 and Ar plasmas. The so called '$\alpha - \gamma$' mode transition in O_2 plasma (100 mTorr) was identified from the power evolution (3 - 600 W) of the electron energy probability function (EEPF) electron density (n_e) and T_{eff}. The EEPF evolved from Druyvesteyn to bi-Maxwellian with increasing power which resulted in a rapid decrease and abrupt increase in T_{eff} and n_e respectively. Comparisons were made to the same mode transition for simi-

lar conditions in Ar plasma. Low energy electrons were effectively heated in Ar plasma when compared to O_2 plasma. This was unusual since Ar atoms have an abnormally low momentum transfer cross-section (Ramsauer effect) which does not favour collisional heating of low energy electrons. The pressure evolution of the EEPF, n_e, and T_{eff} was also investigated in O_2 plasma operated at 30 and 200 W. The number of high energy electrons decreased with increasing pressure (10 - 70 mTorr), however, high energy electrons were enhanced for pressures above 70 mTorr at 30 W and greater than 400 mTorr at 200 W. This behaviour is contrary to the inverse relationship between the ionization rate and gas density (particle balance). The mechanisms behind such unusual behaviour are still unknown and require further investigation. Although, structure was observed on the EEPFs which could indicate the presence of super-elastic collisions; a process which is known to enhance the tail of the EEPF.

Atomic fluorine density was measured in both SF_6/Ar (95/5%) and SF_6/O_2/Ar (85/10/5%) discharges using appearance potential mass spectrometry (APMS). The dissociation fraction, D, increased from 0.3×10^{-3} - 2.4×10^{-3} with increasing power (50 - 300 W) in SF_6/O_2/Ar plasma at 40 mTorr. D in SF_6/Ar plasma was over 22 times lower than in SF_6/O_2/Ar plasma. The presence of O_2 in the feedstock significantly enhanced [F] in the discharge. The F^+ signal increased by a factor of 60 when 10 % O_2 was added to SF_6 plasma, whereas, actinometry predicted only a threefold increase of [F]. Similarly, absolute [F] measured with APMS increased by a factor of 10 with increasing power in SF_6/O_2/Ar plasma whereas actinometry only showed a twofold increase. The comparison of these techniques showed that actinometry for measuring [F] was unreliable for the condition explored in this work.

CHAPTER 1

Introduction

Low temperature, non equilibrium plasmas are widely used for manufacturing of modern technologies. Such technological areas include integrated circuit (IC) manufacturing, material processing, lighting displays, plasma television displays, space physics (thrusters), sterilization and thin film deposition. Plasma processing for IC manufacturing requires materials modification by various mechanisms such as etching, deposition, sputtering, implantation and cleaning. The final outcome after many processes is nano-scale structures (transistors) that can range down to 14 nm in size. Up to as many as 50 plasma processing steps can be required to manufacture a typical microprocessor which in some cases contains up to 47 million transistors. Therefore the IC industry demands stable and reproducible plasmas used for such processes. Any plasma process drift e.g. variation of etch profile dimensions, induced by a shift in some key plasma parameters will often lead to a degra-

dation in the performance of the device. Many wafers need to be discarded depending on the severity of the process drift which is an expensive issue for the IC industry. Therefore, much interest surrounds plasma diagnostics which are used to achieve a greater understanding of processing plasmas and plasma-surface interactions. Such improvements are required for process optimization in order to meet the demand of tighter tolerances as transistor size continuously decreases in the IC industry.

A sensor that can be used to detect variation of key plasma parameters within wafer processing on an industrial plasma tool would be highly desirable in industry. The possibility of implementing real-time, closed loop control of plasma processes for reduction of plasma process variation could be realised with reliable sensors. An important topic discussed in this thesis is the development of a sensor that has such industrial application. The technique described here is optical actinometry, which is used to detect particle densities in particular atomic radicals which are an important plasma process parameter known to effect the outcome of a plasma process if significant variation occurs. The applicability of actinometry for detection of atomic oxygen and fluorine densities in mixtures of O_2/SF_6 and in $SF_6/O_2/Ar$ plasma is reported. In addition, the behavior of [O] and [F] as a function of various plasma operating conditions such as power, pressure, feedstock mixture was investigated with well established and reliable diagnostic techniques such as two-photon laser induced fluorescence spectroscopy (TALIF) and appearance potential mass spectrometry (APMS). Emphasis was placed on dominant production and loss mechanisms such as destruction via wall recombination and production by electron impact dissociation of the parent molecules.

Also discussed is the investigation of electron heating mechanisms which are

fundamental in sustaining the discharge. Such phenomena that were investigated were the $\alpha - \gamma$ mode transition and also the collisionless - collisional heating mode transition in both O_2 and Ar plasma with the use of a Langmuir probe. These mode transitions occur when the discharge operating conditions such as power and pressure are varied. Significant changes in the electron heating and ionization rates occurs, which, in turn effects the spatial dependence of electron plasma parameters and thus, the chemical reaction rates and surface processes that govern a plasma process.

1.1 The importance of the reactor walls

In plasma processing it is widely accepted that the prime cause of process drift is due to a change in the reactor wall conditions [1]. The important process (output) parameters that drift in IC manufacturing are critical dimension uniformity, selectivity, anisotropy and etch profile control (also known as bias). The chemical composition of the reactor walls can influence significantly the density of reactive species within the discharge. This is because the main loss mechanism for radicals is through wall recombination, therefore, a change in the surface chemistry will alter the probability of a surface reaction. Drift occurs within a plasma process when etch or deposition by-products form films on the reactor walls, which alter the gas-phase chemistry and species involved in etching a passivation.

An example of the significance of reactor wall conditions on radical densities has been reported by Cunge *et al* [2]. It was reported that the Cl mole fraction, [Cl]/([Cl]+[Cl_2]), in an inductively-coupled Cl_2 discharge for a fixed power and pressure in a 'clean reactor' was 0.40 but for a SiOCl coated reactor the Cl mole fraction was ≈ 0.95 and for a TiOCl coated reactor after

a metal gate etch process the Cl mole fraction was 0.25. This is a surprising result as for a given power and pressure it is possible for the plasma to be between $\approx$ 25 and 95 % dissociated depending on the chemical nature of the wall. The effects of a change in the wall conditions was investigated in this work by measuring the change in the density of either atomic oxygen or atomic fluorine as the reactor walls are either fluorinated or oxygenated.

1.2 Capacitively-coupled plasma (13.56 MHz)

A basic description of capacitively-coupled plasma (CCP) is outlined in this section. All work discussed in this report was carried out on a CCP source, a basic schematic of which is shown in figure 1.1. A capacitively-coupled plasma source generates plasma which is weakly ionized (fractional ionization of 10^{-6} - 10^{-3}) [3]. Low-pressure, electrically driven plasmas are almost never in thermal equilibrium. Typically, the ion temperature, T_i, and the gas temperature, T_g, are $\approx$ 0.03 - 0.05 eV while the electron temperature, T_e, $\approx$ 1 - 6 eV i.e. $T_i \approx T_g \ll T_e$ [3]. Electrons respond rapidly to varying electric fields and are referred to as 'hot'. CCP vacuum chambers are normally made from aluminium or stainless steel and consist of two parallel plate electrodes or alternatively, one electrode (plate) and the surrounding walls grounded. These reactors also have various orifices for gas transport and pressure sensors and are also equipped with vacuum ports for wafer delivery, optical and electrical access. During plasma operation, gas is flowed continuously into the reactor, regulated using mass flow controllers. Process by-products are then removed by vacuum pumps. Radio frequency (rf) power operated at 13.56 MHz is applied to one electrode and is often refereed to as the driven electrode or bias oscillator. The remaining electrode and surrounding walls

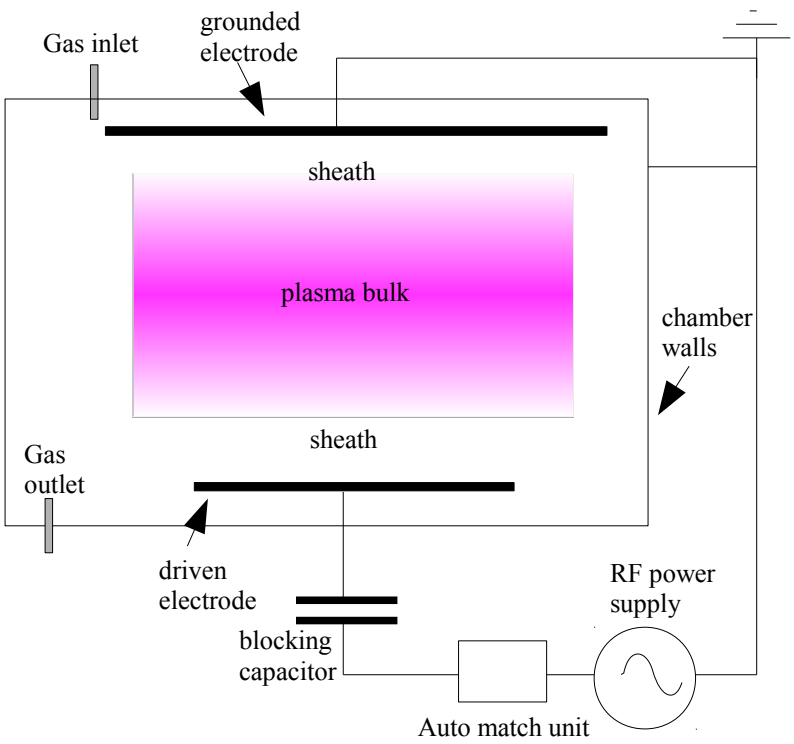

Figure 1.1: Basic capacitively-coupled plasma reactor

are grounded. The applied rf potential, $V_{rf}(t)$, on the electrode has the following form in time, t

$$V_{rf}(t) = \tilde{V}_{rf}\sin(\omega t) \tag{1.1}$$

where $\tilde{V}_{rf}$ is the amplitude of the rf voltage and ω is the angular frequency. A matching network is placed between the power supply and driven electrode. Its main function is to match the impedance of the load (reactor and plasma) to the 50 Ω impedance of the generator. This ensures maximum power transfer (efficiency $\approx$ 80 - 90 %) from the generator to the load, this matching network usually consists of two variable vacuum capacitors. The power system used in this work automatically tunes the capacitors to match

the impedance of the load with the power supply. CCP sources are often called reactive ion etchers (RIE) for the situations where the surface to be treated is placed on the powered electrode and if the electrodes are asymmetric which results in a significant fraction of the applied potential appearing across the powered electrode.

Plasma sources in the RIE configuration results in the simultaneous bombardment of reactive neutrals and energetic ions to the material being processed. This is desirable in cases where chemical etching by reactive species is inhibited without sufficient ion bombardment, this process is called ion-enhanced etching. For example, fluorocarbon films deposited on the process material in CHF_3 plasma can inhibit the chemical etch process by insufficient ion bombardment [4], a similar effect was found by Coburn and Winters with etching by XeF_2 plasma [5, 6]. Some common process gases used in RIE systems include O_2, SF_6, CF_4, HBr and Cl_2.

1.3 Sheath formation

A plasma is joined to the surrounding walls by positively charged layers called sheaths. A sheath forms near any surface in contact with plasma, it is a thin region of strong electric field which repel electrons and consist of positive ions. For now consider the case of an unbiased, perfectly adsorbing wall containing a quasineutral plasma. Quasineutrality means that the electron, n_e, and ion, n_i, number densities are almost equal ($n_e \approx n_i$). The thermal velocity of electrons is at least 100 times the ion thermal velocity since $T_e \gg T_i$ and also because the ion mass, M_i, is far greater than the electron mass, m_e. Initially the plasma is electrically neutral i.e. the electric potential is zero

everywhere due to quasineutrality. Therefore the electrons are not confined within the plasma and rapidly become lost to the surrounding walls. Similarly, ions are not confined to the bulk and are also lost to the walls. However, the flux of electrons to the walls far exceeds the flux of ions due to the higher electron mobility. The electrons lost to the surrounding walls leave the plasma with a positive potential known as the plasma potential, V_p. Figure 1.2 shows a schematic which illustrates the potential profile, $V(x)$ and the spatial profile of the charged species densities against distance from the electrode to the plasma. The potential of the walls is negative relative to the

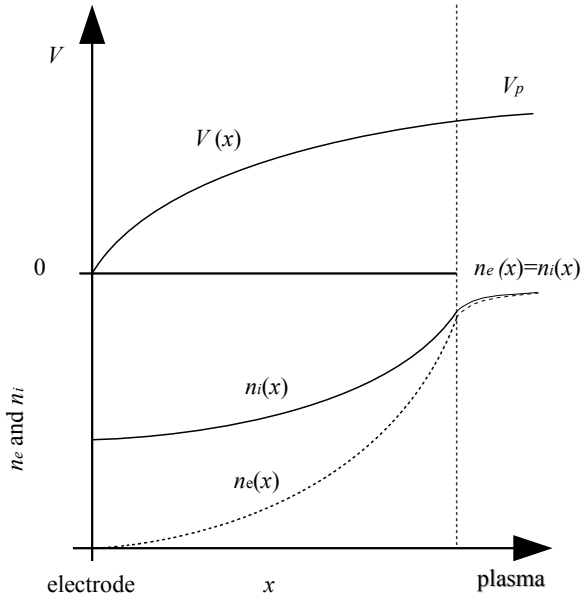

Figure 1.2: Spatial distributions of the potential and charge species density across the sheath.

plasma bulk, consequently, the electrons become repelled from the walls and

ions become attracted to the walls. A balanced condition is reached where the electrons and ions arrive to the walls at equal rates keeping the plasma quasineutral. Within the sheath, quasineutrality is violated and the sheath has net positive charge density and only the most energetic electrons enter the sheath, $n_i \gg n_e$. The potential of walls when this steady state of electron and ion flux is established is known as the floating potential, V_f. The imbalance of charged particles in the sheath region leads to potential profile that is positive within the plasma and decreases sharply towards the wall which is negative with respect to the plasma. A full theoretical description of sheaths is described by Lieberman and Lichtenburg [3].

1.4 Asymmetric CCP

The plasma system investigated in this work is a asymmetric CCP. Asymmetric CCP means that the electrodes are of unequal areas (where A_d and A_g are the areas of the driven and grounded electrode respectively). Typically $A_d \ll A_g$ because the chamber walls are also grounded. Consequently, the magnitude of the sheath potential is different for the driven electrode compared to the grounded electrode. As a result of this asymmetry a negative DC bias, V_{dc}, will be developed in front of the driven electrode which ensures equal loss of positive and negative charge at each electrode. The total potential on the driven electrode is then given by

$$V_{rf}(t) = \bar{V}_{dc} + \tilde{V}_{rf}\sin(\omega t) \tag{1.2}$$

and consequently, the plasma potential will also vary in time i.e. $V_p(t) = \bar{V}_p + \tilde{V}_p\sin(\omega t)$ where $\bar{V}_p$ is the time averaged plasma potential and $\tilde{V}_p$ is the amplitude of the RF component of the plasma potential. The sheath

potential, $V_{sh}(t)$, is defined as the potential difference between the plasma-sheath boundary and powered electrode and is given by

$$V_{sh}(t) = V_{rf}(t) - V_p(t) \tag{1.3}$$

Figure 1.3 shows a schematic of the time varying applied rf, driven sheath and bulk plasma potentials over two RF cycles in an asymmetric capacitively-coupled plasma, also shown is the constant dc bias on the driven electrode.

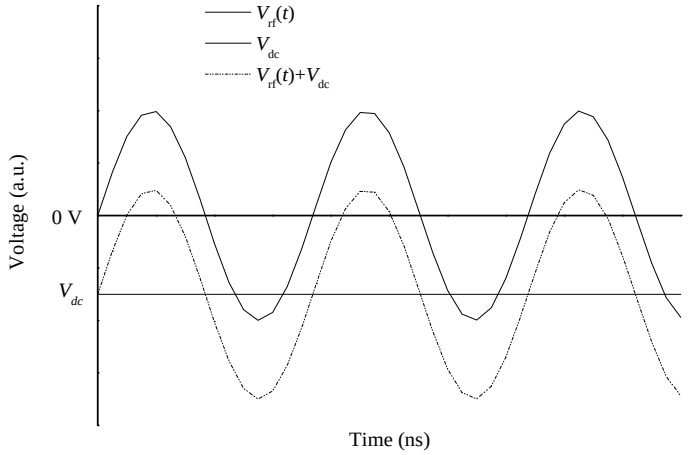

Figure 1.3: Time varying applied RF voltage, dc bias and total voltage on the driven electrode of an asymmetric capacitively-coupled plasma.

1.5 CCP operating modes

It is well established that electrons are responsible for sustaining or 'heating' the discharge due to their small mass and their ability to respond rapidly to electric fields and generate more charged particles through collisions with the background gas [3]. RF capacitive discharges can be sustained through several mechanisms which depend on electron interactions with the oscillating sheath at the plasma boundary, rf electric fields in the plasma bulk and

collisions with neutrals. These heating mechanisms depend significantly on various discharge operating conditions such as the electrode separation distance D, electrode material, gas pressure, applied rf potential, or applied power, P_{rf}, and the feedstock gas.

1.5.1 Alpha (α) mode

The alpha mode (α-mode) occurs when the main heating mechanism is achieved by interaction of low energy electrons with the bulk rf field. The electron momentum must be randomized with respect to the phase of the oscillating electric field for this process to occur and this is achieved by momentum transfer collisions with the background gas. Electrons will gain energy, i.e. be 'heated' by the rf field to enable ionization in order to sustain the discharge. This heating mechanism is called collisional heating or ohmic heating. The discharge is said to be in the α mode when the dominant heating mechanism is via collisional heating. For this mechanism to be dominant the electron neutral mean free path, λ_{en}, must be smaller than or comparable to the discharge dimensions i.e. $\lambda_{en} \leq D$. Therefore, the conditions which are favorable for collisional heating are moderate to higher pressures $\approx$ 0.06 - 1 Torr and low applied powers where the influence of secondary electrons is negligible. This α mode is typically characterized by a Druyvesteyn or Maxwellian EEPF, a low n_e i.e. $\approx 5\times10^{14}$ - $5\times10^{15}\mathrm{m}^{-3}$ and high T_{eff} i.e. $\approx$ 3.5 - 5.0 eV in the plasma bulk [7, 8].

1.5.2 Gamma (γ) mode

A second electron heating mechanism exists when a significant number of secondary electrons are injected into the discharge. As the applied power increases a significant fraction of this power is transferred into the ions which

are accelerated by the large electric field across the sheath and release secondary electrons (SE) upon transfer of kinetic energy onto the surface of the driven electrode. These SE are then accelerated by the oscillating sheath leading to significant ionization at the plasma-sheath boundary. More ions are produced by these SE which are again accelerated into the electrodes which produce more SE. An electron avalanche effect develops and consequently n_e increases abruptly. This is most significant at moderate to high pressures, i.e. 0.1 - 1 Torr, where the electron atom/molecule collision rate is sufficiently high to create an electron avalanche. In this regime the secondary electrons dominate the ionization balance and consequently the bulk rf electric field and electron temperature decreases to prevent further ionization. The discharge is said to be in the γ mode since the ionization occurs predominantly by SE. Low pressures do not favour the γ mode since the accelerated SE can either thermalize or escape from the discharge without a collision with a gas atom/molecule. The flux of the emitted SE, Γ_{se}, is proportional to the bombarding ion flux, Γ_i and the secondary electron emission coefficient, γ_{se}, which is specific to the electrode material i.e.

$$\Gamma_{se} = \gamma_{se}\Gamma_i \tag{1.4}$$

1.5.3 Collisionless heating

Another heating mechanism that occurs at low pressure $\approx$ 1 - 40 mTorr where $\lambda_{en} \geq D$ is known as collisionless or stochastic heating. Stochastic heating occurs when the electron atom/molecule collision frequency is small and when electrons have sufficient energy to overcome the dc ambipolar potential well within the bulk and can reach the plasma-sheath boundary. These electrons will gain energy to sustain the discharge by the oscillating sheath. This heating mechanism and has been the subject of much investigation by many

researchers [9–11]. The EEPF in the collisionless regime usually takes the form of a bi-Maxwellian distribution [7].

1.6 Scope and thesis layout

The key objective of this research was to investigate important process parameters critical to industrial plasma processing. These are the densities of reactive specie such as atomic oxygen and fluorine. Reliable (sophisticated) techniques such as TALIF and AMPS were used to detect O and F atoms in plasmas commonly used in IC manufacturing. The dominant processes responsible for effecting [F] and [O] such as the wall conditions and the electron kinetics were investigated. These techniques were compared to actinometry which can also be used to measure O and F atoms. This method has a low footprint and is very desirable for a sensor within industry.

A brief introduction into CCP and important topics such as reactor wall conditions and operating regimes (α and γ mode) is given in chapter 1. The theory behind the plasma diagnostics techniques used in this thesis and experimental arrangements is given in chapter 2. Discussed in chapter 3 is the investigation of the behavior of [O] measured with TALIF for various mixtures of O_2/SF_6. Changes in the electron kinetics and the corresponding effects in the production of oxygen atoms was also discussed in this chapter with the use of a Langmuir probe.

Discussed in chapter 4 is the investigation of various discharge mode transitions with power and pressure such as the $\alpha - \gamma$ transition and the stochastic - ohmic transition in O_2 plasma with the use of a Langmuir probe. The investigation of [F] measured with APMS in SF_6 and SF_6/O_2 plasma is reported in chapter 5. Actinometry for detection of relative changes in [F] is

also discussed and compared to APMS in this chapter. A conclusion of these chapters is then given in chapter 6.

CHAPTER 2

Diagnostics

2.1 Oxford instruments plasmalab system 100.

The plasma source investigated in this thesis was an Oxford instruments plasmalab system 100 [12]. A brief outline of this plasma system is given in this section. The plasmalab system 100 is a capacitively-coupled (parallel plate) plasma, CCP, which was excited with 13.56 MHz rf power. Figure 2.1 shows a simplified schematic of the important features of this plasma system. The plasma system is both electrically and geometrically asymmetric. The reactor (inner bore) was cylindrical in shape and has radial and axial lengths of 380 and 130 mm respectively. The driven electrode was 205 mm in diameter and was capable of holding 200 mm wafers, the electrode separation distance was 45 mm. The grounded electrode was 295 mm in diameter and also served as the shower-head to supply the feedstock gas, the chamber walls

(radial) are grounded. The reactor material (walls and electrodes) was made from an aluminium alloy (6082) whose main chemical component is Al but also contains small amounts of Mg (1.2%), Si (1%), Mn (0.8%), Fe (0.25%) and Zn (0.25%). Chilled water was supplied to the driven electrode which, however, does not effectively cool or maintain a constant surface temperature during plasma operation while the side walls of the reactor are not cooled at all.

The chamber was evacuated using an Alcatel (ATP400HPC) turbo-molecular

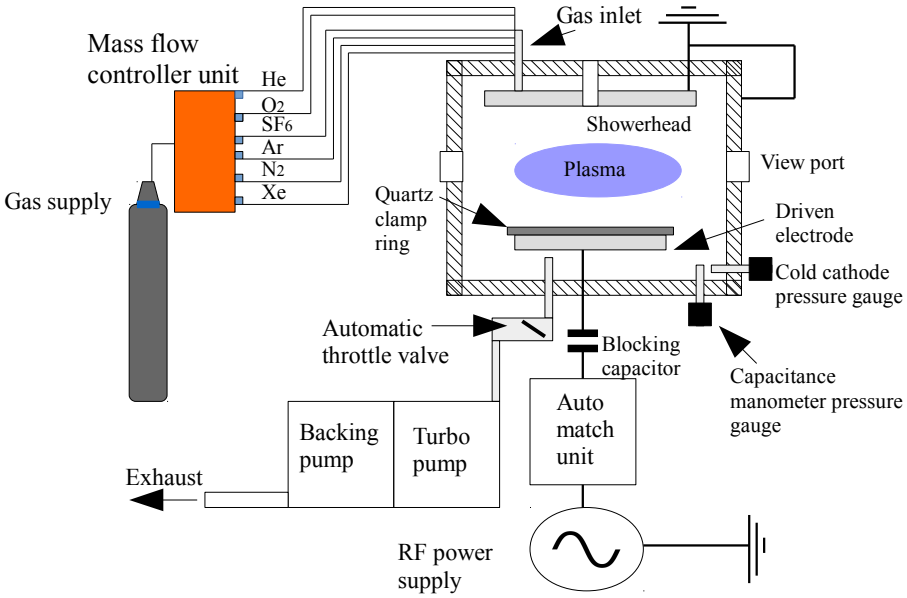

Figure 2.1: Schematic of the oxford instruments plasma system.

pump which has a pumping speed of 400 l·s $^{-1}$ (N_2). This pump was backed by an Alcatel rotary pump (2033C2) which has a pumping speed of approximately 6 l·s $^{-1}$. The typical base pressures achieved after $\approx$ 5 minutes of

pumping were in the range of $5{\times}10^{-5} - 5 \times 10^{-6}$ Torr. The base pressure was measured with a cold cathode ionization gauge (Edwards AIM-S-NW25). The chamber pressure was controlled by variable throttle valve located below the driven electrode which was automatically controlled in order to keep a fixed pressure set point. The process pressure was measured with a MKS (627B-15968) capacitance manometer, this gauge can operate between $\approx$ 1 - 1000 mTorr. It was necessary to adjust the flow rates when using a mixture of gases to correct for differences in pumping speeds, this allows the correct partial pressures to be achieved. An automatic matching network was located between the rf generator and electrode which tunes the impedance of the output from the generator to match the impedance of the load. This ensures an efficient power coupling from the power supply to the plasma. The plasma system has four access ports for optical and electrical diagnostics. Three of these access ports are 40 mm in diameter and are located on the radial inner bore of the chamber. Optical access was also supplied through a hole 10 mm in diameter in the center of the shower. All view ports were made from quartz (fused silica), which has a constant transmittance ($\approx$ 90 %) for wavelengths between $\approx$ 0.25 - 3.0 μm. Electrical probes were positioned at the radial and axial center of the discharge i.e. 190 mm from the inner (radial) wall and 22.5 mm from the driven/grounded electrode.

2.2 Two-photon absorption laser-induced fluorescence spectroscopy

Laser-induced fluorescence (LIF) and two-photon absorption laser-induced fluorescence (TALIF) spectroscopies are active diagnostic techniques that can be used to determine plasma parameters such as particle densities (both

spatially and temporally resolved), radiative lifetimes, collisional-quenching coefficients and particle temperatures [13, 14]. Species which can be measured with both LIF and TALIF include atoms and molecules, metastables and ions.

LIF (single photon) spectroscopy requires exciting particles into higher energy levels by absorption of a single photon from a laser source followed by spontaneous emission of a fluorescence photon when the excited state decays to an intermediate level between the excited and ground state. However, laser generated fluorescent radiation is proportional to the population of the decaying excited state only. In most cases the density of the probe state (ground) is of interest, which necessitates a model which takes additional excitation and de-excitation mechanisms into account. Then, in principal, it is possible to determine the density of the probed state from the observed fluorescence provided the conditions for the model are satisfied. The probe radiation required for typical atomic species found in plasmas e.g. Ar, O, H, N, F, and Cl is in the VUV region. This can often be problematic as this spectral region is often just out of the spectral range of commercial dye lasers. Consequently, a more sophisticated, non-commercial, laser/experimental set up is required which can be difficult and challenging to implement [14, 15]. Further more, the VUV probe radiation can also be absorbed by other plasma species and the background gas. This can result in low probe radiation intensities which may limit the diagnostic to particular plasma conditions, feedstock mixtures and pressures.

Laser-induced excitation can also occur through the simultaneous absorption of two-photons (TALIF). This can be useful as excitation occurs through the combined energy of the two photons. Therefore the challenge of generating VUV laser radiation for single photon LIF is avoided and thus, commer-

cial dye lasers can be used. However, the two-photon absorption transition probabilities are smaller than the single photon excitation process by orders of magnitude. Consequently, high laser intensities are required which can be achieved by focusing the laser beam into a small volume. A simplified schematic of the basic set up LIF and TALIF experiments are shown on figure 2.2. In this work, TALIF was used for detection of atomic oxygen density in O_2 and O_2/SF_6 based plasmas. A calibration scheme which is based on TALIF on xenon atoms was also implemented to provide absolute atomic oxygen densities.

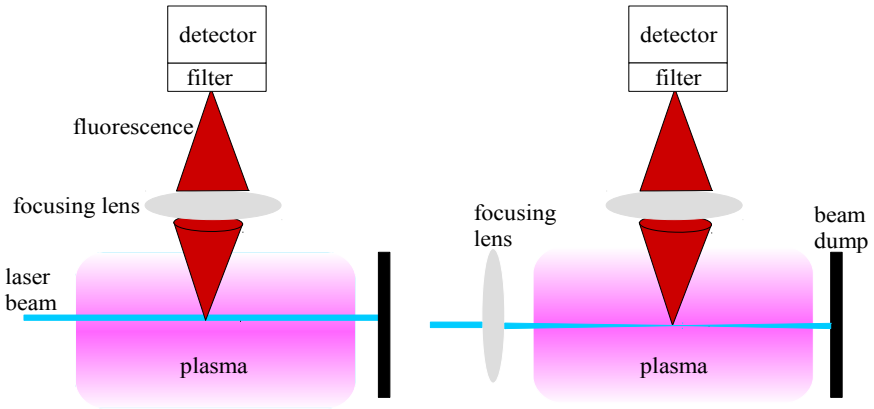

Figure 2.2: Typical set ups for (left) laser-induced fluorescence and (right) two-photon laser-induced fluorescence. No focusing lens if required for the laser beam for single photon LIF.

2.2.1 Excitation dynamics and rate equations

TALIF spectroscopy for detection of oxygen atoms requires two laser laser generated photon (≈ 225 nm) to excite the $O(2p^4\ ^3P_2)$ level to the $O(3p^3P_{1,2,0})$ level. Spontaneous emission at ≈ 844 nm occurs upon decay to the $O(3s^3P)$ state. This section discusses the TALIF model that is used for determining ground state densities. This model is based on a set of time dependant differential rate equations which contains state populations and rates of dominant processes such as laser excitation, R, and fluorescence, A. However, additional processes can affect the excitation and depopulation dynamics. Such processes and their corresponding rates are photo-ionization, P, amplified spontaneous emission (ASE) or also known as stimulated emission, S, collisional de-excitation (quenching), Q, and finally plasma assisted processes such as electron-impact excitation or cascade excitation, C. Figure 2.3 shows a simplified schematic of a four level system used to describe the population dynamics of the relevant energy levels. Levels 1, 2, 3 and 4 refer to the ground state, an intermediate state (for which fluorescence occurs to), a laser excited state and the ionization continuum respectively. The laser-induced excited state population, n_3, is assumed to be entirely produced by laser photons from ground state i.e. $n_1 \rightarrow n_3$. However, n_3 can be populated through other plasma assisted mechanisms such as electron-impact excitation and cascade transitions. It is assumed that such processes are negligible ($C \approx 0$) in low-pressure capacitive discharges due to the predominately high rate of laser excitation ($R \gg C$). This assumption would probably be violated in discharges characterized by $n_e \gg 10^{18}\mathrm{m}^{-3}$. Under such conditions C must be accounted for. The laser excitation rate is given by

$$R(t) = \sigma^2 G^2 g(\triangle \upsilon) \left(\frac{I_{LS}(t)}{h\upsilon_L} \right)^2 \tag{2.1}$$

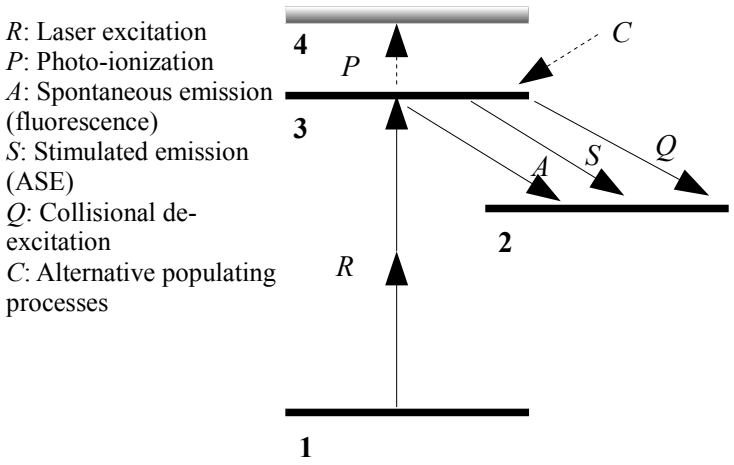

Figure 2.3: Simplified energy level diagram for TALIF excitation and de-excitation processes with corresponding process rates

where σ^2 is the two-photon absorption cross-section, G^2 is a statistical factor based on temporal variation of the laser and is ≈ 2 [16], $g(\triangle v)$ represents the convolution of the laser and absorption line profile, I_{LS} is the laser intensity (integrated over volume), h is Plank constant and v_L is the photon frequency. Non-radiative de-excitation (quenching) of the laser excited state can occur when the excited species of interest undergoes collisions with the background gas. This collisional deactivation process is significant in atmospheric pressure discharges and competes with fluorescence. Generally, quenching is not significant below 500 mTorr [17] and can often be ignored in low-pressure processing plasmas particularly for pressures less than 100 mTorr. The gas pressures investigated in this report are high enough for quenching to have a

measurable effect (comparable to twice the standard error) on the evaluation of [O]. Therefore, the quenching process was considered in the TALIF model used in this work. The rate of this collisional quenching process is given by

$$Q = k_q n \tag{2.2}$$

where k_q is the collisional quenching rate constant and n is the number density of the collisional partner. The collisional quenching rate constant is either known from the literature or can be measured for specific collisional partners by time resolved LIF/TALIF measurements of the species of interest [18]. Alternatively, if the collision cross-section, σ_q, and the gas temperature are known then the collisional quenching rate constant can calculated using

$$k_q = \sigma_q \langle \upsilon_n \rangle \tag{2.3}$$

where $\langle \upsilon_n \rangle$ is the mean neutral velocity. Another competing de-population mechanism is amplified spontaneous emission (ASE) also known as stimulated emission. This occurs at high laser intensities which creates a population inversion between levels 3 and 2 within one laser pulse. For example, the lifetime of the O($3s^3S$) intermediate state is short ($\approx$ 1.8 ns) [17] in comparison to the laser excited O(3p $^3P_3$) state ($\approx$ 35.1 ns) [13]. Therefore, saturation of n_3 can occur at high laser intensities within one laser pulse which results in stimulated emission and a depletion of n_3. The occurrence of ASE can result in a non-linear dependence of the fluorescent signal with ground state density [17, 19], therefore saturation of n_3 must be avoided. Photons produced as a result of ASE have the same energy as the fluorescent photons. However, the ASE is directed on the same optical axis as the laser beam only. Therefore the ASE signal will not be superimposed on the TALIF signal if the fluorescence detector is positioned off axis i.e. perpendicular to the laser beam. The onset of ASE can also be identified by a characteristic

narrow spectral profile compared to the purely fluorescent spectral profile [19, 20]. Operating at high laser intensities can also result in the absorption of a third photon which results in ionization of the probed species (photo-ionization). A noticeable reduction in the fluorescent radiation occurs when this process is significant due to the depletion of the ground state density. Monitoring the TALIF signal as function of laser intensity can be used to identify the onset of processes that effect fluorescent radiation such as ASE and photo-ionization. A characteristic slope of ≈ 2 from a log-log plot of the TALIF signal versus laser intensity indicates normal operating conditions usually referred to as the quadratic regime. Deviation from a slope of ≈ 2 is indicative of saturation of n_3 or depletion of n_1 and the associated laser intensity would not be applicable for reliable measurements of ground state densities.

Differential rate equations can be constructed which describe the time varying population densities of the relevant energy levels and these rate equations can then be solved to evaluate the ground state density. A three level system is sufficient to derive the important parameters for TALIF. This model is based on the assumption that processes such as photo-ionization and ASE are negligible, the rate of change of the laser excited state population, n_3, is

$$\frac{dn_3(t)}{dt} = R(t)n_1(t) - (A+Q)n_3(t) \tag{2.4}$$

the rate of change of the ground state density is

$$\frac{dn_1(t)}{dt} = -R(t)n_1(t) \tag{2.5}$$

The solutions to the integrations of Eqn.(2.4) and Eqn.(2.5) and the known laser excitation rate Eqn.(2.1) allows for the number of fluorescent photons, n_{FL}, to be evaluated by

$$n_{FL}(t) = \frac{A_{ij}}{A+Q}\frac{\sigma^2}{(h\upsilon)^2}G^2 g(\triangle\upsilon)n_1 \int I_{LS}^2(t)dt \tag{2.6}$$

The first term on the R.H.S of Eqn.(2.6) is usually called the optical branching ratio or the quantum yield and accounts for the fraction of fluorescence that is observed. This is due to the fact that the laser excited state can also decay to other lower intermediate levels and also non-radiatively (quenching). When alternative de-excitation pathways exist, the total fluorescent rate, $A = \sum_j A_{ij} = \tau_i^{-1}$, and the fluorescent rate of the considered transition, A_{ij}, must be known. τ_i^{-1} is the radiative lifetime of the excited state and can be either found in the literature or measured from the decay time of time resolved fluorescent signals [13, 18, 21]. For the atomic oxygen excitation scheme used in this study, the ratio A_{ij}/A is unity [22]. The collisional quenching rate (Q) can be determined by the collisional quenching coefficient, k_q, and the corresponding density of the collisional partner i.e. $Q = \sum_q k_q n_q$. In summary to Eqn.(2.6) the number density of ground state species is proportional to the number of fluorescent photons divided by the laser intensity squared provided that the optical branching ratio is constant. This $n_1 \propto n_{FL}/I_{LS}^2$ relationship forms the basis of the calibration technique which is discussed in section 2.2.2.

2.2.2 Absolute [O] using xenon calibration scheme

Section 2.2.1 discussed the important processes required for TALIF to be a reliable diagnostic for detection of ground state species in low-pressure discharges. It was shown that under certain conditions the TALIF model was greatly simplified down to a proportionality between the ground state density and number of fluorescent photons normalized by the laser intensity squared. However, direct evaluation of Eqn.(2.6) for determining ground state density is challenging for two main reasons. Firstly, the number of fluorescent photons is extremely difficult to measure as only a small number

of the isotropically distributed fluorescent photons, n_{FL}^{Frac}, are collected for detection. n_{FL}^{Frac} is proportional to several parameters i.e.

$$n_{FL}^{Frac} \propto \left(\frac{\triangle\Omega}{4\pi}\right) n_{FL} T_{optics} \tag{2.7}$$

where $\triangle\Omega$ is the solid angle of detection n_{FL} is the total number of fluorescent photons integrated over the excitation volume and T_{optics} is the product of transmission efficiencies for any optical components used to collect the fluorescent radiation i.e. lenses, mirrors, bandpass filters and windows. These parameters are not easily measured. Furthermore, the measured photomultiplier signal, S_{PMT}, is proportional to various parameters,

$$S_{PMT} \propto G_{PMT} \eta_{hv}^{PMT} R_T n_{FL}^{Frac} \tag{2.8}$$

where G_{PMT} is the amplification factor of the photomultiplier tube, and η_{hv} is the wavelength dependent quantum efficiency, R_T is the total resistance of any resistive components within the detector and n_{FL}^{Frac} is the fraction of fluorescent photons incident on the collection area of the photomultiplier tube. Secondly, explicit evaluation of the spatial distribution of the laser intensity is required for Eqn.(2.6) which is difficult to determine due to the poorly characterized spatial distribution of the laser beam within the focused volume. Clearly, many experimentally determined parameters are required for determining the absolute number of fluorescent photons and this makes direct evaluation of ground state density using Eqn.(2.6) both challenging and unreliable due to many possible sources of uncertainty.

A calibration scheme that was first proposed by Goehlich *et al* [21] can overcome many of these difficulties. This technique is based on a comparative measurement of a TALIF signal from a reference gas incorporated into the same experimental system as the species investigated. Xenon was used in this work as the reference gas for calibration of the oxygen TALIF signals. This is

the references gas commonly used for calibration of [O] [13, 21–23], however, alternative noble gases can be used to calibrate other atomic species found in plasma [14]. The excitation scheme for xenon atoms is spectrally close to the atomic oxygen scheme in terms of both the probe and fluorescence radiation. Therefore the same optical arrangement can be used for experiment and calibration which eliminates the need to know various parameters that are problematic to define. The excitation scheme for xenon and oxygen atoms are shown on figure 2.4.

The resonance excitation wavelength for the $O(2p^4\ ^3P_2)$ to the $O(3p^3P_{1,2,0})$

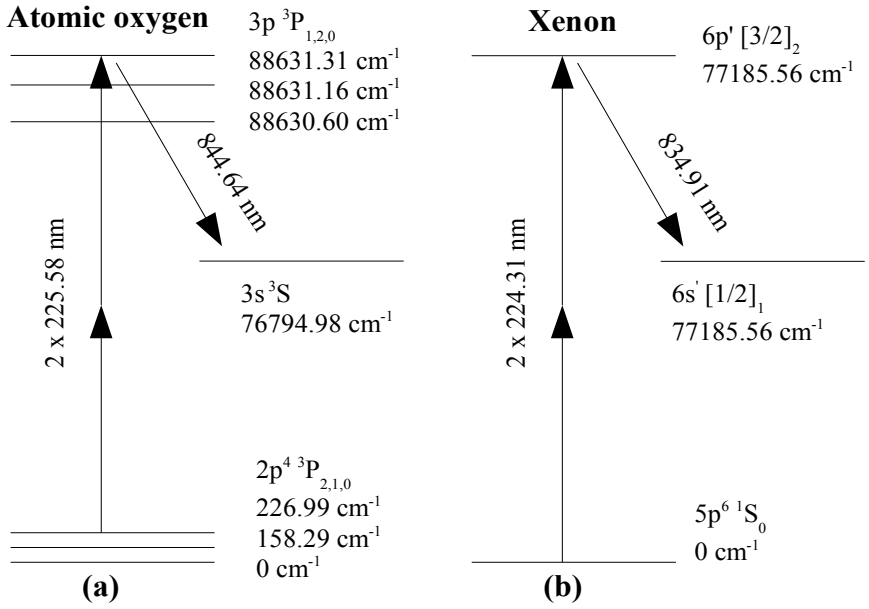

Figure 2.4: TALIF excitation scheme for oxygen (a) and xenon atoms (b).

transition and for the $Xe(5p^6\ ^1S_0)$ to $Xe(6p'[3/2]_2)$ transition is approximately 225.58 nm and and 224.31 nm respectively. The subsequent fluores-

cence from the excited oxygen and xenon atoms is at 844.64 nm and 834.91 nm respectively. The assumption of similar spatial and temporal variations of the laser intensity distribution is best met when the wavelengths of excitation for both transitions are spectrally close. Also the similar fluorescence wavelengths allows the arrangement for both experiment and calibration to be identical i.e. filters, lenses and photo multiplier tube.

The laser wavelength is scanned over the absorption line of oxygen and xenon atoms and the corresponding fluorescent signal is measured for each exciting wavelength to form a fluorescent spectral profile. A time varying fluorescence signal results from the characteristic radiative lifetime of excited states ≈ 20 - 100 ns, therefore the fluorescent signal must be integrated with respect to time. The time integrated fluorescence signal for each laser wavelength is then normalized to the square of the time integrated laser intensity. This removes the dependence of S_{PMT} on I_{LS} and also removes any shot to shot variation in the laser intensity. This normalized fluorescent signal, I_{FL}, is then proportional to the ground state density as shown by

$$I_{FL} = \frac{\int S_{PMT}(t)dt}{\int I_{LS}^2(t)dt} \propto n_1 \tag{2.9}$$

An example of a time resolved fluorescent signal for xenon is shown on figure 2.5, also shown is time resolved laser signal measured with a fast photo-diode. The temporal characteristics of this fluorescent PMT signal can be related to the natural lifetime and collisional quenching coefficient of the excited state. Section 2.2.3 discusses the evaluation of the collisional quenching coefficient of the O(3p $^3P_3$) state by SF_6 molecules using the temporal TALIF signal. I_{FL} was measured as a function of excitation wavelength for both xenon and oxygen to form fluorescent spectral profiles. The profiles were integrated with respect to wavelength which removes the dependence of the fluorescent profiles on the absorption linewidth and any Doppler broadening. The oxygen

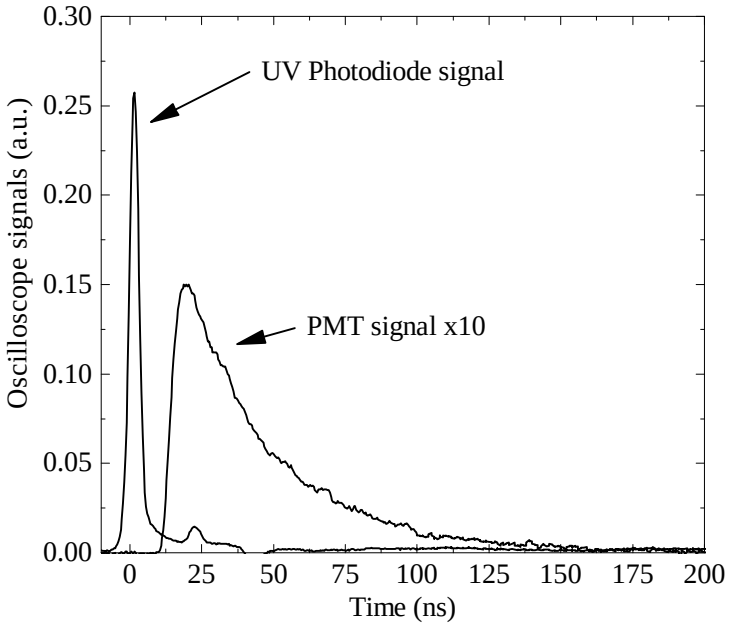

Figure 2.5: Typical time varying oscilloscope signals of the laser beam measured with a fast UV photo-diode and a xenon TALIF signal measured with a red sensitive PMT scaled ($\times$ 10) for comparison.

fluorescent profile is non-symmetric and is composed of the three fluorescent profiles due the splitting of the upper state (J''=2,1,0) where J is the principal quantum number. However, the splitting is small, being comparable to the width of the exciting laser profile and therefore these lines are not usually resolved and only small contributions from each line are noticeable from the overall fluorescent spectral profile. An example of a typical oxygen fluorescent spectral profile upon excitation from O($2p^4\ ^3P_2$) to O($3p\ ^3P_{J''}$) is shown in figure 2.6, this fluorescent profile was recorded in an O_2 plasma operated at 100 mTorr and 100 W and both the measured data points and a theoretical fit to the measured data based on the sum of three (Gaussian distributions) fine structure contributions of the excited state are shown. The fine structure

components are weighted in accordance with the relative photon absorption cross-sections from the fine structure ground state level (quantum number $J' = 2$) to each of the excited fine structure levels (J''= 0, 1, 2) taken from Saxon [24]. Figure 2.6 does not show the absolute spectral positions due to the miscalibrated laser wavelength. The relative spectral positions for the fitting procedure are therefore displaced based on the well known theoretical energy levels. The line widths of the three fine structure components were varied until a best fit (least squares) between the sum the three distributions and the measured data points was established. The xenon excitation scheme exhibits no fine structure and the fluorescent profile is either Gaussian or Lorentzian depending the distribution of the laser line.

The atomic oxygen density can be determined by taking the ratio of these normalized fluorescent signals (I_{FL}) for both oxygen and xenon which gives

$$[\mathrm{O}] = [\mathrm{Xe}]\frac{I_{FL}^{\mathrm{O}}}{I_{FL}^{\mathrm{Xe}}}\frac{\sigma_{\mathrm{Xe}}^2}{\sigma_{\mathrm{O}}^2}\frac{a_{\mathrm{Xe}}}{a_{\mathrm{O}}}\frac{\eta_{\mathrm{Xe}}^{PMT}}{\eta_{\mathrm{O}}^{PMT}}\frac{T_{\mathrm{Xe}}}{T_{\mathrm{O}}} \tag{2.10}$$

where I_{FL}^{O} and I_{FL}^{Xe} denotes the wavelength integrated normalized fluorescent signals of oxygen and xenon respectively, σ_{O}^2 and σ_{Xe}^2 are the two photon absorption cross-sections of the oxygen and xenon transitions respectively, a is the optical branching ratio and is equal to $A_{ij}/(A+Q)$, η_{Xe}^{PMT} and η_{O}^{PMT} and also T_{Xe} and T_{O} represents the photomultiplier tubes quantum efficiency and transmission efficiency of the band pass filter for the fluorescent wavelengths of oxygen and xenon respectively. The xenon number density was determined using the ideal gas law and the known pressure and temperature ($\approx$ 300 K) of xenon in the vessel. The xenon calibration was carried out prior to plasma experiments to ensure the reactor walls were at room temperature.

As shown on figure 2.4 ground state atomic oxygen exhibits fine structure that is significantly larger than the splitting of the excited state which is less than the Doppler broadened half width (0.274 cm^{-1}) at 300 K. However,

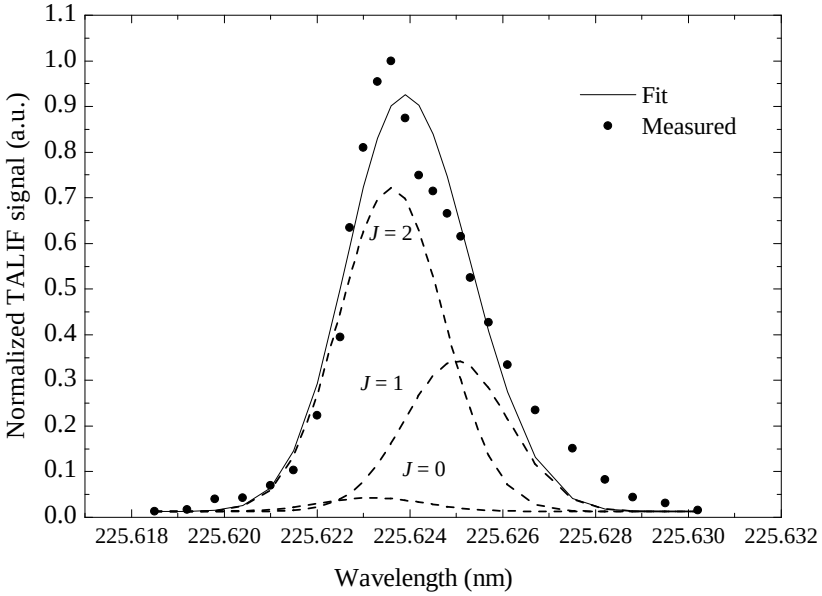

Figure 2.6: The measured atomic oxygen fluorescent spectral profile (•). The signal used for determining [O] was the sum (−) of three theoretically determined fluorescent components (· · ·).

it is only necessary to probe one sub-level to determine the total ground state population. At room temperature approximately 74 % of the oxygen atoms lie in the $^3P_2$ sub-level. Therefore the laser was set to excite the $^3P_2$ state in order to produce the optimum TALIF signal intensity. The Boltzmann population equation was then used to calculate the fraction of oxygen atoms in the $^3P_2$ and hence correct for this partitioning. For a given gas temperature, T_g, and assuming a thermal population distribution the Boltzmann population equation is

$$\frac{n_{J'}}{\sum_{J'} n_{J'}} = \frac{(2J'+1)\exp\left(\frac{-E_{J'}}{k_B T_g}\right)}{\sum_{J'}(2J'+1)\exp\left(\frac{-E_{J'}}{k_B T_g}\right)} \tag{2.11}$$

where k_B is the Boltzmann constant. Processes such as photo-ionization and ASE which can effect the fluorescent signal were avoided by working with low laser intensities that correspond to the non-saturation, quadratic regime. This quadratic regime was identified by a log-log plot of the fluorescent signal versus laser intensity which yields a characteristic slope ≈ 2 provided no disturbances of the fluorescence from ASE and photo-ionization.

2.2.3 Determination of the quenching rate constant of O(3p $^3P_3$) by SF_6 molecules.

Collisional quenching is a non-radiative relaxation process which effects the radiative fluorescent rate. This quenching process was included into the TALIF model for determining [O]. In this work, TALIF was used for determining [O] in O_2/SF_6 plasma, therefore the main quenching species for the O(3p $^3P_3$) state that were considered were O_2 and SF_6. The O_2 quenching coefficient, $k_q^{O_2}$, is known from the literature [22], however no quenching coefficient for O(3p $^3P_3$) by SF_6 molecules are available. Therefore, it was necessary to measure the quenching coefficient, $k_q^{SF_6}$, for O(3p $^3P_3$) by SF_6 molecules for an accurate determination of [O] by Eqn.(2.10). Furthermore, the same O(3p $^3P_3$) excited state (electron-impact) is used for determining [O] by actinometry (in O_2/SF_6 plasma) which is discussed in section 2.3.1, thus, $k_q^{SF_6}$ is also a requirement for actinometry measurements presented in this thesis.

The fluorescence decay rate is inversely proportional to the lifetime of the excited state. Thus, a measurement of the temporal fluorescent signal can be related to the natural lifetime, τ_{nat}, of the excited state and also the collisional-quenching rates. This relationship is shown by

$$\tau_{eff}^{-1} = \tau_{nat}^{-1} + k_q^{O_2}[O_2] + k_q^{SF_6}[SF_6] \tag{2.12}$$

where τ_{eff}^{-1} is the effective decay time and was determined from the exponential decay of the fluorescence PMT signal. τ_{eff}^{-1} was measured as a function of [SF_6], this was achieved by varying the flow rates and total pressure (100 - 300 mTorr) in an O_2/SF_6 plasma in order to vary [SF_6] while keeping [O_2] constant. A so called Stern-Volmer plot was used to determine $k_q^{SF_6}$ and the natural lifetime (τ_{nat}) of the O(3p $^3P_3$) state by the slope and intercept respectively. This Stern-Volmer plot is shown in figure 2.7.

The gas temperature, T_g, is required to calculate the main collisional-

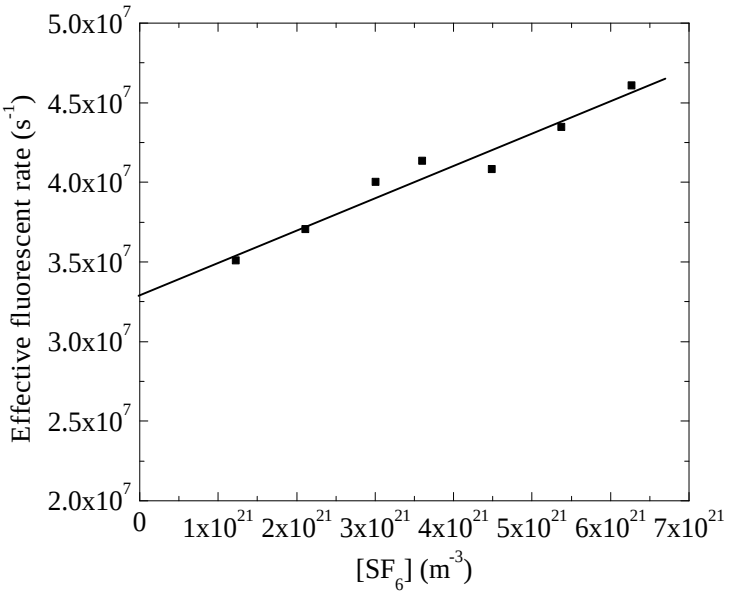

Figure 2.7: Stern-Volmer plot of the effective fluorescent decay rate versus SF_6 concentration, the slope is equal to k_{SF_6}.

partner (O_2 and SF_6) number densities required for Eqn.(2.12) using the known partial pressure and the ideal gas-law. This allows $k_q^{SF_6}$ to be determined for a known temperature which, in turn, allows for the quenching

cross-section to be estimated for a given T_g since $k_q = \sigma_q n$. Therefore it was necessary to measure T_g for both the evaluation of $k_q^{SF_6}$ (Stern-Volmer plot) and also for the experiments in order implement this quenching correction for recalculated k_{SF_6} for a given gas temperature. T_g varied by only 5 K throughout the Stern-Volmer experiment, therefore it was assumed that T_g was constant at 325 K for determination of $k_q^{SF_6}$ by Eqn.(2.12).

A plot of τ_{eff}^{-1} versus [SF_6] yields $k_{SF_6} = 20.2 \pm 4.1 \times 10^{-10}$ cm^3·s^{-1} from the slope. No quenching coefficient for SF_6 was in the literature for comparison. A method to check this result would be to evaluate the natural lifetime and compare it to values which are well known from the literature. The zero pressure intercept and also $k_{O_2} = 9.4 \pm 0.5 \times 10^{-10}$ cm^3·s^{-1} [22] allows for τ_{nat}^{-1} to be determined. The natural lifetime was 32.9 ± 1.8 ns which is in reasonable agreement to values such as 34.7 ± 1.7 ns and 35.1 ± 3.0 ns reported elsewhere [13, 22]. [O] increased by ≈ 10 % (on average) after this collisional quenching correction factor was applied in a plasma operated at 100 mTorr.

2.2.4 TALIF experimental set up

Figure 2.8 shows a schematic of the experimental set up for the TALIF experiment. The laser used in this work was a combination of two commercial laser systems configured into a single unit. A Nd:YAG laser from Innolas was used to pump a dye laser from Radiant Dyes Laser and Accessories GmbH. The pulsed (10 Hz) fundamental Nd:YAG output at 1064 nm was frequency doubled using a non linear crystal (BBO). This 532 nm beam was guided into the dye laser to pump a dye solution of DCM/Pyridine 1 dissolved in methanol of high purity. Tunable fluorescent laser radiation at approximately 675 nm was then frequency doubled and tripled using two KBO crystals to

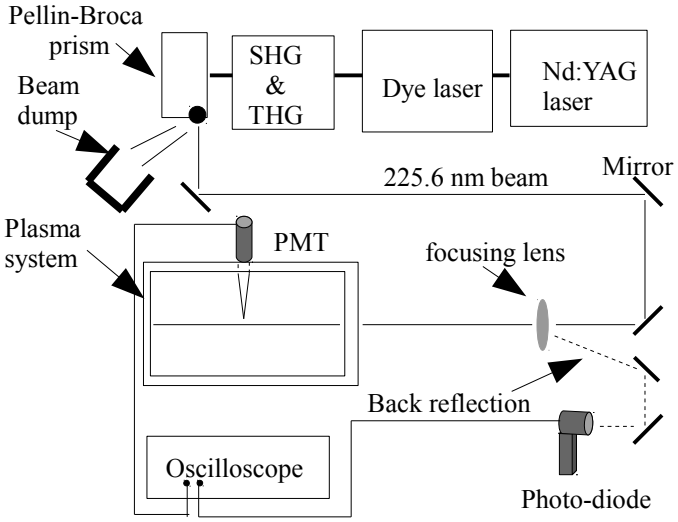

Figure 2.8: Schematic of TALIF experimental set up.

produce a 225 nm beam. A pellin broca prism system was used to separate the 225 nm beam from residual pump laser beams. The pulse energy and beam diameter were approximately 1 mJ and 6 mm, respectively. UV grade mirrors and a 50 mm plano convex fused silica focusing lens was used to steer and focus the laser beam into the plasma bulk. A small (3 mm $\times$ 3 mm) absorbing material was positioned on the inner wall of the reactor to act as a beam pump to prevent scattering of laser photons into the detector. Optical access was supplied via an aperture in the centre of the shower head and was used for the detection of the fluorescent photons. A KF-10 standard quartz viewport was mounted external to the showerhead. An 845 $\pm$10 nm optical band pass filter was placed directly after the viewport to suppress the background radiation from plasma entering the PMT, the fil-

ter and PMT were housed in custom built mount which attached onto the viewport. The detector used was a red sensitive photomultiplier tube from Hamamatsu (R632-01) which had a rise time of 2.2 ns. A fraction of the laser beam (back reflection from the focusing lens) was positioned onto a fast UV photo-diode (Thorlabs DET210) to monitor relative variations of the laser intensity for normalization of the TALIF signal.

2.3 Actinometry

Plasma diagnostics which are based on optical emission spectroscopy (OES) are highly desirable for industrial applications due to its non-invasive nature and low footprint. OES based techniques that can be used to investigate elementary plasma processes include trace rare gas optical emission spectroscopy (TRG-OES) and the line ratio method for determination of the electron temperature, electron density and electron energy distribution function [25, 26], line broadening techniques for estimating the gas temperature and electron density [27], end point detection for determining the completion of a plasma process [28] and phase resolved optical emission spectroscopy (PROES) for insight into the spatial and temporal dynamics of the high energy electrons within one RF cycle [29].

Another popular OES based plasma diagnostic technique that can be used to determine particle densities is actinometry. In this work, actinometry was used for detection of both atomic oxygen and fluorine. This technique was first introduced by Coburn and Chen [30] and is based on comparative measurement of the optical emission line intensity of a species with a known density (actinometer) to the optical emission line intensity of a species of unknown density to be determined. The actinometer is usually a noble

gas due to its non-reactive nature and the typical amount required is small ($\approx$ 1 - 10 %). In this work, the emission line at 750 nm from $Ar(2p_1)$ was used as the actinometer. The concentration of the actinometer must be either known for determining absolute particle densities or constant if detecting relative changes in particle density. The concentration of the actinometer can be evaluated by the ideal gas law and the known temperature and partial pressure in the feedstock. Assuming the relevant excited state is populated directly from ground state followed by radiative decay only, the measured time averaged intensity of an optical emission line is given by

$$I_{\mathrm{X}} = c_{\mathrm{X}} h\upsilon_{\mathrm{X}} A_{ij}^{\mathrm{X}} n_e k_e^{\mathrm{X}} [\mathrm{X}] \tag{2.13}$$

where I_{X} is the measured intensity of species X, c_{X} is a factor which takes into account the observation volume and spectral response of the detection system, $h\upsilon_X$ is the photon energy, A_{ij}^{X} is the spontaneous emission rate of the observed transition, n_e is the electron density, k_e^{X} is the electron impact excitation rate constant and [X] is the ground state number density. The difficulties with using one emission line to monitor ground state species is that the intensity is proportional to the decaying excited state only. Thus, the changes in the intensity are not simply related to the ground state density and could be due to changes in several parameters

$$I_{\mathrm{X}} \propto A_{ij}^{\mathrm{X}} [\mathrm{X}^*] \tag{2.14}$$

where [X*] is the density of excited species X. [X*] can be determined by

$$\begin{aligned} [\mathrm{X}^*] &= n_e k_e^{\mathrm{X}} [\mathrm{X}] \\ &= n_e [\mathrm{X}] \int_0^\infty f_e(\varepsilon) \sigma_e^{\mathrm{X}}(\varepsilon) \upsilon_e(\varepsilon) \quad d(\varepsilon) \end{aligned} \tag{2.15}$$

where ε denotes the electron energy, $f_e(\varepsilon)$ is the normalized electron energy distribution function (EEDF), σ_e^{X} is the electron impact excitation cross-

section and v_e is the electron velocity. Therefore, knowledge of the excitation cross-section and also plasma parameters such as the electron density and the EEDF are required for determining [X] using Eqn.(2.13). Furthermore, the absolute spectral intensity is needed for Eqn.(2.13) which requires an absolute spectral intensity calibration of the detection system which is not a practical procedure that can be implemented easily within an industry environment.

However, normalizing the intensity of the species of interest by the intensity of an optical emission line from an actinometer eliminates the dependence of I_{X} on the electron density. Under the assumption that the energy dependent shapes of the excitation cross-sections for both the species of interest the actinometer and also the threshold energies are similar, then, the line ratio is dependent on the EEDF and [X] only. However, the ratio of signal from the species of interest to the actinometric signal can still be useful for monitoring relative changes in concentrations provided the EEDF and actinometer concentration are fixed, i.e.

$$\frac{I_{\mathrm{X}}}{I_{\mathrm{Ar}}} \propto [\mathrm{X}] \tag{2.16}$$

where I_{Ar} is the intensity of the argon actinometer emission line. Taking the ratio of the intensities of the emission lines from the species of interest and actinometer allows absolute concentrations to be determined if the ratio of the excitation rate constants, $k_e^{\mathrm{Ar}}/k_e^{\mathrm{X}}$, is known and is given by

$$[\mathrm{X}] = \frac{I_{\mathrm{X}}}{I_{\mathrm{Ar}}} \frac{\eta_{\mathrm{Ar}}^{spec}}{\eta_{\mathrm{X}}^{spec}} \frac{h\upsilon_{\mathrm{Ar}}}{h\upsilon_{\mathrm{X}}} \frac{A_{ik}^{\mathrm{Ar}}}{A_{ik}^{\mathrm{X}}} \frac{k_e^{\mathrm{Ar}}}{k_e^{\mathrm{X}}} [\mathrm{Ar}] \tag{2.17}$$

where η^{spec} denotes the wavelength dependent spectral response of the detection system, $h\upsilon$ is the photon energy, k_e is the electron impact excitation rate constant and [Ar] is the argon concentration. This actinometry approach for measuring particle densities is known as the classical actinometric model.

It is valid provided optical emission is generated by direct electron impact excitation from ground state and that population by dissociative excitation and by metastables is negligible and that the excitation cross-sections have a similar energy dependence particularly near the threshold for excitation and that collisional quenching of the excited level is negligible.

2.3.1 Oxygen actinometry

Determination of [O] in oxygen plasmas using the classic actinometry model can sometimes be unreliable when compared to an independent measurement of [O] using techniques such as TALIF or absorption spectroscopy. This is predominantly due to dissociative excitation which is an additional populating mechanism that produces optical emission at the same wavelength as the species of interest i.e. $e + O_2 \rightarrow O^* + O + e$. Therefore, the classic actinometry model must be modified to include the contribution from this additional excitation mechanism. The set of direct and dissociative excitation process used in this work for detection of atomic oxygen density by actinometry are,

$$e + O(2p^4\ {}^3P) \overset{k_e^{O(3p)}}{\rightarrow} O(3p^3P) + e,\ \varepsilon^*_{thr} = 10.98\ \text{eV}$$

$$e + O_2 \overset{k_{diss}^{O(3p)}}{\rightarrow} O(3p^3P) + O + e,\ \varepsilon^*_{thr} = 16.01\ \text{eV}$$

$$e + Ar(1p_0) \overset{k_e^{Ar(2p_1)}}{\rightarrow} Ar(2p_1) + e,\ \varepsilon^*_{thr} = 13.5\ \text{eV}$$

where $k_e^{O(3p)}$ and $k_e^{Ar^{(2p_1)}}$ represents the direct excitation rate constants for populating the $O(3p^3P)$ and $Ar(2p_1)$ levels respectively, $k_{diss}^{O(3p)}$ is the dissociative excitation rate constant for $O(3p^3P)$ and ε^*_{thr} is the excitation threshold energy. Optical emission then occurs according to

$$O(3p^3P) \overset{A_{ij}^{O(3p)}}{\rightarrow} O(3s^3S) + h\nu(844.67\ \text{nm})$$

$$Ar(2p_1) \overset{A_{ij}^{Ar^{2p_1}}}{\rightarrow} Ar(1p_0) + h\nu(750.38\ \text{nm})$$

where the spontaneous emission rates for both the $O(3p^3P) \rightarrow O(3s^3S)$ and $Ar(2p_1) \rightarrow Ar(1p_0)$ transitions are denoted by $A_{ij}^{O(3p)}$ and $A_{ij}^{Ar(2p_1)}$. Including both direct and dissociative excitation pathways for the excited state O(3p ^{3}P), the time averaged 844 nm emission line intensity is

$$I_O^{844} = c_O h\nu_O A_{ij}^O n_e \left(k_e^{O(3p)}[O] + k_{diss}^{O(3p)}[O_2] \right) \tag{2.18}$$

The actinometry model then becomes

$$[O] = \frac{I_O^{844}}{I_{Ar}^{750}} \frac{\eta_{Ar}^{spec}}{\eta_O^{spec}} \frac{h\nu_{Ar}}{h\nu_O} \frac{a_{ik}^{Ar}}{a_{ik}^O} \frac{k_e^{Ar(2p_1)}}{k_e^{O(3p)}}[Ar] - \frac{k_{diss}^{O(3p)}}{k_e^{O(3p)}}[O_2] \tag{2.19}$$

where [Ar] and [O_2] are the densities of argon atoms and oxygen molecules determined using the ideal gas law and the known gas pressure and temperature. In some cases the excited state can decay to several lower levels and can also undergo radiation-less decay i.e. collisional quenching. Therefore, the optical branching ratio, a_{ij}, is introduced to account for these additional de-excitation pathways. The optical branching ratio is given by

$$a_{ij} = \frac{A_{ij}}{A + Q} \tag{2.20}$$

where A_{ij} is the spontaneous emission rate for the observed transition, A represents the total spontaneous emission rate of the excited level and is equal to the sum of all spontaneous emission rates of the excited level to all lower levels which is equivalent to the reciprocal of natural lifetime, τ_i of the excited state i.e. $A = \sum_{j<i} A_{ij} = \tau_i^{-1}$. Q is the total collisional quenching rate of excited level by the main plasma constituents i.e. Ar, O_2 and SF_6 which is evaluated by the product of the known collisional quenching rate constant and number density of the collisional partner and was described by Eqn.(2.2) and Eqn.(2.3) in section 2.2.1. The experimental and physical constants required for determining [O] using Eqn.(2.19) are shown in table 2.1. The

Table 2.1: Physical and experimental constants

Species	η^{spec}	τ_{i}^{-1}	$k_q^{\mathrm{O_2}}$	$k_q^{\mathrm{SF_6}}$	k_q^{Ar}
	(a.u)	(ns)	($\mathrm{cm^{-3}\cdot\ s^{-1}}$)	($\mathrm{cm^{-3}\cdot\ s^{-1}}$)	($\mathrm{cm^{-3}\cdot\ s^{-1}}$)
O(3p)	0.22	35.1[13]	9.40×10^{-10}[13]	20.2×10^{-10}	0.25×10^{-10}[13]
$\mathrm{Ar(2p_1)}$	0.11	24.0[13]	7.60×10^{-10}[13]	7.7×10^{-10}[18]	0.16×10^{-10}[13]

collisional quenching rate constant for the $\mathrm{O(3p^3P)}$ state by $\mathrm{SF_6}$ molecules was determined using TALIF and was described in section 2.2.3.

The relevant excitation cross-sections used for determining the excitation rate constants for Eqn.(2.19) are shown in figure 2.9. The direct excitation cross-sections for $\mathrm{O(2p^4 \rightarrow 3p)}$ and $\mathrm{Ar(1p^0 \rightarrow 2p_1)}$ were taken from [31] and [32] respectively. The dissociative excitation cross-section was taken from [33]. In this thesis actinometry was used for measuring atomic oxygen density in various mixtures of $\mathrm{O_2/SF_6/Ar}$ plasma at 100 mTorr and relative variations of fluorine density in $\mathrm{SF_6/O_2/Ar}$ (85/10/5 %) plasma at 100 mTorr. The details of fluorine actinometry is discussed in section 2.3.2. The excitation rate constants required for determining [O] with actinometry were calculated using Langmuir probe measured EEDFs which is discussed in more detail in section 2.5. These excitation rate constants are particularly sensitive to changes in the EEDF. This is evident from figure 2.10 which shows the variation of several excitation rate constant used for oxygen actinometry determined using Maxwellian EEDFs as a function of electron temperature.

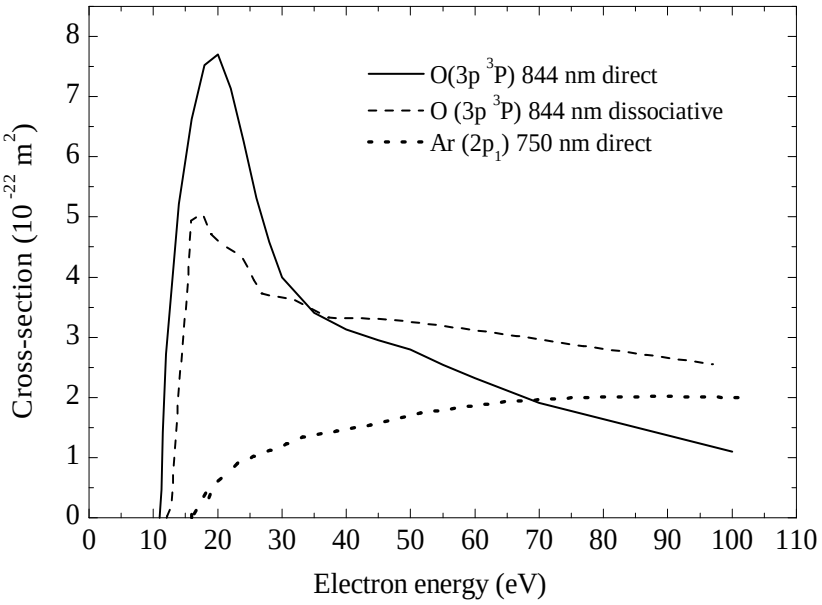

Figure 2.9: Relevant electron impact excitation cross-sections for oxygen actinometry.

2.3.2 Fluorine actinometry

Actinometry can be used to monitor changes in atomic fluorine density as first introduced by Coburn and Chen [30]. The excitation scheme that was used in this work was

$$\mathrm{e} + \mathrm{F}(2\mathrm{p}^5\,{}^3\mathrm{P}^0) \overset{k_e^{\mathrm{F(3p)}}}{\rightarrow} \mathrm{F}(3\mathrm{s}\,{}^2\mathrm{P}^0) + \mathrm{e}, \quad \varepsilon_{thr} = 14.74 \text{ eV}$$

$$\mathrm{F}(3\mathrm{s}^2\mathrm{P}^0) \overset{A_{ij}^{\mathrm{F(3p)}}}{\rightarrow} \mathrm{F}(3\mathrm{s}\,{}^2\mathrm{P}) + h\nu(703.7 \text{ nm})$$

where $k_e^{\mathrm{F(3p)}}$ is the excitation rate constant for the $\mathrm{F}(2\mathrm{p}^5 \rightarrow 3\mathrm{s}^2\mathrm{P}^0)$ transition and $A_{ij}^{\mathrm{F(3p)}}$ is the spontaneous emission rate of the $\mathrm{F}(3\mathrm{s}^2\mathrm{P}^0)$ level. Emission at 750 nm from the excited $\mathrm{Ar}(2\mathrm{p}_1)$ atom was used as the actinometer. One major limitation of fluorine actinometry is that there is no measured excitation cross-sections for the $\mathrm{F}(2\mathrm{p}^5\,{}^3\mathrm{P}^0 \rightarrow 3\mathrm{s}\,{}^2\mathrm{P}^0)$ transition. Therefore, absolute [F]

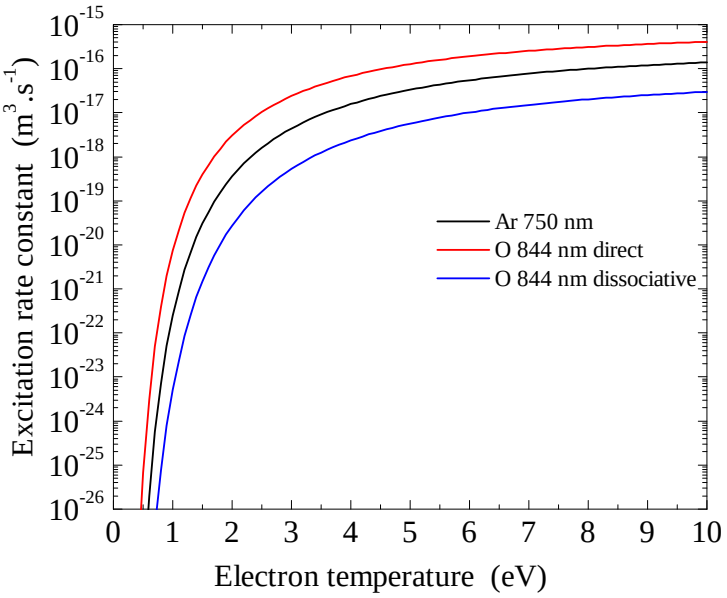

Figure 2.10: Relevant electron impact excitation rate constants for oxygen actinometry as a function of electron temperature (determined with Maxwellian EEDFs).

can not be determined using the classic actinometry model as previously described in section 2.17 due to the unknown fluorine excitation rate constant. Although, attempts [34] have been made to indirectly determine the ratio $k_e^{\mathrm{Ar(2p_1)}}/k_e^{\mathrm{F(3p)}}$, which is often referred to as the constant of proportionality, K, using a combination of an independent absolute measurement of [F] (i.e. VUV absorption) and also the emission line ratio $I_{\mathrm{F}}^{703}/I_{\mathrm{Ar}}^{750}$. The classic actinometry model can then be used to calculate K provided [F]$\propto I_{\mathrm{F}}^{703}/I_{\mathrm{Ar}}^{750}$, a plot of [F] versus [Ar]$I_{\mathrm{F}}^{703}/I_{\mathrm{Ar}}^{750}$ yields a straight line through the origin with the slope equal to K. It was shown that K was sensitive to changes in the feedstock mixture and pressure. Furthermore, it was shown that the classic actinometry model was violated for certain conditions and $I_{\mathrm{F}}^{703}/I_{\mathrm{Ar}}^{750}$ was not proportional to [F]. This is indicative of an additional excitation mechanism

such as dissociative excitation. No attempts were made in this work to provide absolute [F] using (2.17). This is because the published values of K are EEDF dependant and are specific to the discharge type, feedstock, pressure and power for which they were measured in. Only the fluorine actinometric signal, $I_{\mathrm{F}}^{703}/I_{\mathrm{Ar}}^{750}$ was used to monitor relative changes of [F], therefore it was assumed that additional excitation mechanisms for $\mathrm{F}(2\mathrm{p}^5\,{}^3\mathrm{P}^0)$ and $\mathrm{Ar}(2\mathrm{p}_1)$ excited atoms were negligible and that the EEDF remained fixed over the plasma conditions explored.

To summarize the basic requirements necessary for actinometry to provide relative or absolute concentration of reactive species are

1. The excited states of both the species of interest and the actinometer are produced by direct electron impact excitation from the ground states, i.e. population via cascades, metastables and resonant enhanced quenching is negligible.

2. The actinometric model must include process rates such as dissociative excitation and quenching when such processes are significant.

3. The electron impact excitation cross-sections for both the species of interest and the actinometer have similar energy dependences and thresholds energies.

4. The EEDF and [Ar] must be constant and dissociative excitation must be negligible for estimating relative density variation using the actinometric signal ($I_{\mathrm{X}}/I_{\mathrm{Ar}}$).

5. For estimating absolute densities the EEDF and excitation cross-sections for direct and dissociative excitation processes must be known.

2.3.3 Optical detection system for actinometry

The optical detection system used was a Horiba Jobin Yvon spectrometer (MicroHR) which consists of an automated scanning monochromator in the CzernyTurner optical layout with a focal length of 140 mm. This spectrometer was equipped with a CCD detector (Toshiba TCD1304AP) and the spectral resolution of this device was 0.25 nm. Figure 2.11 shows a basic schematic of the optical arrangement used for actinometry experiments. The plasma induced emission was viewed through a UV grade quartz optical viewport onto the entrance slit of the monochromator. The monochromator was scanned only over the spectral region of interest i.e. 700 - 900 nm. A correction was applied to the line intensities of interest which removes the dependence of the line intensities on the spectral response of the detection system i.e. CCD, monochromator, mirrors and windows. Correcting for the response of the detection system was paramount for the actinometric technique as significant two fold variation in the spectral response was observed between 750 - 850 nm as shown in Table 2.1. A tungsten calibration lamp was used for this calibration which provides the true irradiance of the lamp (for a known distance from the source to detector). However, only a relative spectral response correction was necessary for actinometry, therefore, only the shape of the spectral lamp output was required which is independent on the separation distance between the spectrometer and the lamp. This calibration technique was similar to previous workers [35–37].

2.4 Mass spectrometry

Mass spectrometry (MS) is a useful plasma diagnostic technique that can be used to detect various plasma species such as atomic and molecular neutrals,

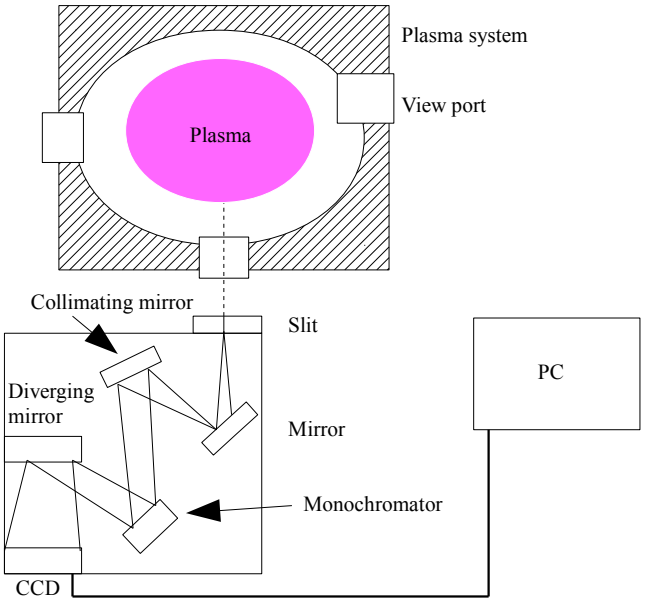

Figure 2.11: Basic schematic of the optical arrangement for actinometry.

positive and negative ions and also metastables. A commercial mass spectrometer from Hiden Analytical Ltd [38] (EQP 300) was used in this work which has a quadrupole type filter and can be used in various modes such as RGA (residual gas analysis) for detection of neutral species and SIMS for positive/negative ion detection. However, only the RGA mode was used in this work. This series of mass spectrometers from Hiden Analytical allows the sampling head to be inserted directly into the plasma region. This is possible as the sensitive probe is contained within a metal enclosure which is differentially pumped with a turbo molecular pump backed by a rotary vane pump. The EQP can reach pressures as low as $\approx 5 \times 10^{-6} - 1 \times 10^{-8}$ Torr depending on the pressure of the process chamber. A sampling orifice

was also incorporated into the enclosure with the ionization source $\approx$ 3 cm behind the orifice for good sensitivity.

A popular alternative is to place the probe into a separate chamber connected to the plasma chamber [39–41]. An aperture incorporated into the wall of the plasma chamber allows the gas to leak into the separate chamber and subsequently into the probe which is in line of sight with the aperture. A major drawback of this method is that a significant background signal can be produced, and therefore, this approach requires several stages of pumping and careful vacuum design in order to provide sufficiently high beam to background signal ratio which can be expensive and experimentally challenging [39–41].

A simplified schematic of key features of the EQP 300 is shown in figure 2.12. The EQP 300 was positioned in the radial direction and was connected to the reactor wall using a KF 40 access port. The diameter of the orifice used in this work was 150 μm. The orifice was positioned downstream ($\approx$ 15 cm) from the outer edge of the plasma region due to physical restrictions with vacuum connections. Neutral species effuse from the plasma through the sampling orifice and into the ionization source of the probe. The ionizing electrons were generated with oxide coated iridium filaments and were accelerated towards an ionizer cage by a potential applied across the cage and filament. The ionizing electrons have an energy spread which is assumed to be in the form of a Gaussian distribution with a half width of $\approx$ 0.5 eV [42]. Ions are then guided with electrostatic lenses to a triple filter quadrupole mass analyzer. Detection of the ions was achieved with a secondary electron multiplier (SEM). No repelling potential on the extractor lens was necessary since plasma ions, photons or metastables could not reach the SEM. This was confirmed as no signals were detected for any m/e while the SEM detector

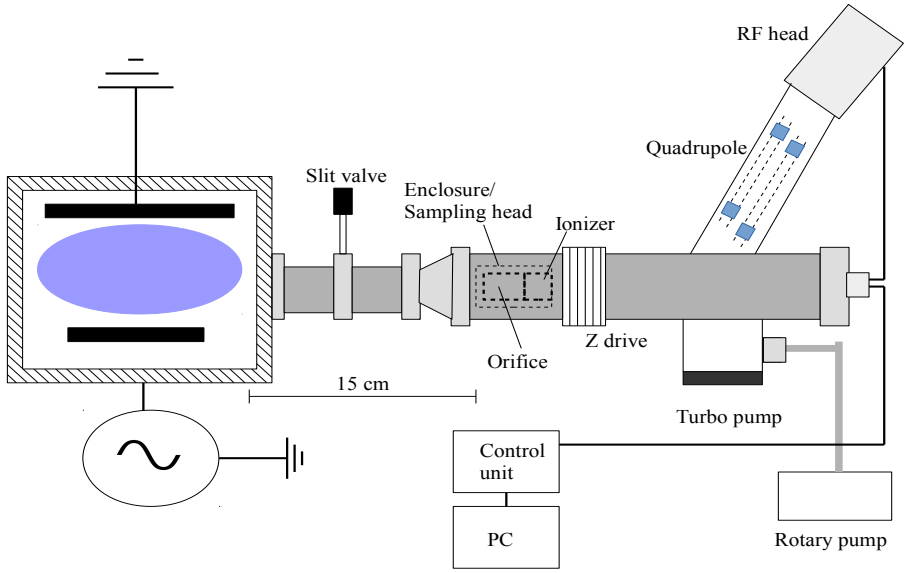

Figure 2.12: Basic schematic of a mass spectrometer used in RGA mode

was on and the filaments were off during plasma operation.

2.4.1 Appearance potential mass spectrometry

Appearance potential mass spectrometry (APMS) was used in this work for the detection of atomic fluorine density. APMS differs from traditional residual gas analysis (RGA) as ionization of neutrals is performed with selective electron energies instead of electrons with fixed energy (typically 70 eV) as used in standard RGA. Controlling the kinetic energy, ε, of the filament generated electrons can be used to discriminate the measured ion signal from processes such as dissociative ionization i.e. $e + X_2 \rightarrow 2e + X^+ + X$. Thus, in the case measuring fluorine atoms in SF_6 plasma the signal from dissociative

ionization i.e. $e + SF_6 \rightarrow F^+ + SF_4 + 2e$ ($\varepsilon = 23.0$ eV) can be ignored by measuring the F^+ signal for electron energies less than 23.0 eV.

If the species of interest, X, originates from its parent molecule, X_2, where $[X_2] \gg [X]$ then the measured ion signal, is proportional to [X] for $\varepsilon_{thr}^{X \rightarrow X^+} < \varepsilon < \varepsilon_{thr}^{X_2 \rightarrow X^+}$. In the case of $[X_2] \gg [X]$, the measured ion signal for $\varepsilon > \varepsilon_{thr}^{X_2 \rightarrow X^+}$ is proportional to $[X_2]$. An example of this dissociative ionization contribution is evident by the N^+ ion signal as function of electron energy in an N_2 plasma as shown in figure 2.13. This appearance potential scan was taken with the EQP 300 in an N_2 plasma (Oxford instruments CCP) operated at 150 mTorr and 200 W. The direct and dissociative appearance

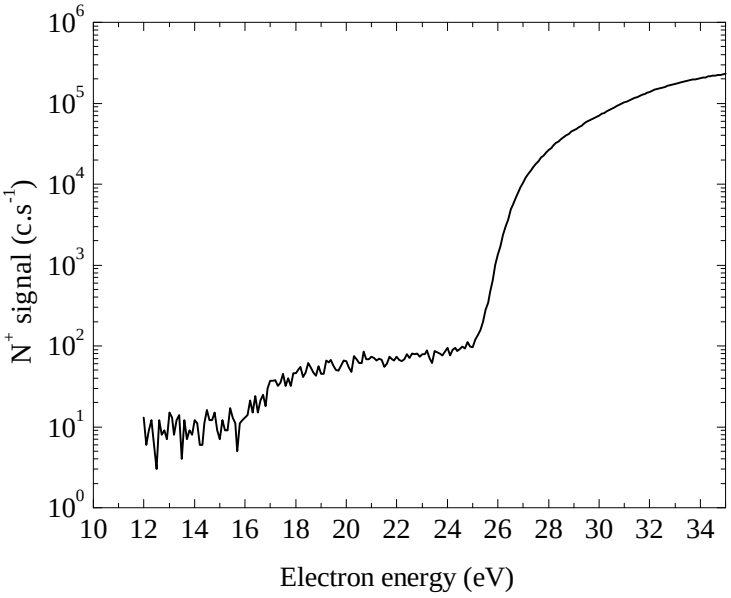

Figure 2.13: Appearance potential scan of nitrogen ions $m/e = 14$ in N_2 plasma operated at 150 mTorr and 200 W. The significant inflection of N^+ at ≈ 25.2 eV is from dissociative ionization of N_2

potentials, ε_{thr}, of N^+ are

$$e + N \rightarrow N^+ + 2e \quad \varepsilon_{thr}^{N \rightarrow N^+} = 14.53 \text{ eV [43]}$$

$$e + N_2 \rightarrow N + N^+ + 2e \;\; \varepsilon_{thr}^{N_2 \rightarrow N^+} = 25.2 \text{ eV [44]}$$

The significant change of the slope of the N^+ signal as a function of electron energy at $\approx$ 25 eV is due the contribution of dissociative ionization of N_2 which produces a N^+ at $m/e = 14$. Therefore the N^+ signal that is proportional to [N] is for electron energies 14.53 - 24.53 eV.

2.4.2 Calibration technique for absolute atomic fluorine density

There are several mechanisms for which F^+ ions can be produced within the ionization source of the mass spectrometer. These processes and their appearance potentials are

1. $e + F \rightarrow F^+ + 2e$, $\varepsilon_{thr}^{F \rightarrow F^+} = 15.5$ eV [45]
2. $e + F_2 \rightarrow F^+ + F + 2e$, $\varepsilon_{thr}^{F_2 \rightarrow F^+} = 21.0$ eV [46]
3. $e + SF_6 \rightarrow F^+ + SF_4 + 2e$, $\varepsilon_{thr}^{SF_6 \rightarrow F^+} = 23.0$ [47]

In principle, APMS allows direct measurement of fluorine atoms because the ionization potential for direct ionization of fluorine atoms is lower than the dissociative ionization processes i.e. $\varepsilon_{thr}^{F \rightarrow F^+} < \varepsilon_{thr}^{F_2 \rightarrow F^+}$ and $\varepsilon_{thr}^{F \rightarrow F^+} < \varepsilon_{thr}^{SF_6 \rightarrow F^+}$. The energy separation between processes (1) and (2) is much greater than the FWHM of the Gaussian energy distribution of the ionizing electrons and energy resolution (0.1 eV) to allow reliable electron energy scanning. An example of a typical electron energy scan on fluorine atoms is shown on figure 2.14, three F^+ signals are shown these are the plasma on, U_{ON}, plasma off, U_{OFF}, and residual signals, U_{RES}. The residual signal is an always present source of contamination from a fluorine containing substance. This signal is

not necessarily constant and can increase depending on the level of contamination and the exposure time of the mass spectrometer to chemically reactive plasmas such as SF_6 plasma. It is detected even with no gas flow into the mass spectrometer. Given the reactive nature of fluorine atoms, this signal is probably caused by desorbed fluorine atoms or fluorine containing molecules from the inner surfaces of the mass spectrometer i.e. filaments/ionization source.

The plasma off signal is obtained by sampling the feedstock gas with the rf power off. This 'background signal' for $\varepsilon_{thr}^{F\rightarrow F^+} < \varepsilon_{thr}^{F_2\rightarrow F^+}$ is believed to be caused by thermal pyrolysis of SF_6 molecules on the filaments. Although not typically discussed, it is also possible that this background signal can be generated from neutral dissociation processes such as SF_6 + e $\rightarrow$ F + SF_5 + e and SF_6 + e $\rightarrow$ 2F + SF_4 since the threshold energies for these reactions are lower than the ionization potential of fluorine atoms i.e. 9.6 and 12.1 eV respectively [45]. These instrument produced fluorine atoms can then be ionized which contribute to the background signal. The plasma off signal was observed to increase with increasing SF_6 partial pressure. This confirms that pyrolysis and possibly neutral dissociation are responsible for the plasma off signal for $\varepsilon_{thr}^{F\rightarrow F^+} < \varepsilon_{thr}^{F_2\rightarrow F^+}$. A similar affect was also observed in a separate experiment while measuring the background signal of O^+ with increasing O_2 content. For $\varepsilon > \varepsilon_{thr}^{SF_6\rightarrow F^+}$ the plasma off signal will be dominated by dissociative ionization due to the relatively high abundance of F_2 and SF_6 compared to fluorine atoms.

Finally, the plasma on signal is the sum of residual, background signal and also the contribution from fluorine atoms emanating from the plasma. The background signal shown on figure 2.14 was recorded with a gas mixture of SF_6/O_2/Ar (85/10/5 %) operated at 40 mTorr, and the plasma on was

recorded under the same conditions and with a power of 250 W. Above 21

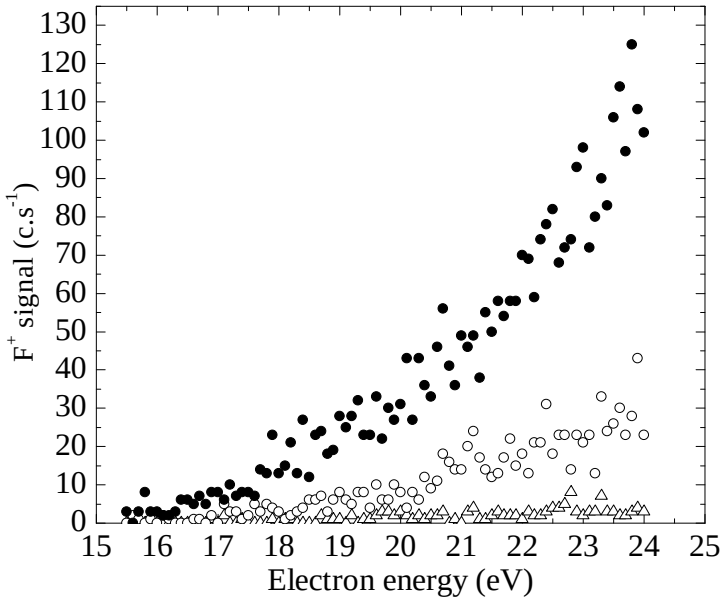

Figure 2.14: Appearance potential scan of fluorine ions, three signal are shown these are: the residual signal (△), background signal (∘) and plasma on signal (•).

eV the plasma on signal is dominated by process (2). For particular plasma conditions, a clear inflection in the signal at $\approx$ 21 eV was observed which indicates a relatively large abundance of F_2 in the discharge. This implies that process (2) can be significant and that the appearance potentials scans need to be performed between $\varepsilon_{thr}^{F\rightarrow F^+} - \varepsilon_{thr}^{F_2\rightarrow F^+}$ and not $\varepsilon_{thr}^{F\rightarrow F^+} - \varepsilon_{thr}^{SF_6\rightarrow F^+}$. Finally, the signal which is proportional to [F] is the difference between the plasma on and plasma off signals for electron energies in the range of 17.5 - 21.0 eV.

A correction factor was applied to the background signal which accounts for the depletion of the neutral gas density induced by gas heating when the discharge is switch on. The depletion of the gas density was determined

based on estimates of the gas temperature and the ideal gas law. This correction was determined assuming a proportional relationship between the background signal and [SF_6]. Based on previous TALIF (O atoms) and thermocouple measurements [48] on the same plasma reactor, the maximum gas temperature of 365 K was measured. The signal proportional to [F] is given as $U^{F^+}(\varepsilon) = U_{ON}(\varepsilon)$ - $0.78U_{OFF}(\varepsilon)$. The correction factor of 0.78 was calculated assuming a gas temperature of 365 K corresponding to 22 % decrease in the gas density and thus, background signal. This relatively simple correction technique does not significantly affect the results in the current experimental set up due to the sufficiently large difference between the plasma on and background signal i.e. $U_{ON}(\varepsilon)/U_{OFF}(\varepsilon) \approx 3$ - 6. After correcting the background signal it was found that [F] increased by $\approx$ 10 % for $U_{ON}(\varepsilon)/U_{OFF}(\varepsilon)$ $\approx$ 3 and increased only by $\approx$ 3 % for $U_{ON}(\varepsilon)/U_{OFF}(\varepsilon) \approx 6$.

There is some ambiguity about the direct ionization potential of fluorine atoms. Often, 17.42 eV is taken as the appearance potential of fluorine ions as determined by spectroscopic methods [49]. However, the appearance potential of fluorine ions was found at $\approx$ 15 eV based on the experimental ionization cross-sectional data [50]. Also, a separate study determined the appearance potential of fluorine ions at 15.5 $\pm$ 0.25 eV [45]. No signals were detection in the range of 15 - 16 eV in this study which was probably due to small signals at such low electron energies and the low concentration of fluorine atoms in CCP.

The measured ion signal, U^{X^+}, is related to the number density, [X], in the ionizer by

$$U^{X^+}(\varepsilon) = \beta\theta(m_X)T(m_X)I_e\sigma_e^+(\varepsilon)l_{ionizer}[X] \tag{2.21}$$

where β is the extraction efficiency of the ions, $\theta(m_X)$ is the mass dependent detection efficiency of the SEM, $T(m_X)$ is the mass dependent transmission

efficiency of the quadrupole, I_e is the electron emission current, $\sigma_e^+(\varepsilon)$ and $l_{ionizer}$ are the ionization cross-section and length of the ionizer respectively. In this work, the fluorine ion signal, $U^{\mathrm{F}\rightarrow\mathrm{F}^+}$, was calibrated by a comparative measurement of an argon ion signal, $U^{\mathrm{Ar}\rightarrow\mathrm{Ar}^+}$, for a known argon density. Taking the ratio of both ion signals allow [F] to be evaluated using [40]

$$[\mathrm{F}] = \left(\frac{N_{\mathrm{F}}}{N_{\mathrm{Ar}}}\right)\left(\frac{\lambda_{\mathrm{Ar}}}{\lambda_{\mathrm{F}}}\right)\left(\frac{T(m_{\mathrm{Ar}})\theta(m_{\mathrm{Ar}})}{T(m_{\mathrm{F}})\theta(m_{\mathrm{F}})}\right)[\mathrm{Ar}] \tag{2.22}$$

where N_{F} and N_{Ar} are the slopes of linear fits to the measured signal for fluorine and argon as a function of electron energy and λ_{F} and λ_{Ar} are the slopes of linear fits to the known ionization cross-sections for fluorine and argon atoms as a function of electron energy. The signals and cross-sections can be approximated using these slopes since they both scale linearly for typically several electron-volts above the ionization potential. Good agreement was found between both the measured F^+ signal and fluorine atom ionization cross-section as a function of electron energy as shown in figure 2.15.

The electron emission current was fixed at 100 μA for both experiment and calibration, therefore I_e and $l_{ionizer}$ can be ignored from Eqn.(2.22). Similarly, the extraction efficiency of the ions (β) is unity for all direct ionization processes [40] and can also be neglected from Eqn. (2.22). $U \propto I_e$ for a fixed electron energy until a point where space charge effects begin to reduce the signal intensity [41]. Space charge effects were not present in this device below 200 μA. However, operating with I_e less than 100 μA was recommended by the manufacturer to preserve the lifetime of the filaments in chemically aggressive environments.

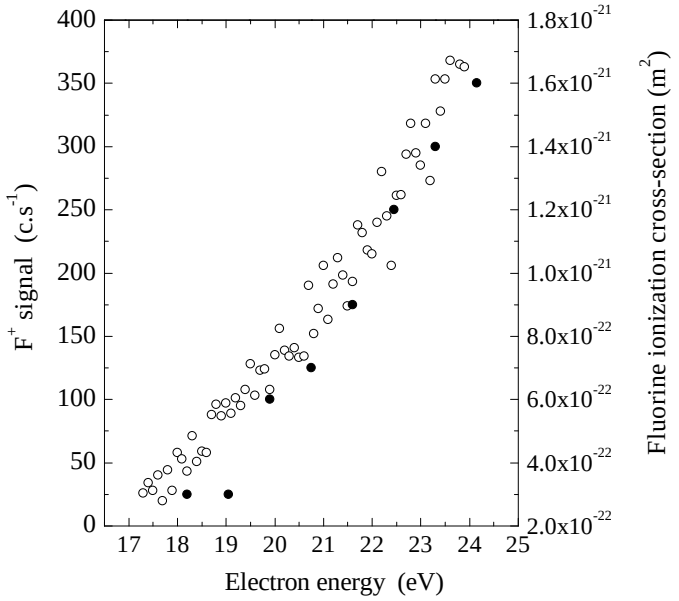

Figure 2.15: The F^+ signal and atomic fluorine ionization cross-section as function of electron energy.

2.4.3 Mass spectrometer instrument response function

The unknown mass dependent instrument parameters such as $\theta(m_X)$ and $T(m_X)$ were determined by a separate calibration procedure using several gases of known density. The gases used for this procedure was He, N_2, O_2, and Ar. Electron energy scans were recorded for each gas individually at a known pressure of 40 mTorr. In this work [He], [N_2], [O_2] and [Ar] was calculated using the ideal gas law assuming a gas temperature of 300 K and the emission current was fixed for each measurement. $T(m_X)\theta(m_X)$ was evaluated for 4, 28, 32, and 40 amu using,

$$T(m_X)\theta(m_X) = \frac{N_X}{\lambda_X[X]} \tag{2.23}$$

All other mass spectrometer settings were kept the same for this calibration and for the experiments. The ionization cross-sections used for He and Ar

were taken from Wetzel *et al* [51] and cross-sections for N_2 and O_2 were taken from Straub *et al* [52]. Only singly charged species were considered for this calibration. Figure 2.16 shows the product of $\theta(m_X)$ and $T(m_X)$ versus ion mass, m, a curve fit (power law) to the experimental data is also shown in this figure which allows for $T(m)\theta(m)$ to be determined for any singly charged ion with a mass between 4 - 40 amu.

The dependence of $T(m)\theta(m)$ varied with $m^{-0.75}$. This agrees well with pre-

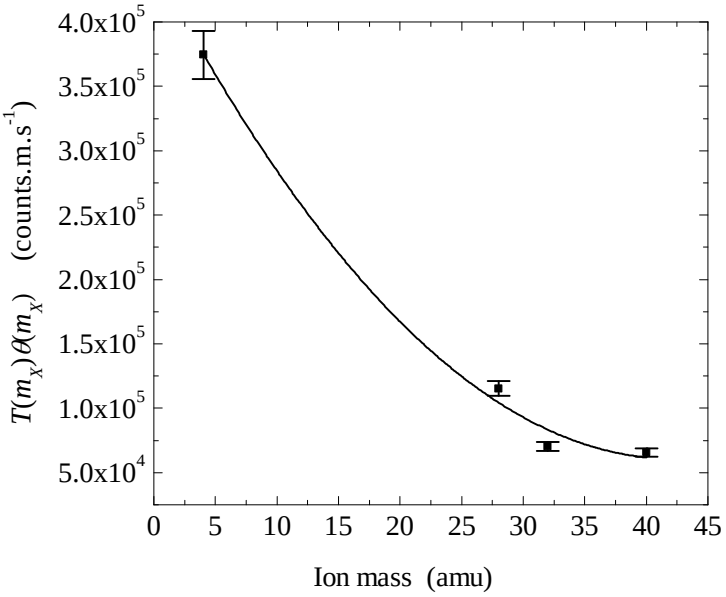

Figure 2.16: The product of the mass dependant transmission efficiency and mass dependant detection efficiency as a function of atomic mass unit.

vious measurements. For example, Pulpytel *et al* [53] found a dependence of $T(m)\theta(m)$ as $m^{-0.85}$ and similarly Singh *et al* found $T(m)\theta(m)$ to vary as $m^{-0.81}$ [40]. For this mass spectrometer it was found that the required $T(m_{Ar})\theta(m_{Ar})/T(m_F)\theta(m_F)$ for Eqn.(2.22) was ≈ 0.35.

2.5 The Langmuir probe

Langmuir probes, invented by Nobel prize winning physicist Irvine Langmuir, are one of the most commonly used and oldest diagnostic technique for plasma. The probe can be used to measure key plasma parameters such as electron and ion density, electron temperature, plasma and floating potential and the electron-energy distribution function. In this work a Langmuir probe was used to investigate the electron kinetics in O_2 and Ar plasma over a wide range of powers and pressures. The pressure and power evolution of parameters such as n_e, T_{eff} and EEPFs were examined in order to investigate various plasma phenomena such electron heating mechanisms and mode transitions i.e. $\alpha - \gamma$ transition. Important plasma quantities such as reaction rate constants (excitation, dissociation) require knowledge of the EEDF. In particular, the O_2 dissociation rate constant and excitation rate constants relevant for oxygen actinometry were calculated using EEDFs measured with a Langmuir probe in this work. Furthermore, the variation of n_e, T_{eff} for various mixtures of O_2/SF_6 was investigated in this work with the use of a Langmuir probe.

2.5.1 Probe theory

A Langmuir probe can be defined as a conductor immersed in plasma which is biased positively or negatively for the purpose of drawing electron or ion current. A current-voltage (IV) characteristic is measured which can be used to determine plasma parameters. Shown in figure 2.17 is an example of a cylindrical Langmuir probe IV trace recorded in an O_2 plasma. This IV trace can be separated into three regions which are separated according to

the floating potential, V_f, and the plasma potential. These regions are:

The ion saturation region (I): For large negative probe potentials, V_b, i.e. $V_b \ll V_f$ the current drawn is predominately from positive ions. Electrons do not have sufficient energy to reach the probe, however, very energetic electrons can reach the probe as V_b is increased towards V_f.

The electron retardation region (II): This region is defined for $V_f \leq V_b \leq V_p$ where a repelling potential exists for electrons. An equal flux of positive and negative charge reach the probe for $V_b = V_f$, here, the total probe current, I_T, is zero. Electrons can reach the probe for $V_b > V_f$ and some of which are repelled until $V_b = V_p$. For an electron to reach the probe in this retarding region the kinetic energy, ε, must be greater than or equal to $(V_b - V_p)$.

The electron saturation region (III): No electrons are repelled for $V_b > V_p$. Depending on the geometry of the probe tip, the electron saturation current can either saturate or continue to increase due to an increase in the effective collection area. Figure 2.17 shows an example an increase in the probe current for $V_b > V_f$. Constant saturation is only observed in planar probe geometries.

Langmuir probes have been studied extensively since 1926 and many theories have been developed. Although, a Langmuir probe is simply a conducting wire immersed in plasma, the relevant theories for determining plasma parameters can be complex. Such theories that have been developed are based on the nature of sheath surrounding the probe tip and on many parameters such as the probe radius and length, mean free paths for electron-neutral,

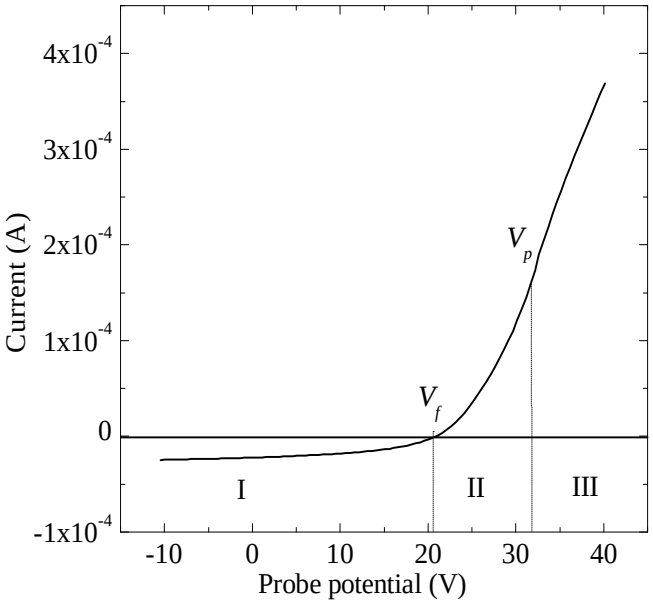

Figure 2.17: Langmuir probe IV trace recorded in an O_2 CCP operated at 10 mTorr and 30 W. Region (I) corresponds to the ion saturation region, (II) is the electron retardation region and (III) is electron saturation region

ion-neutral and ion-ion collisions, plasma density, Debye length and electron and ion temperatures. Various models such as orbital motion limited (OML) for electron collection in the electron saturation region and for ion collection in the ion saturation region and the Langmuir procedure for determining charged particle densities and temperatures have been reviewed by Godyak *et al* [54]. It was shown that some of these theories can result in considerable error in the calculated plasma parameters in non-Maxwellian plasmas. Therefore, the use of such theories are not reliable since electrons in low pressure CCP are rarely in thermal equilibrium and are usually characterized by non-Maxwellian energy distributions such as Druyvesteyn and bi-Maxwellian. In this work the Druyvesteyn method was used to determine n_e, T_e and the EEDF. This is the most widely used method for determin-

ing electron plasma parameters in processing plasmas since it is independent on the particular shape of the electron energy distribution and can relate directly to the second derivative of the measured electron current with respect to probe voltage, d^2I_e/dV_b^2 to the EEDF. The Druyvesteyn formula for calculating $f_e(\varepsilon)$ is

$$f_e(\varepsilon) = \frac{2m}{e^2 A_{PT}} \left(\frac{2e\varepsilon}{m_e}\right)^{1/2} \frac{d^2 I_e}{dV_b^2} \tag{2.24}$$

where ε is equal to $V_p - V_b$, m_e is the electron mass, e is the charge of an electron and A_{PT} is the area of the probe. It is common to express this electron distribution as the electron energy probability function, $f_p(\varepsilon)$, (EEPF) which is given by

$$f_p(\varepsilon) = (\varepsilon)^{-1/2} f_e(\varepsilon) \tag{2.25}$$

It is convenient to use the EEPF to determine if the energy distribution is Maxwellian or Druyvesteyn. The distribution is Maxwellian if a plot of $\ln f_p(\varepsilon)$ versus ε is a straight line and Druyvesteyn if $\ln f_p(\varepsilon)$ versus ε^2 is represented by a straight line. The energy distribution is either Maxwellian or Druyvesteyn if such plots can be approximated by a straight lines. The electron density can be calculated based on the EEDF and is

$$n_e = \int_0^\infty f_e(\varepsilon) d\varepsilon \tag{2.26}$$

and the average electron energy, $\langle\varepsilon\rangle$, in electron volts is

$$\langle\varepsilon\rangle = \frac{1}{n_e} \int_0^\infty \varepsilon f_e(\varepsilon) d\varepsilon \tag{2.27}$$

The electron temperature, T_e, of plasma electrons is strictly a valid concept when the electrons are in thermal equilibrium with each other and have a Maxwellian distribution. Maxwellian electron energy distributions in low

pressure CCP are rarely encountered, therefore the temperature of the electrons is described by an effective electron temperature, T_{eff}, which is defined as [3]

$$T_{eff} = \frac{2}{3}\langle\varepsilon\rangle \tag{2.28}$$

This technique for determining the EEDF, n_e and T_{eff} is valid for any isotropic electron velocity distribution and is independent of the type of distribution i.e. Maxwellian, Druyvesteyn and bi-Maxwellian and does not depend on the ratio of the probe radius to the Debye length, r_p/λ_D, or T_i/T_e [3].

2.5.2 Determination of the electron current

The Druyvesteyn method requires the electron current only and not the total current to determine the EEPF. This requires removing any contribution from positive ion current to the total current. The theory of Laframboise was used in this work to determine the positive ion current for a cylindrical Langmuir probe which takes the sheath expansion as a function of probe voltage into account. Steinbruchel parametrized numerical results from Laframboise for arbitrary ratios of r_p/λ_D [55]. It was shown that the ion current can be expressed as a function proportional to $a(-X)^b$ where a and b are constants which depend on r_p/λ_D. These constants for a given r_p/λ_D can be found elsewhere [55], however, r_p/λ_D did not exceed ≈ 3 for the conditions explored in this work and a and b can be approximated by 1.15 and 0.5 respectively for r_p/λ_D between 0 - 3 according to [55]. X is a dimensionless probe potential given by

$$X = \frac{e(V_b - V_p)}{k_B T_e} \tag{2.29}$$

Including the ion flux at the sheath edge allows for the ion current, I_i, for a given probe voltage to be given as

$$I_i = -en_i A_{PT} \left(\frac{k_B T_e}{2\pi m_i} \right)^{1/2} a(-X)^b \tag{2.30}$$

where I_i is the positive ion current, T_e is the electron temperature (in Kelvin) and m_i is the ion mass. Only the mass of the most dominant positive ion is used i.e. O_2^+ for O_2 plasma and Ar^+ for an Ar plasma. The ion current was determined from large negative probe potentials to the plasma potential and the electron current was found by $I_e = I_T - I_i$. At first, it was necessary to analyse the IV trace with both electron and ion contributions i.e. I_T to calculate plasma parameters such as T_{eff}, n_e and V_p. This allows r_p/λ_D to be determined so that the necessary constants a and b required for estimating the ion current using Eqn.(2.30) can be found. In addition, initial estimates of T_{eff} and V_p were required for calculating the dimensionless probe potential using Eqn.(2.29). The plasma parameters were then recalculated by the Druyvesteyn method using the electron current only. An example of the calculated ion current in comparison to the measured (total) probe current in an argon plasma operated at 100 mTorr and 30 W is shown in figure 2.18, the floating and plasma potentials were 24.6 and 31.0 V respectively. Excellent agreement between the calculated ion current and measured ion current was evident for large negative probe potentials. The ion current departs from the total measured current close to the floating potential which indicates the increasing contribution of electron current as the probe-sheath potential barrier for electrons is reduced as V_b becomes more positive.

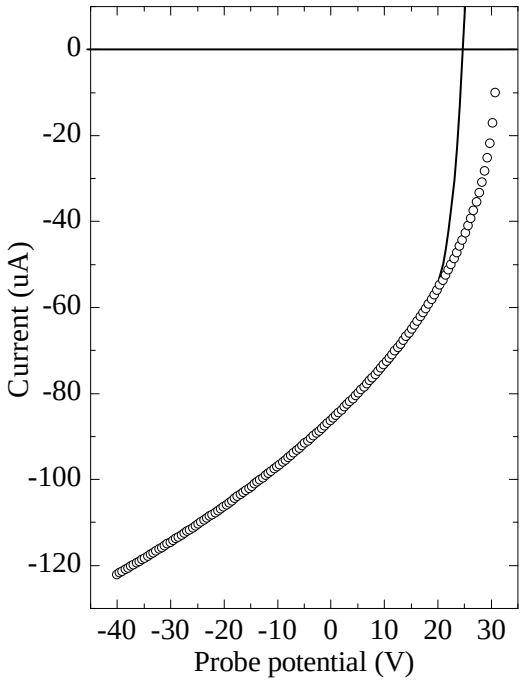

Figure 2.18: Measured probe current (solid line) recorded with the Smart-Probe and the calculated ion current (○) in Ar plasma operated at 30 W and 100 mTorr.

2.5.3 The Smartprobe

The Langmuir probe used in this work was a SmartProbe from Scientific Systems [56]. This probe deploys passive compensation using a compensation electrode and was also equipped with a floating reference probe, the purposes of these are discussed in more detail in sections 2.5.4 and 2.5.5. Figure 2.19 shows a basic schematic of the SmartProbe used in this work.

The probe tip was made from cylindrical platinum wire which was 10 mm in length and 0.15 mm in diameter. Platinum was used to reduce the degree contamination and thus minimize distortion of the IV data. The probe potential was swept from -100 to 100 V and the sampling size was 100 samples

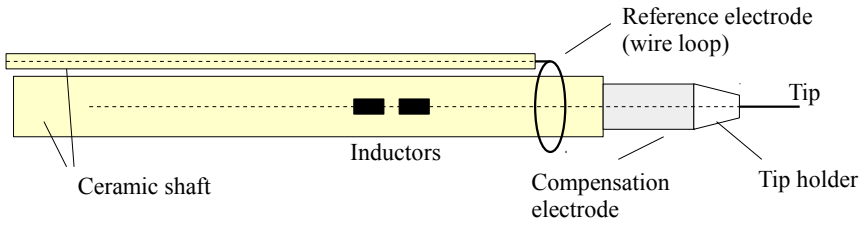

Figure 2.19: Schematic of the SmartProbe from Scientific Systems.

per point, the IV trace used for analysis was an average of ≈ 20 - 30 sweeps. The tip was cleaned before each sweep by electron bombardment until it glowed red hot. This was achieved by biasing the tip positively for ≈ 2 - 3 seconds depending on the plasma density. This procedure ensured a reproducible IV trace was obtained which was free from contaminants such as an oxide layer which has a low conductivity. The tip was replaced regularly to avoid changes in the tip dimensions from etching particularly in reactive plasma such as O_2 and O_2/SF_6 which are studied in this thesis.

2.5.4 Compensation electrode.

Temporal variations in the plasma potential occurs in rf discharges which can produce large errors in the measured plasma parameters determined with a Langmuir probe. Compensation for this variation in V_p can be achieved with a compensation electrode often called 'rf compensation' or 'passive compensation' which allows the probe potential to follow the rf oscillation where it is then filtered out. This compensation technique (passive) was first introduced

by Cagne and Catin [57]. Another technique to overcome this issue is to use active compensation, which directly applies an rf signal to the probe which has an amplitude and phase equal to that of the plasma [58].

The compensation electrode was made from a hollow aluminium cylinder with an area of ≈ 3.5 cm^2, a ceramic tube (isolation dielectric) is placed between the probe and compensation electrode which insulates the probe. The probe is 'forced' to float at the rf potential by configuring the probe circuitry to have probe-plasma impedance, Z_{ps}, much smaller than the probe-ground impedance, Z_{pg}. The rf potential predominantly appears across Z_{pg} and the probe then floats at the plasma potential. This rf oscillation was capacitively-coupled to the probe wire and was filtered with the use of self resonant inductors tuned to 13.56 MHz and associated harmonics. For more details of the probe circuitry refer to [59, 60].

2.5.5 Reference electrode

The SmartProbe was also equipped with a reference probe which is used to track and corrected for changes plasma potential which occurs when the tip is biased. The probe was in the form of a wire loop made from stainless steel and the loop was formed around the main shaft of the probe and the main body of the wire was insulated from the plasma with a ceramic tube ≈ 2 mm in diameter. This wire was connected to an electrical feed-through on a CF flange which was connected to the acquisition unit. Without accounting for such changes in the local plasma potential would lead to large errors in the plasma parameters.

2.6 Hairpin probe

A hairpin probe is a useful plasma diagnostic instrument which measures electron density [61]. The hairpin probe used for this work was developed by Gaman *et al* and more detail can be found [62]. The basic principle of the hairpin probe is that a microwave powered resonator consisting of an antenna immersed in plasma will experience a different resonance frequency, ω_r, compared to the resonance frequency, ω_o, under just vacuum conditions. The electron density, n_e, can be determined by measuring this pair of frequencies and using

$$n_e = \frac{\epsilon_o m_e}{e^2}(\omega^2 - \omega_o^2) \tag{2.31}$$

where ϵ_o is the vacuum permittivity, m_e and e are the mass and charge of an electron respectively.

CHAPTER 3

Investigation of atomic oxygen density in a capacitively-coupled O_2/SF_6 discharge using two-photon absorption laser-induced fluorescence spectroscopy and Langmuir probe

The surface chemistry of plasma reactors plays a critical role in defining the gas-phase plasma chemistry and the flux of reactive species to the material being processed. Also, combining various gases such as O_2/SF_6 and Cl_2O_2 can produce inhibiting layers such as $Si_xO_yF_z$ and $Si_xCl_yO_z$ which allow control of etch profiles. The thickness of these layers are controlled by the concentration of species such as Si, O, F and Cl. Thus, reliable diagnostics to measure these species is critical in understanding various plasma aided processes in IC manufacturing.

Discussed in this chapter is the investigation of absolute atomic oxygen

density in an O_2/SF_6 CCP using two-photon absorption laser-induced fluorescence spectroscopy (TALIF). The variation of atomic oxygen density for various mixtures of O_2/SF_6 was investigated for a fixed pressure and power of 100 mTorr and 100 W respectively. A significant fivefold increase of [O] was observed when an O_2 plasma was diluted with 5 % SF_6. The atomic oxygen density then decreased for gas mixtures greater than 10 % SF_6. The important mechanisms responsible for these findings are explored by investigating the electron kinetics and the reactor wall conditions. Another technique for detection of atomic oxygen density (actinometry) is also reported and compared to TALIF measurements.

3.1 Absolute atomic oxygen in O_2/SF_6 mixtures.

Figure 3.1 shows the variation of absolute atomic oxygen densities for various mixtures of O_2/SF_6. A five-fold increase in [O] was observed as O_2 plasma was diluted with $\approx 5\%$ SF_6. The reason for this rapid increase in [O] is due to a change in the wall loss rate for oxygen atoms caused by the constituents of SF_6 plasma reacting with the reactor walls. The presence of fluorine atoms or fluorine containing substances on the walls inhibits the recombination of oxygen atoms leading to an overall increase in the atomic oxygen concentration within the plasma bulk, this fluorination affect has been well documented [63–65]. The atomic oxygen sticking coefficient is modified when SF_6 is added to the feedstock given the reactive nature of fluorine atoms. This effect was confirmed by direct measurements of the oxygen atom sticking coefficients in both oxygenated (0.5 ± 0.01) and fluorinated (0.09 ± 0.01) reactor walls [66], a marked five-fold variation in the oxygen atom sticking coefficient was ob-

served depending if the walls were fluorinated or not.

The atomic oxygen density decreased steadily as a function of increasing SF_6 after a maximum [O] was reached at 10% SF_6. A possible explanation for this would be because the O_2 partial pressure drops as the SF_6 partial pressure increases; however results shown in section 3.3 suggests an alternative explanation. It is possible that gas-phase reactions could actually be responsible this decreasing trend of [O] between 10 - 60% SF_6.

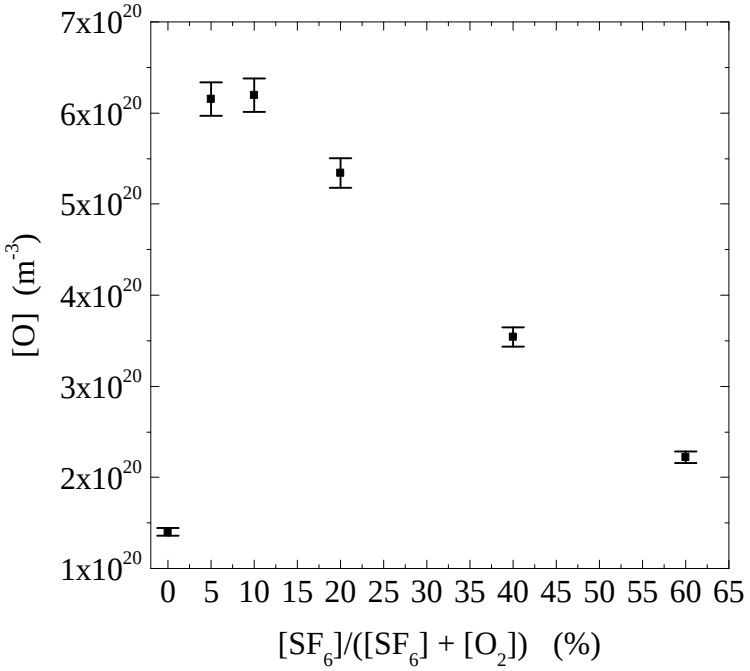

Figure 3.1: Absolute atomic oxygen density variation measured with TALIF for various mixtures of O_2/SF_6. The gas pressure and RF power was 100 mTorr and 100 W respectively.

3.2 Variation of [O] by fluorinating the walls

Direct investigation of the oxygen atom wall loss rate or sticking coefficient requires temporal or spatially resolved measurements of oxygen atoms [66–69]. However, in this work, the effects of a change in the wall conditions was investigated by an indirect method which involves a comparison of [O] measured in a fluorinated reactor to a reference [O] measured when the walls are exposed to an oxygen plasma. These measurements were performed using TALIF and are shown on figure 3.2.

A marked increase in the atomic oxygen density occurs after the reactor walls were fluorinated. The reference plasma conditions prior and post surface fluorination was O_2/Ar (98/2 %) and a fixed gas pressure and power of 400 mTorr and 80 W respectively. The walls were fluorinated by running an O_2/SF_6 (95/5 %) plasma at 100 mTorr and 100 W for 3.0 minutes, this occurred between 20 - 30 minutes as indicated by the dashed lines on figure 3.2. After the surface fluorination process, approximately 7.0 minutes was allowed for reactor walls to return the same temperature as before the fluorination procedure. This eliminates any affects of a change in the gas density induced by changes in the reactor wall temperature. The [O] increased by over a factor of three after the fluorination step which is due to the presence of fluorine atoms or fluorine containing molecules on the walls which impedes surface recombination of oxygen atoms which enhances the [O] within the discharge. It is interesting to observe that [O] does not decay quickly to the reference level after the surface fluorination. Thus, the walls remain fluorinated for a relatively large amount of time ($>$ 20 minutes) which suggests that the fluorine is not easily liberated from the walls for these conditions.

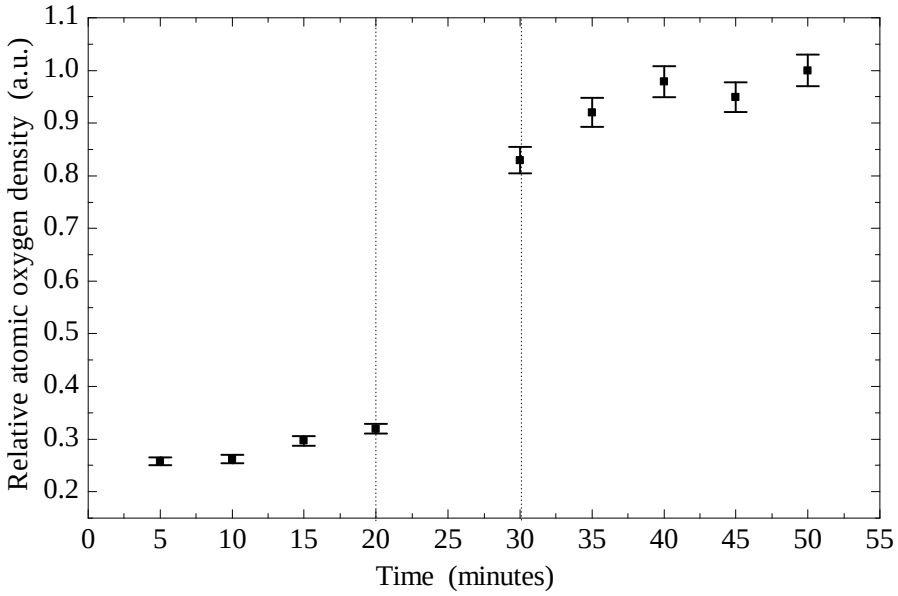

Figure 3.2: TALIF measurements of [O] before and after surface fluorination. [O] increased by over a factor of three after the walls were fluorinated by running an O_2/SF_6 (95/5 %) plasma for three minutes between 20 - 30 minutes as indicated by the dashed lines. The pre and post (5 - 20 and 30 - 50 minutes) fluorinated conditions was O_2/Ar (98/2 %) at 400 mTorr and 80 W.

3.3 Investigation of the electron kinetics and fluorine atom production rates in O_2/SF_6 mixtures.

The dominant generation and loss mechanisms for oxygen atoms in low-pressure O_2 discharges are production via electron impact dissociation of O_2 and destruction by diffusion to walls followed by surface recombination [70]. Section 3.2 presented results highlighting the influence of surface condition

on [O] while in this section the electron impact production of oxygen atoms is explored by investigating the electron kinetics as a function of O_2/SF_6 ratio. The key parameters that were determined were the effective electron temperature, T_{eff}, the electron density, n_e, and the electron energy probability function, $f_p(\varepsilon)$.

3.3.1 Variation of T_{eff} and n_e in O_2/SF_6 mixtures.

The dependence of T_{eff} on the gas composition is shown on figure 3.3, the power and pressure was 100 W and 100 mTorr respectively. A marked increase of the effective electron temperature (0.8 to 3.6 eV) was observed with only a slight change in the gas composition i.e. from pure O_2 to O_2 with 5% SF_6. T_{eff} then reached a maximum of 8 eV at 60% SF_6 which is particularly high for a capacitive discharge given the operating pressure was 100 mTorr. Figure 3.4 shows the variation of n_e for various mixtures of O_2/SF_6 measured with a Langmuir and hairpin probe. A significant decrease in n_e was observed when the oxygen plasma was diluted with SF_6, i.e. the electron density decreased by over a factor of 45 upon diluting the feedstock with 10 % SF_6. Such significant changes in T_{eff} and n_e have been reported elsewhere [71–73] using Langmuir probes and global models and is attributed to electron-attachment processes which results in the formation of negative ions by the consumption of low energy electrons.

3.3.2 Optical investigation of T_{eff} and n_e

The $Ar(2p_1)$ 750 nm emission line intensity was monitored in order to provide an additional method to investigate changes in T_{eff} and n_e. This emission line is frequently used as an actinometer (to correct for variations of the electron density and temperature) as it is primarily excited by electron-impact

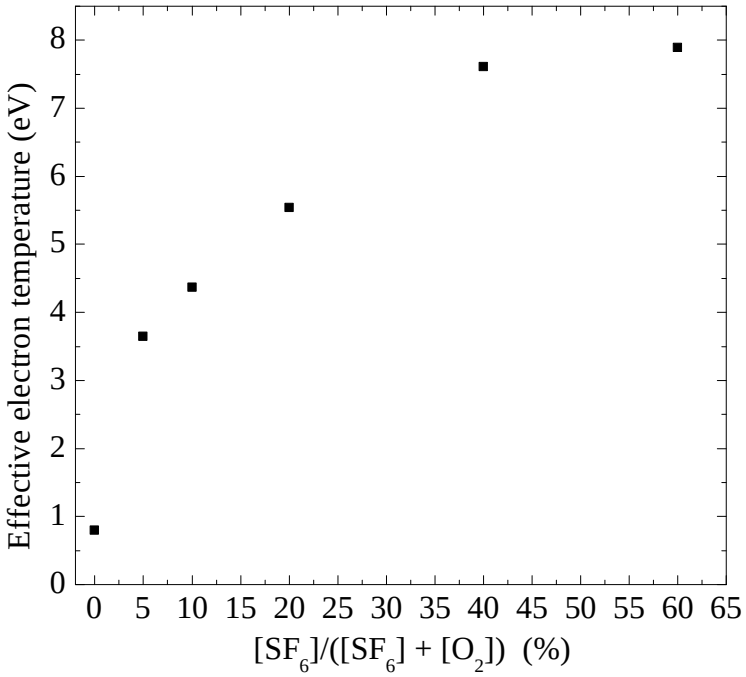

Figure 3.3: The effective electron temperature measured with a Langmuir probe for various mixtures of O_2/SF_6. The gas pressure and RF power was 100 mTorr and 100 W respectively, the error bars are too small to indicate.

with ground state argon and is not influenced (populated) significantly by metastable species or via cascades [74]. Figure 3.5 shows the variation of this optical emission line intensity for the various mixtures of O_2/SF_6 where the argon content was fixed at 3 % and the pressure and power was 100 mTorr and 100 W respectively. The line intensity (750 nm) rapidly increases between 0 - 20 % SF_6 followed by a steady increase with increasing SF_6 content. The behaviour of this line intensity indicates a significant production of electrons with energy greater than the $Ar(1p_0 \rightarrow 2p_1)$ excitation threshold (13.5 eV) as the SF_6 content is increased. This result is in agreement with the variation of the T_{eff} as shown on figure 3.3. The line intensity increased

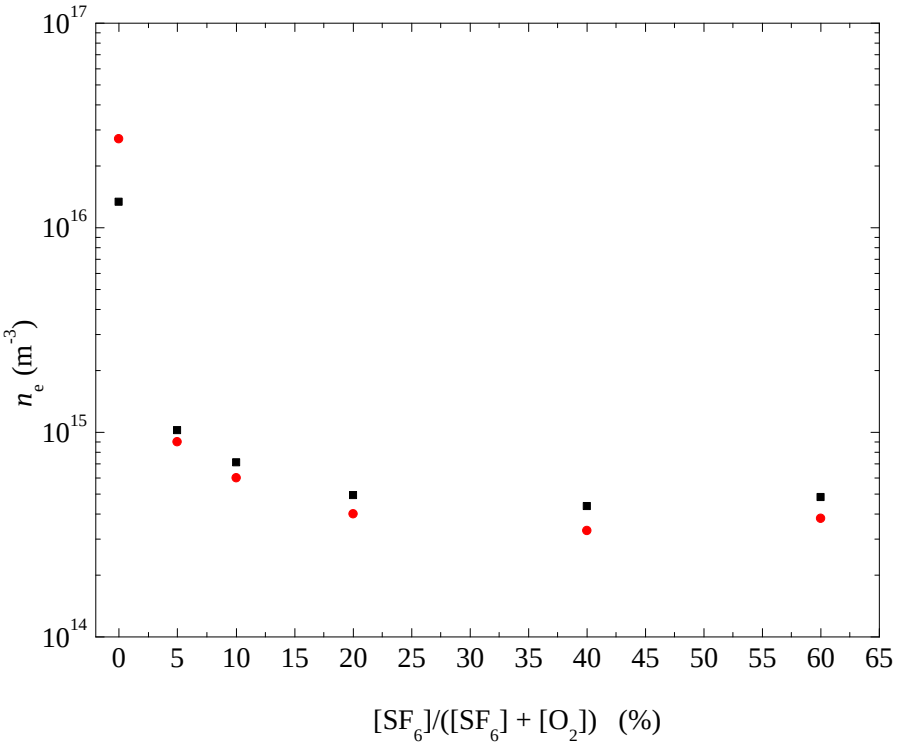

Figure 3.4: The electron density measured with both a Langmuir probe (red) and hairpin probe (black) for various mixtures of O_2/SF_6. The gas pressure and RF power was 100 mTorr and 100 W respectively.

rapidly with SF_6 addition despite the large decrease of the electron density as shown on figure 3.4. This would suggest that the variation of n_e is almost entirely due to low energy electron group with insufficient energy for excitation $<$ 13.5 eV.

Such significant changes in T_{eff} and n_e are caused by electron attachment processes that occur as SF_6 is introduced to the feedstock. As the O_2 plasma becomes diluted with SF_6, attachment processes between the low energy electrons and SF_x (x = 1-6) promotes a significant reduction in the electron density. This dramatic change in n_e is characteristic of SF_6 electronegative

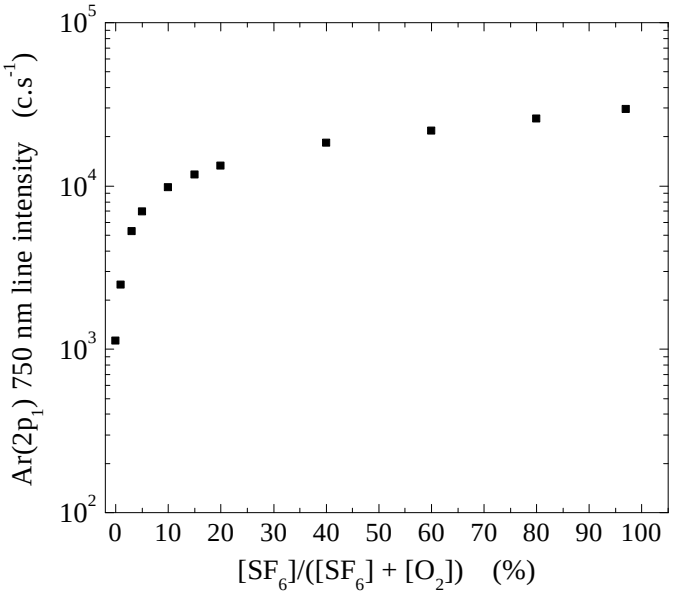

Figure 3.5: The variation of the $Ar(2p_1)$ 750 nm emission line intensity as a function of SF_6 content. The plasma induced optical emission from the plasma bulk was detected with a Horiba Jobin Yvon spectrometer.

discharges and has been observed elsewhere [71, 72, 75]. Furthermore, the cross-sections for electron-attachment reactions are a function of gas temperature [47, 76] and thermocouple measurements indicate that SF_6 containing plasma has a higher translational temperature than pure O_2 plasma. This is another factor that enhances the consumption of plasma electron by attachment with SF_6 molecules which leads to marked decrease of n_e as shown on figure 3.4.

3.3.3 Evolution of the EEPF and atomic oxygen production rates in O_2/SF_6 mixtures.

As discussed in section 3.3, the addition of SF_6 to an O_2 discharge has considerable effects on the electron dynamics and these effects can be summarized by the normalized electron energy probability functions (EEPF) determined with a Langmuir probe shown on figure 3.6. It is clear that a significant frac-

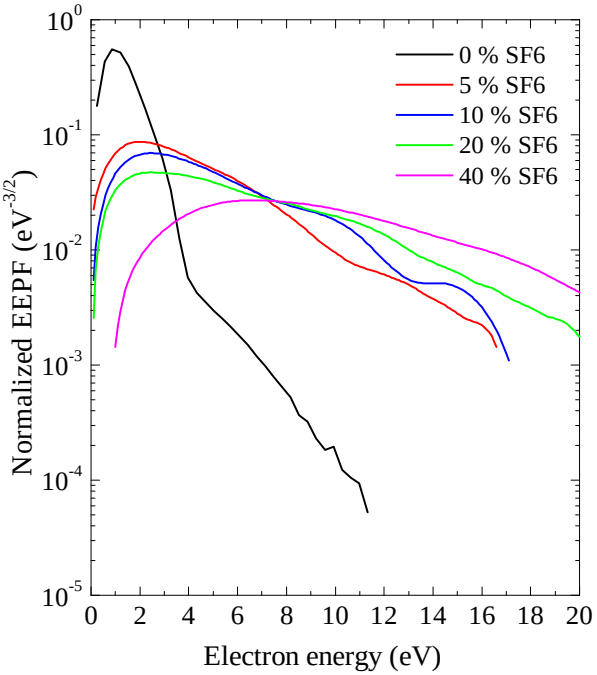

Figure 3.6: Normalized EEPFs recorded with a Langmuir probe for various mixtures of O_2/SF_6, the power and pressure was 100 W and 100 mTorr respectively.

tion of low energy electrons are consumed by attachment processes upon SF_6 dilution and that this fraction increases with increasing SF_6 content. More high energy electrons are produced and T_{eff} increases with increasing SF_6 content. This marked change in the electron characteristics was not observed

in a similar experiment where the atomic oxygen density also increased by a factor of 5 as SF_6 was added to an O_2 discharge [66]. Therefore, under the conditions explored in this work, it appears that both fluorination affects and enhanced electron impact production of oxygen atoms is responsible for the rapid rise in [O] as shown on figure 3.1.

The atomic oxygen production rate, G_{O}, can be used to quantify this enhanced production of oxygen atoms. This production rate is,

$$G_{\mathrm{O}} = 2n_e k_e^{\mathrm{O_2}}[\mathrm{O_2}] \tag{3.1}$$

where $k_e^{\mathrm{O_2}}$ is electron impact dissociation rate constant of oxygen molecules determined by

$$k_e^{\mathrm{O_2}} = \int_0^{\varepsilon_{max}} f_e(\varepsilon)\sigma_e^{\mathrm{O_2}}(\varepsilon)v_e(\varepsilon) \tag{3.2}$$

where $f_e(\varepsilon)$ is the normalized electron energy distribution function, $\sigma_e^{\mathrm{O_2}}$ is the electron impact dissociation cross-section for O_2 taken from [52] and v_e is the electron velocity. The electron density measured with the hairpin probe was used for Eqn.(3.1), the O_2 number density was calculated the using ideal gas law and the known O_2 partial pressure and temperature measured with a thermocouple. It was assumed that the temperature measured with a thermocouple in contact with the inner aluminum side walls reflects the average gas temperature. The error in the electron density and molecular oxygen density was estimated to be 5% and 2% respectively.

It is possible to determine the translation temperature from the Doppler broadened TALIF spectral profiles. This would offer a better estimation of the neutral gas density compared to the thermocouple method (surface temperature) as it directly measures the temperature of a neutral species in the discharge center where the Langmuir probe measurement are taken. However, in this work it was found that gas temperatures evaluated using

TALIF was not trustworthy. The Doppler broadened half widths after deconvolution of the instrumental width (using TALIF on xenon atoms with a known Doppler width) indicate that the oxygen atom temperature in pure O_2 plasma was 365 K and 1937 K in O_2 plasma containing 5 % SF_6. In the latter case, the temperature of the oxygen atoms does not reflect the overall gas temperature as this is an unrealistic gas temperature for this type of discharge. Clearly hot O atoms are produced and the temperature rise could be a consequence of the significant enhancement of hot electrons when the discharge was diluted with SF_6 as shown on figure 3.6.

Self-quenching of laser excited oxygen atoms can be neglected even at high oxygen atom temperatures in the case of O_2 with 5 % SF_6. The self quenching rate (Q_O) required for the optical branching ratio in Eqn.(2.10) was calculated based on a modified self quenching rate constant, k_q^O. It was assumed that changes in the collisional quenching cross-section with temperatures over 300 K was negligible which is a reasonable assumption based on typical cross-sections [77, 78]. Based on the quenching coefficient k_q^O for 300 K quoted by Dilecce *et al* [79], a new k_q^O corresponding to a particle temperature of 1937 K was evaluated. Q_O was negligible despite the high species temperature, the main reason for a negligible self-quenching rate is because oxygen atoms are a minority species and also because the self-quenching collisional cross-section is roughly an order in magnitude smaller than the quenching cross-section of O(3p ^{3}P) by O_2. The oxygen radical production rates and the O_2 electron impact dissociation rate constant for various mixtures of O_2/SF_6 are shown on figure 3.7.

G_O increases with increasing SF_6 content, this is entirely due to the increase in $k_e^{O_2}$ since both [O_2] and n_e required for Eqn.(3.1) decreased as the SF_6 partial increased. These findings indicate that [O] should increase as the

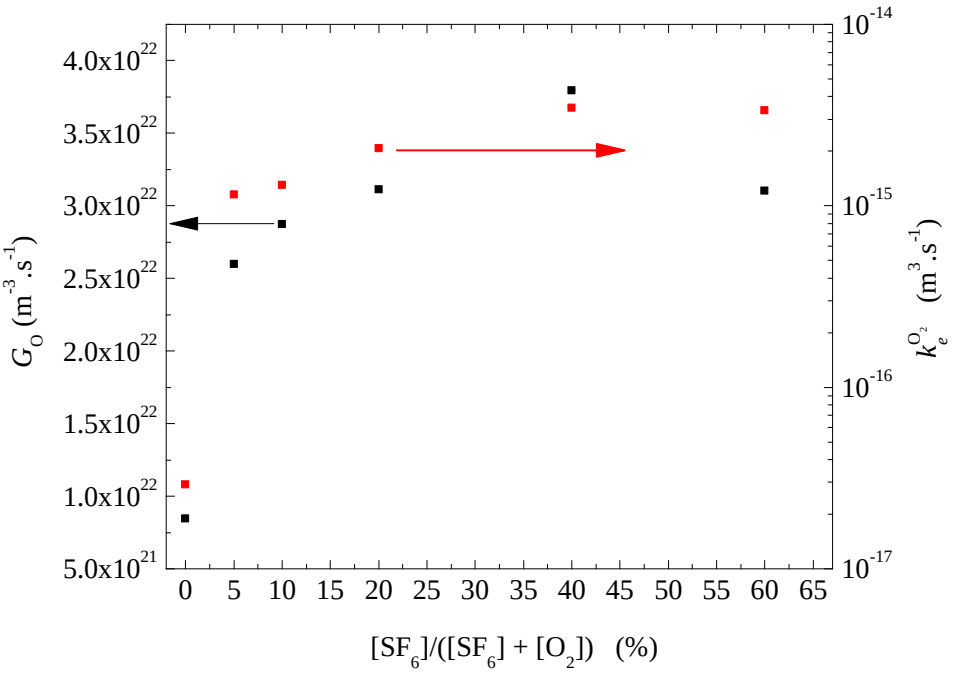

Figure 3.7: Variation of the production rate for atomic oxygen (black squares) and electron impact dissociation rate constant for O_2 (red squares) as a function of SF_6 content, the power and pressure was 100 W and 100 mTorr respectively.

SF_6 partial increase. However, the variation of G_O between 10 - 60 % SF_6 does not agree with the decreasing trend of [O] shown on figure 3.1 over the same conditions. Similar studies also showed a decreasing trend of [O] after a maximum was reached at approximately 10 % SF_6 or CF_4 [63, 65, 66]. These authors concluded that the reduction of O_2 in the input gas was the reason for the decrease of [O] after a maximum was reached at approximately 10 % SF_6 or CF_4. The findings shown on figure 3.7 do not agree with explanations given by these authors. The discrepancy between G_O and [O] in this case is not fully understood at present. However, it is possible that gas-phase reac-

tions between oxygen atoms and the SF_6 plasma constituents are significant and must be considered as an important production/loss channel for oxygen atoms in chemically complex plasmas such as O_2/SF_6.

3.4 Actinometry for detection of [O] in O_2/SF_6 plasma

The applicability of measuring [O] in O_2/SF_6 plasma using actinometry is discussed in this section. Emission lines from O(3p ^{3}P) at 844 nm and Ar($2p_1$) at 750 nm and excitation rate constants evaluated using Langmuir probe EEDFs were used for calculating [O] using the actinometry model described by Eqn.(2.19). Often EEDFs measured with a Langmuir probe can become unreliable in the high energy regime i.e. 15 - 20 eV which is probably due to noise amplification from numerical differentiation. However, it is important that the EEDFs are reliable in this range in order to calculate accurate rate constants as the threshold energies for populating the O(3p ^{3}P) and Ar($2p_1$) levels are within this high energy regime.

For certain conditions explored in this work, the measured EEDFs were unreliable beyond a particular energy ranging from $\approx$ 13 - 17 eV. Therefore, the measured EEDFs were fitted with Maxwellian distributions in the range where a plot of $\ln f_p(\varepsilon)$ vs. ε was linear i.e. for energies lower than the 'unreliable range'. These theoretical distributions were then extrapolated up to 25 eV in order to provide a sufficient energy range for reliable excitation rate constants. It is not unreasonable to assume a Maxwellian distribution beyond the measured range of the EEDFs. No sudden change in the EEDF is expected in this high energy regime (15 - 30 eV) based on good quality measured EEDFs (Langmuir probe and RFEA) found elsewhere [80, 81].

Figure 3.8 shows a comparison the TALIF and actinometry measurements of [O] as function of O_2/SF_6 ratio for a fixed gas pressure of 100 mTorr and power of 100 W. It is clear that actinometry for detection of [O] under the conditions explored in this work is questionable. Quantitatively, the actinometric prediction for [O] is in good agreement with the absolute value [O] for 100 % O_2, however actinometry does not measure the rapid rise of [O] with 5 - 10 % SF_6 addition. Instead, an increase of only $\approx$ 11 % was observed compared to an increase of $\approx$ five fold as shown by the TALIF data. The two techniques for measuring [O] are in good agreement (qualitatively) for mixtures $>$ 10 % SF_6, however, actinometry under predicts the absolute densities in this range. The possible sources of error (actinometry) are violation of the actinometric model, Eqn.(2.19), caused by

- Additional excitation mechanisms for the $Ar(2p_1)$ level which are unaccounted for. Previous works indicate that alternative argon emission lines provide a better reference signal for actinometry [82].

- Resonant enhanced deactivation of the $Ar(2p_1)$ state by oxygen atoms [83]. This would diminish the intensity of the 750 nm emission line to produce erroneous results.

- Addition populating processes for the $O(3p\ ^3P)$ level other than dissociative excitation $e + O_2 \rightarrow e + O + O(3p\ ^3P)$ i.e. population via metastables or cascade excitation.

This chapter reports on the experimental investigation of an O_2/SF_6 CCP plasma using various plasma diagnostic techniques. The dilution of an O_2 plasma with SF_6 resulted in abrupt variations in several important plasma quantities. [O] rapidly increased by a factor of $\approx$ 5 with small additions of SF_6 (5 - 10 %) to the feedstock. The key mechanisms responsible for

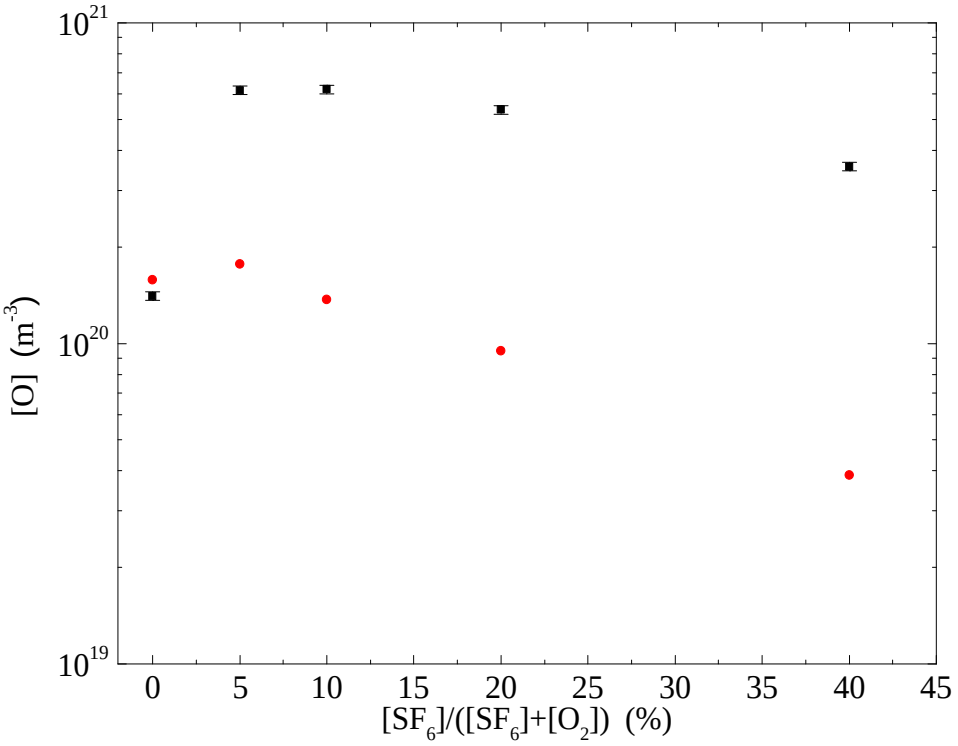

Figure 3.8: Comparison of [O] detected using both actinometry (red circles) and TALIF (black squares). [O] was measured for various ratios of O_2/SF_6, the power and pressure was 100 W and 100 mTorr respectively.

this observation was investigated and found to be an enhanced production of atomic oxygen via electron-impact dissociation of O_2 and also due to fluorination of the reactor walls which decreased the oxygen atom wall loss rate. Such mechanisms were examined using TALIF which demonstrated the effects of changes in the wall conditions on [O] within the discharge and also using a Langmuir probe which was used to quantify changes in electron plasma quantities and the oxygen atom production rate. Quantities such as n_e and T_{eff} also showed dramatic variations due to the addition of SF_6 to O_2 plasma. n_e rapidly decreased by approximately one order of magnitude upon

diluting O_2 plasma with 5 % SF_6 while T_{eff} increased from 0.8 to 3.6 eV when the gas mixture changed from pure O_2 to O_2 with 5% SF_6 and increased as high as 8 eV with increasing SF_6 content. It was found that the detection of [O] using actinometry was poorly correlated to absolute [O] using TALIF. Actinometry did not predict the rapid rise in [O] with SF_6 addition and a significant quantitative discrepancy was observed for mixtures between 5 and 40 % SF_6.

CHAPTER 4

Investigation of electron kinetics in O_2 13.56 MHz capacitive discharge with the use of a Langmuir probe

Knowledge of the electron kinetics is of critical importance for understanding fundamental physical processes within plasma. Parameters such as the electron density, n_e, the electron temperature, T_e, and the electron energy distribution function (EEDF) are particularly useful for understanding important quantities in plasma physics such as reaction rates e.g. dissociation, ionization, excitation, radical production and also fundamental plasma quantities such as the Debye length, electron-ion and electron-neutral mean free paths and the plasma frequency. Electron plasma parameters such as density and temperature and energy distribution depend on plasma operating conditions such as gas composition, pressure, applied power, geometry and reactor material [7, 84]. These operating conditions govern the mechanisms by which electrons acquire energy or are 'heated' for sustaining the

discharge. Therefore a comprehensive understanding of the various electron heating mechanisms and associated electron plasma parameters will allow a better optimization of plasma aided processes e.g. etching for IC manufacturing.

Langmuir probes are by far the most popular technique for investigating the dynamics of charged species within plasma. The electron kinetics and various electron heating mechanism in capacitively-coupled plasma (CCP) have been extensively studied with Langmuir probes [3, 7, 79, 84–87], however these studies have been restricted to noble gases such as argon and helium. Very few experimental reports on the electron kinetics in molecular plasmas commonly used in processing such as O_2 are available. While O_2 inductively-coupled plasmas (ICP) have been the subject of much investigation [88–92], very few studies of O_2 capacitive discharges are available. Lee *et al* [93] reported on the pressure variation (3 - 100 mTorr) of the EEPF, the density of the low and high energy electron groups and the temperature of the low energy electron group in an O_2 CCP. Pulpytle *et al* [94] reported a bi-Maxwellian EEPF in O_2/Ar (75/25 %) CCP operated at 110 mTorr and an applied rf potential of 320 V, the variation of T_{eff} and n_e as a function of applied rf voltage was also reported.

The motivation behind the work presented in this chapter is to provide an extensive experimental investigation of fundamental electron parameters such as n_e, T_{eff} and the EEPF in oxygen capacitively-coupled plasma over a wide range of plasma conditions (power and pressure) with use of a Langmuir probe. These plasma parameters can also be used to investigate various plasma phenomena such as electron heating mechanisms and mode transitions. The densities and temperatures of the low and high energy electron groups are also discussed for the case of a bi-Maxwellian electron energy dis-

tribution. For the first time, the power evolution of the EEPF in O_2 CCP operated at 100 mTorr is reported. A wide power range (10 - 600 W) was explored so that the EEPF was investigated for two discharge modes (α and γ modes). Two distinct trends of n_e versus applied power in oxygen plasma was observed which is contrary to other reports [7, 86]. A hairpin probe was used to measure and compare n_e over the same conditions to better interpret these trends. The α - γ transition in an argon plasma was also investigated for comparison with same mode transition in an oxygen discharge.

The pressure evolution of the EEPF, n_e and T_{eff} in oxygen plasma is also discussed for two powers (30 and 200 W) corresponding to conditions where secondary electrons have significantly different impacts on the plasma. All probe measurements (Langmuir and hairpin) were recorded in the centre of the discharge, the electrode separation distance was fixed at 45 mm, thus, the probe tip was located 22.5 mm from either electrode and in the radial centre of the discharge.

4.1 The α - γ transition in O_2 plasma

Figure 4.1 shows the power evolution of the EEPF measured with a Langmuir probe in an oxygen plasma operated at 100 mTorr. Significant changes in the shape of the EEPF can be seen as the power increased from 10 to 75 W. The number of bulk electrons (0 - 4 eV) rapidly increased with increasing power within this range. Also, the width of the EEPF became progressively narrower as the applied power increased which means a decrease in the effective electron temperature.

The EEPFs are concave in shape and closely resembles a Druyvesteyn distribution for low powers (10 - 30 W). The broadening of the EEPFs in the

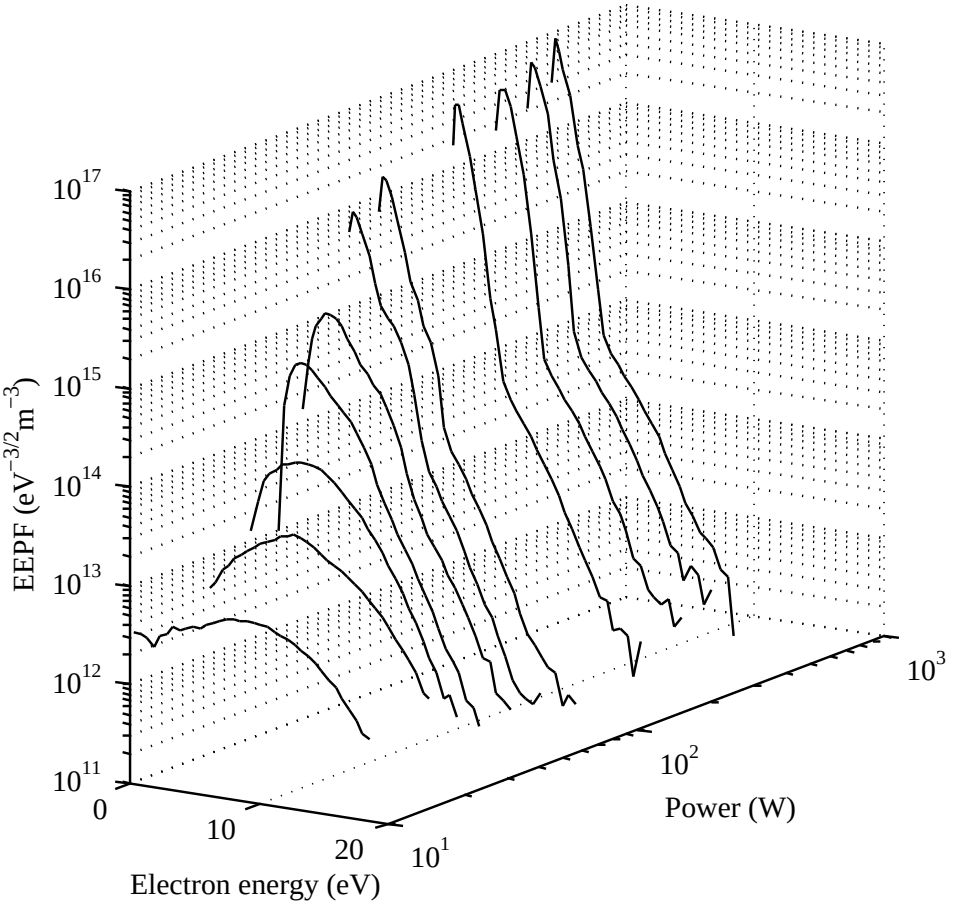

Figure 4.1: Power evolution (10 - 600 W) of the EEPF in pure O_2 plasma operated at 100 mTorr. The significant change in the EEPF is due to the α - γ mode transition.

low power range is typical for discharges sustained by ohmic or collisional heating. Examples of this broadening of the EEPF was also observed in capacitive discharges (Ar, N_2) under conditions which are favorable for ohmic heating i.e. moderate pressures (0.1 - 1 Torr) and low applied rf potential or alternatively low discharge current density [3, 7, 54, 85, 95, 96]. The shape of the EEPFs in the power range of 40 - 75 W resembles a bi-Maxwellian distribution and evolves into a distinctly bi-Maxwellian distribution upon increasing the applied power greater than 75 W. No significant change in the shape occurred for powers between 100 - 600 W.

The significant reshaping of the EEPF between 10 - 75 W indicates the occurrence of the α - γ transition. This occurs when a significant fraction of the applied power or voltage is coupled into the driven sheath. This power is predominantly transferred into the ions which are accelerated by the large electric field across the sheath and release secondary electrons (SE) upon transfer of kinetic energy onto the surface of the driven electrode. These SE are then accelerated by the oscillating sheath leading to significant ionization at the plasma-sheath boundary. Ions produced by SE are again accelerated into the electrode which produce more SE so that an electron avalanche effect develops and consequently n_e increases abruptly. This is most significant at moderate to high pressures, i.e. 0.1 - 1 Torr, where the electron-atom/molecule collision rate is sufficiently high to create an electron avalanche. In this regime the secondary electrons dominate the ionization balance and consequently the bulk rf electric field and electron temperature decreases to prevent further ionization. The discharge is said to be in the γ mode when this occurs the ionization occurs predominantly by these secondary electrons.

The power variations of T_{eff} and n_e are shown in figure 4.2; both T_{eff} and n_e show abrupt changes as the power varies in the range of 10 - 75 W which

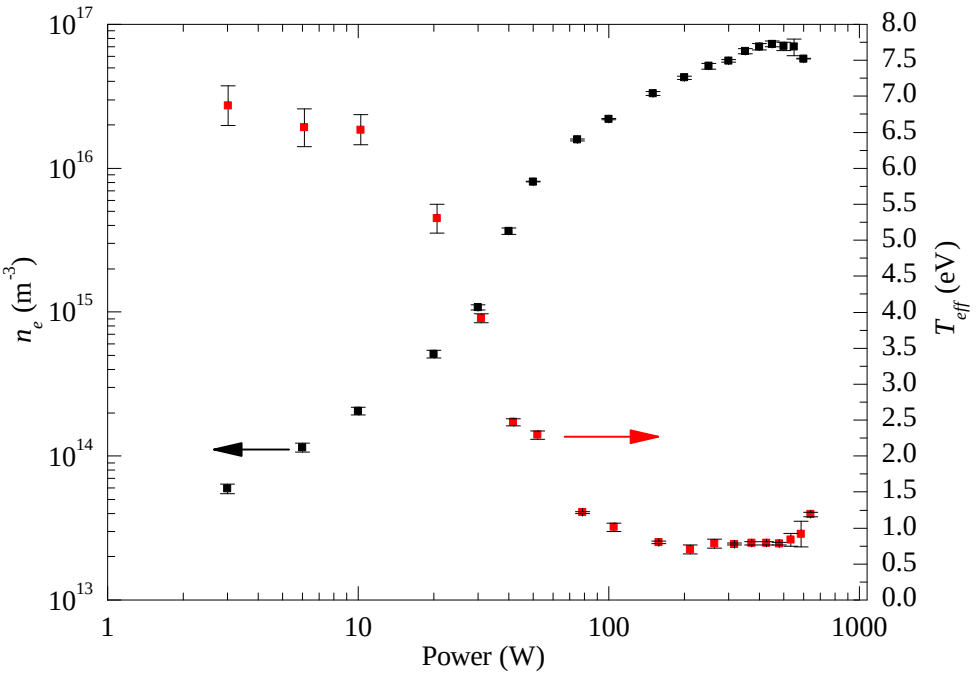

Figure 4.2: Variation of T_{eff} (red square) and n_e (black square) as a function of applied power in O_2 plasma operated at 100 mTorr. The abrupt changes in T_{eff} and n_e with increasing power is due to the α - γ mode transition.

corresponds to the α - γ mode transition.

The behaviour of T_{eff} and n_e with power is consistent with previous finding in argon and helium capacitively-coupled plasma [7, 84, 86] and was also explained by the occurrence of the α - γ transition. The threshold conditions for which the discharge enters the γ is defined by the steepest $T_{eff}(P_{rf})$ dependence [85], where P_{rf} is the applied rf power. At powers less than this threshold the discharge is sustained by a combination of collisional heating and by secondary electrons. The threshold power for the γ mode transition in O_2 plasma operated at 100 mTorr was observed at 50 W. It is estimated that the applied rf voltage (amplitude) in this work at 50 W

(corresponding to the γ mode) is in the range of 200 - 300 V. This is based on typical threshold rf voltages for similar experiments reported in the literature [8, 85, 86, 94].

Similar changes in the EEPF for the α - γ transition as measured with Langmuir probe in argon and helium capacitive discharges have been reported elsewhere [7, 84, 86], although, the electron energy distribution can be specific to the gas used for a given discharge mode. For example, the α mode in Ar plasma is characterized by a Druyvesteyn EEPF while a Maxwellian EEPF was observed in a He plasma for the same mode [7]. Similarly, a Maxwellian EEPF was measured in Ar plasma in the γ mode whereas a bi-Maxwellian was reported in the γ mode of He plasma [7]. No EEPF variation over the α - γ mode transition in O_2 plasma was found in the literature for comparison. Although in two cases, the α - γ transition was observed in oxygen by means of a decrease in the electron temperature with increasing applied voltage [8, 94].

4.1.1 Investigation of the low and high energy electron groups in O_2 plasma at 100 mTorr.

Using the measured EEPF allows for the analysis of the low and high energy electron groups provided the EEPF can be well approximated by a bi-Maxwellian distribution. The densities (n_{low}, n_{high}) and temperatures (T_{low}, T_{high}) of the low and high energy electron groups have been determined for powers between 100 - 600 W since the criteria for a bi-Maxwellian EEPF is valid over this power range. n_{low} and n_{high} were determined by integrating the EEDF within a given energy range that is defined by the approximate electron energy where the EEDF experiences a change in the slope or a 'kink'. In this work; this energy was $\approx$ 3 eV in O_2 plasma at 100 mTorr operated

between 100 - 600 W. T_{low} and T_{high} were determined by a plot of $\ln f_p(\varepsilon)$ versus ε; the temperature of an electron group was found by -1/slope where the slope was found by a linear fit to the data ($\ln f_p(\varepsilon)$ vs. ε) in a given energy range where a linear dependence was satisfied. Figure 4.3 shows the power variation of n_{low} and n_{high} for a fixed pressure of 100 mTorr in O_2 plasma. The low energy electron population increased linearly between 100 - 350 W followed by saturation and a decrease for powers above 350 W. This variation of n_{low} versus power for (100 - 350 W) is expected since an increasing number of secondary electrons are created which generates more electrons from ionizing the background gas, these electrons then fall into the low energy group.

Figure 4.3 shows an unusual trend as n_{low} saturated for powers above 350 W. This is possibly a result of severe contamination of the Langmuir probe tip by sputtered electrode material. Although the tip is automatically cleaned before each IV trace it is still possible that contamination can still occur if the deposition of sputtered electrode material is considerable. This saturation affect will be discussed in more detail in section 4.1.2. Both n_{high} and n_{low} increased with increasing power with no saturation of n_{high} observed at high powers. The densities of the low and high electron groups increased by similar magnitudes i.e. a factor of ≈ 3.6 between 10 to 450 W and a factor ≈ 4.8 between 10 - 600 W.

Figure 4.4 shows the variation of T_{low} and T_{high} as function of increasing power for a fixed pressure of 100 mTorr O_2. The temperature of the high energy group increased gradually with increasing power. These electrons gain kinetic energy from the oscillating sheath as the sheath potential increases with increasing power, hence, T_{high} increases with increasing power. However,

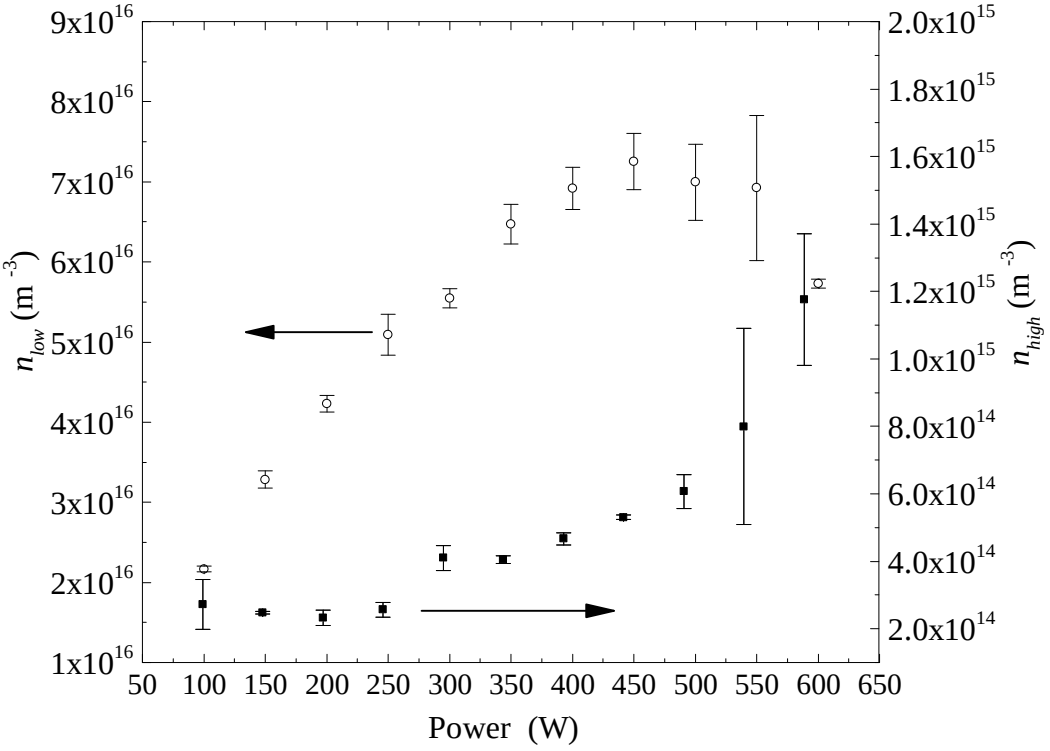

Figure 4.3: Variation of n_{low} (hollow circles) and n_{high} (filled squares) as a function of applied power in pure O_2 plasma operated at 100 mTorr.

T_{low} decreased with increasing power which is expected since the temperature of the bulk electrons predominately determines T_{eff} which was observed to decrease with increasing power due to the $\alpha - \gamma$ transition as discussed in section 4.1.

4.1.2 Comparison of n_e determined with a Langmuir and Hairpin in O_2 plasma.

The power variation of n_e in an oxygen plasma at 100 mTorr measured with a Langmuir probe using the Druyvesteyn method was shown on figure 4.2 in

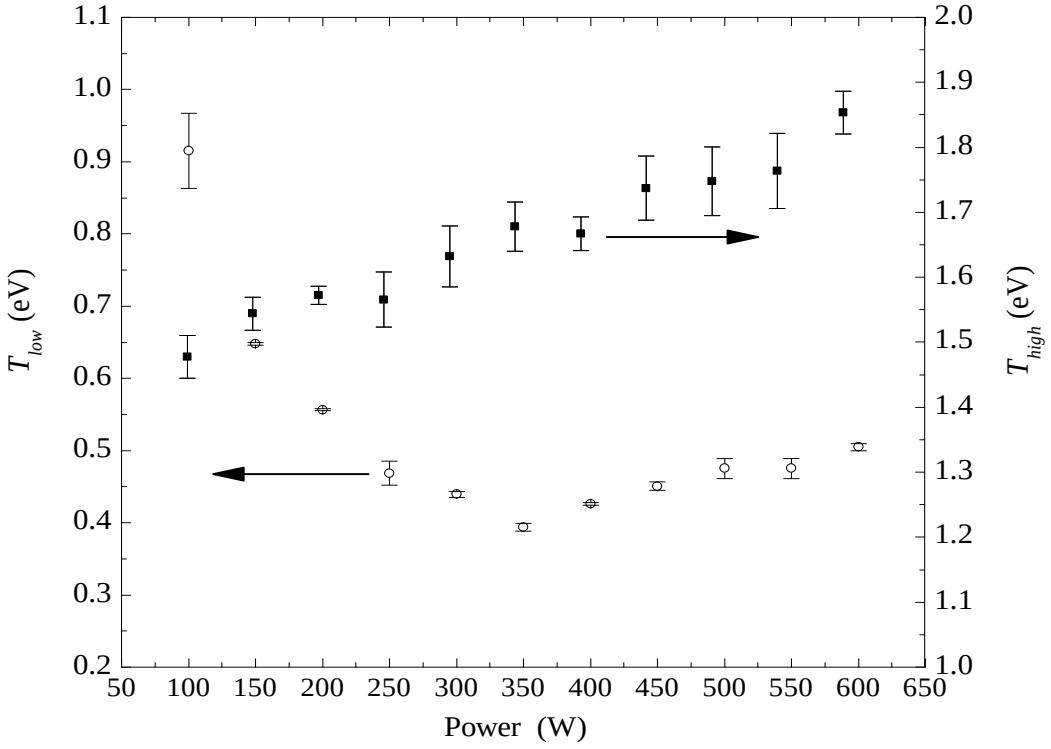

Figure 4.4: Variation of T_{low} (hollow circles) and T_{high} (filled squares) as a function of applied power in pure O_2 plasma operated at 100 mTorr.

section 4.1. Two distinct trends in n_e as function of applied power was observed. Firstly, n_e rapidly increased while increasing the power from 10 - 100 W which is due to the development of an electron avalanche as the discharge enters the γ regime. Secondly, a gradual increase in n_e followed by saturation was observed upon increasing the power above 100 W. This behaviour of the electron density is unusual and was not observed by similar studies [7, 86]. Unfortunately, n_e as a function of current density or applied potential was reported in these articles and no powers were given [7, 86]. It is possible that the higher power range explored in this work (100 - 600 W) far exceeds the powers deposited into the plasma in those studies. Therefore, such unusual

behaviour of n_e (saturation) may not have been observed in similar studies due to dissimilar experimental conditions. A similar saturation affect was observed by Melzer *et al* [84] but no explanation was proposed. Nevertheless, to investigate this unusual n_e trend in further detail requires elimination of any ambiguity of n_e determined with a Langmuir probe. A hairpin probe was used to measure n_e which provides a independent diagnostic in order to investigate this unusual trend 4.2 in further detail.

Discussed in this section is the comparison of electron densities measured with a Langmuir and hairpin probe as a function of applied power in a O_2 plasma operated at 100 mTorr. However, it is necessary to first discuss the possible explanations for the significant difference in the variation of n_e between 100 - 600 W in comparison to the rapid variation within the power range of 10 - 100 W shown on figure 4.2. It is possible that an increasing population of negative ions (O^-) are produced through electron attachment reactions for powers above 100 W which depletes low energy electrons and results in saturation of n_e. Alternatively, a similar plasma process responsible for the consumption of plasma electrons could exist for powers greater than 100 W. Secondly, it is possible that significant probe contamination may occur by sputtered electrode material which can distort the IV characteristics or alter the net dc current drawn by the Langmuir probe by a change in the series resistance. Finally, it is possible that there is a non-linear relationship between the applied power and the actual power deposited into the plasma. Power losses can occur in the matching unit by insufficient impedance matching which may cause non-linearity between the applied power and deposited power.

The comparison of the electron densities determined with the Langmuir and Hairpin probe are shown on figure 4.5. Generally, these techniques pro-

duce results which are in excellent agreement [61]. Reasonable qualitative and quantitative agreement between both techniques is evident as shown on figure 4.5. However, the emphasis is not on the accuracy of each independent technique but on the qualitative agreement and the appearance of saturation of n_e at high powers.

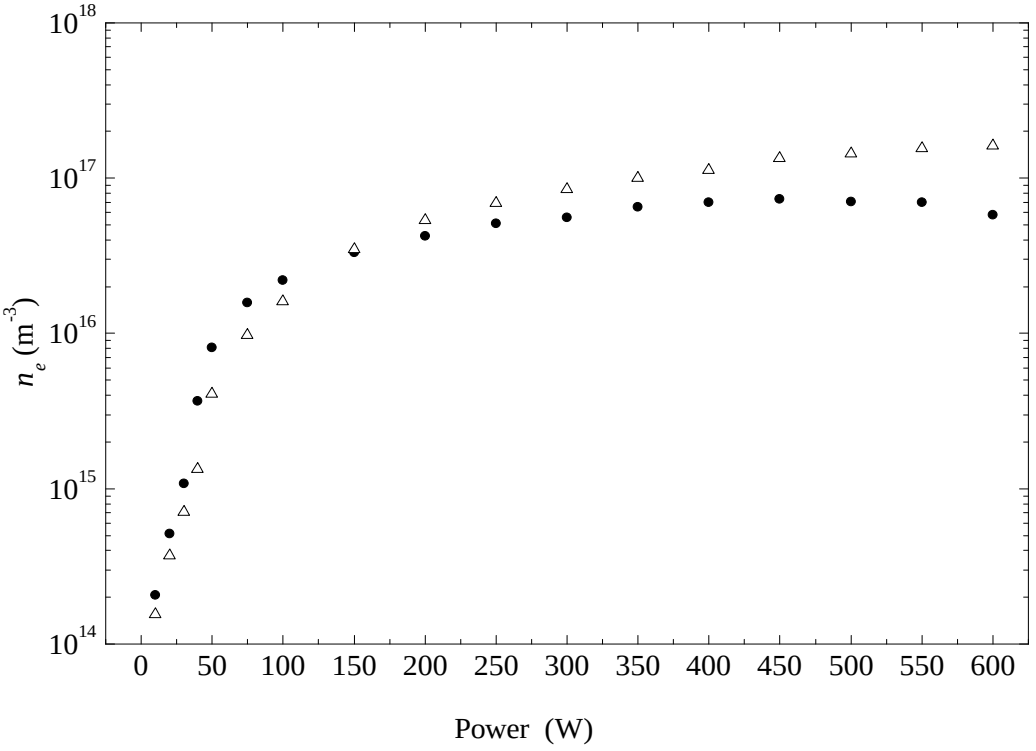

Figure 4.5: Comparison of n_e measured with both a Langmuir probe (•) and hairpin probe (△) as a function of applied power in pure O_2 plasma operated at 100 mTorr.

Saturation of n_e was observed with a hairpin probe which means that this unusual trend is indeed real and erroneous results obtained by an inadequate Langmuir probe in the γ mode (where electrode sputtering can occur) can eliminated. A similar trend was also observed in Ar plasma and will be

discussed in a further section (section 4.2), thus, the loss of electrons at high powers through a plasma-chemical process (attachment) can also be discounted as a possibility. Therefore, it can be concluded that there is a change in the dependence of the applied power with the actual transmitted power. This change in dependence occurs at powers above 100 W and may be due to power losses in the auto match unit.

Figure 4.5 shows reasonable qualitative agreement between n_e determined with an Langmuir and Hairpin probe, this is reasonable statement to some extent (for investigated saturation). However, a discrepancy was observed for powers above 450 W, n_e determined with the Langmuir decreases while the hairpin probe measured a continual increase of n_e for powers above 450 W. Such discrepancy may be due to a considerable contamination of the Langmuir probe tip by sputtered electrode material.

4.2 The α - γ mode transition in argon plasma (comparison to oxygen plasma).

Section 4.1 discussed a significant reshaping of the EEPF and abrupt variations of n_e and T_{eff} as a function of applied power. These findings are typical in CCP when changes in the electron heating mechanisms or mode transitions occur, in particular the α - γ transition. Reported in this section is the α - γ mode transition in Ar plasma operated at 100 mTorr and for powers ranging from 3 to 400 W. Comparisons are made to the same mode transition in O_2 plasma in order to discuss the relevant electron heating processes in each discharge.

The power evolution of the EEPF in Ar plasma operated at 100 mTorr is shown on figure 4.6. The shape of the EEPF varied significantly as the

power increased from 3 - 20 W. The EEPF resembles a Druyvesteyn distribution between 3 - 10 W and evolved into a Maxwellian like distribution for powers greater than 20 W. No significant change in shape of the EEPF was observed for powers above 20 W, however the population of the bulk electrons increased significantly as the power increased. This variation of the EEPF is due to the α - γ transition and is consistent with other Langmuir probe studies in Ar CCP [7, 96]. The first apparent difference between the shapes of the EEPFs in Ar plasma with respect to O_2 plasma (figure 4.1) is that in the high power regime (100 - 600 W) the EEPFs are distinctly bi-Maxwellian in O_2 plasma whereas only one main electron group was observed in Ar plasma. Also, the low energy electrons are characterized by a three-fold higher electron temperature in Ar plasma compared to O_2 plasma. A clearer comparison of these EEPFs for various powers is shown on figure 4.7.

The second interesting observation is that the EEPF in Ar plasma (10 W) is approximately Druyvesteyn in shape with a corresponding T_{eff} and n_e of 3.4 eV and 1.28×10^{15} m^{-3} respectively. Whereas, in O_2 plasma (for the same power and pressure) the EEPF shape is significantly broadened and is characterized by a higher T_{eff} and a lower n_e of 6.5 eV and 2.06×10^{14} m^{-3}, respectively. The broadening affect becomes more apparent in Ar plasma for a lower power of 3 W which is also shown on figure 4.7. The differences in the EEPFs and T_{eff} in Ar and O_2 plasma for a given power of 10 W is due to difference in the threshold power conditions for the α - γ transition since the broadening affect is more apparent in an Ar plasma for a lower power of 3 W. The threshold conditions for which the discharge switches from the α into the γ mode is defined by the steepest $T_{eff}(P_{rf})$ dependence [85]. This corresponds to a threshold power of 20 W and 50 W for Ar and O_2

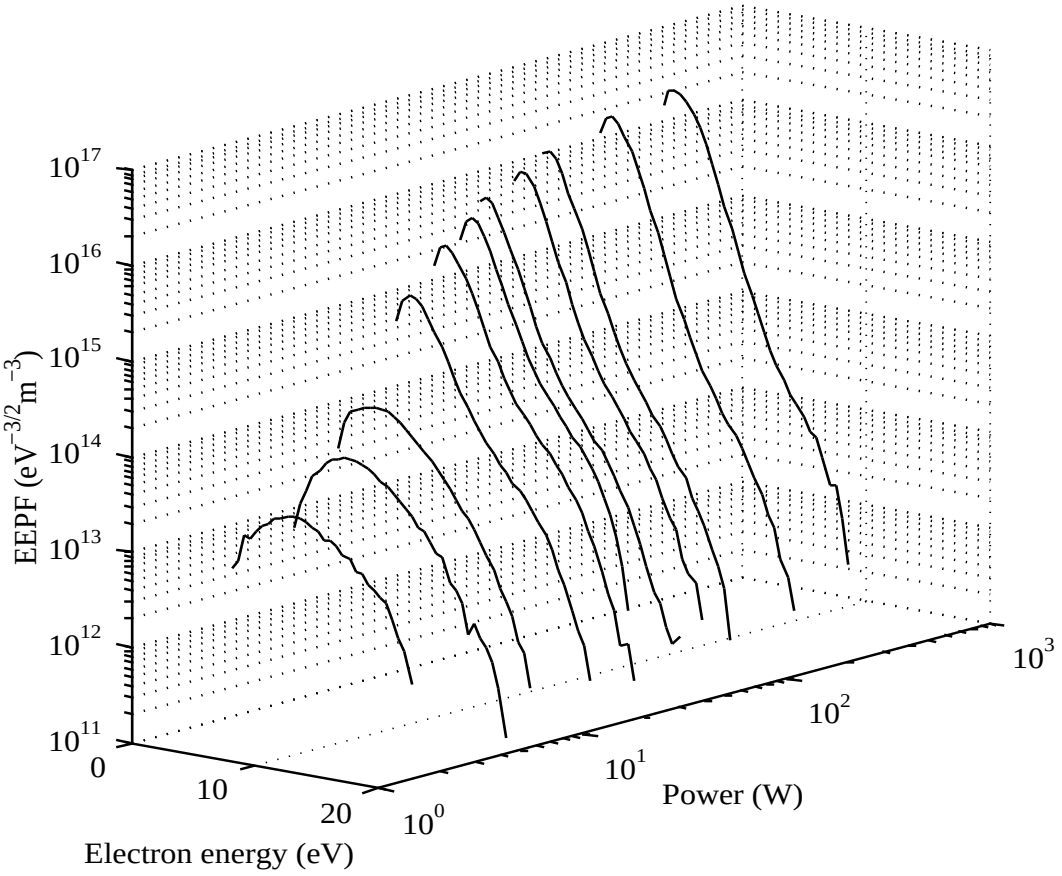

Figure 4.6: Power evolution of EEPF as a function of applied power in pure argon plasma operated at 100 mTorr.

plasma (100 mTorr) respectively. In addition, it is possible that the marked broadening of the EEPF in O_2 plasma (10 W) is enhanced due to the much lower n_e. The rf electric field, E, within the plasma bulk is dependent on n_e i.e. $E \propto J_O/n_e$ where J_O is the discharge current density, therefore the electric field responsible for collisional heating is enhanced in O_2 plasma provided an approximately similar J_O in each discharge for a given power. The flattening of the EEPF was also observed in Ar plasma at 20 W, however,

at much high gas pressure of 500 mTorr which is also shown on figure 4.7.

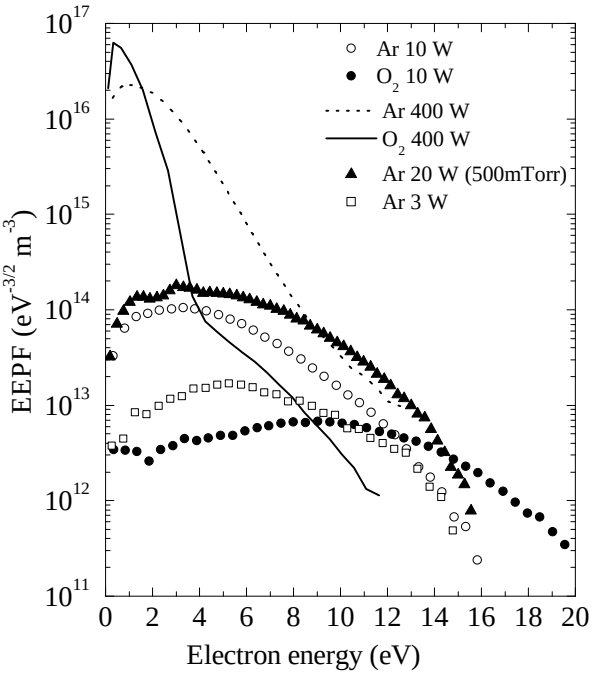

Figure 4.7: Comparison of EEPFs in Ar and O_2 plasma operated at 100 mTorr and for various powers. Significant differences in the EEPFs are shown for given power of 10 W. The broadening of the EEPF was most significant in Ar plasma at 3 W (100 mTorr) and at 20 W (500 mTorr). Collisional heating is more efficient in Ar plasma at high powers (400 W) compared to O_2 plasma.

For this pressure the electron-neutral collision frequency is higher by a factor of five than at 100 mTorr which increases the collisional power transferred to electrons. These affects are discussed in more detail in section 4.2.2.

This EEPF broadening affect and high electron temperatures ($\approx$ 5 eV) is associated with a regime of collisional heating for bulk electrons. It typically

found at moderate pressures i.e. 0.1 - 1 Torr and when the applied power is sufficiently low such that ionization by secondary electron emission is negligible. The physical processes which govern the power transferred to electrons are the rf electric field within the bulk, the rf current density, the dc plasma conductivity, σ_{dc} which is a function of n_e and the average electron-neutral collision collision frequency, $\overline{\nu}_{en}$, and length of the plasma bulk, L_{bulk}, which depends on the electrode separation and sheath width. These processes are discussed in more detail in section 4.2.1.

The EEPFs shown on 4.7 at 400 W are consistent with findings by Lee *et al* [93] in CCP operated at a fixed power of 120 W (12.5 MHz). The authors suggested that collisional heating was inefficient in O_2 plasma due to a weak electric field, hence, the observation of a bi-Maxwellian EEPF instead of a Maxwellian like EEPF measured in Ar plasma. This hypotheses was demonstrated by coupling 2 W of inductive power at 13.56 MHz into the O_2 CCP plasma which heated the low energy electron group, consequently a distinctly bi-Maxwellian EEPF evolved into a Maxwellian EEPF. It is possible that the same physical mechanism is responsible for the formation of a bi-Maxwellian EEPF in O_2 plasma (100 - 600 W) observed in this study. As discussed in section 4.1, the discharge operates in the γ-mode for powers above 50 W (100 mTorr), it is also known that a reduced rf electric field occurs when the discharge operated in the γ-mode [8, 85]. Hence, the expected reduction in the rf electric field for high powers agrees well with the conclusions drawn by Lee *et al* [93] for the formation of a bi-Maxwellian EEPF in O_2 plasma. For these conditions the EEPF in Ar plasma indicates that collisional heating is more effective than in O_2 plasma despite the Ramsauer effect which is known to enhance the existence of two electron groups in Ar plasma [7]. This Ramsauer effect is discussed in more detail in section 4.2.2.

4.2.1 Comparison of T_{eff} and n_e in O_2 and Ar CCP

The comparison of the power variation of n_e and T_{eff} in O_2 and Ar plasma operated at 100 mTorr is shown on figures 4.8 and 4.9 respectively. The variation of n_e as a function of power is similar in both discharges. A rapid increase in n_e occurs for powers 3 - 100 W which is followed by a gradual increase for powers greater than 100 W. The reasons for the gradual variation of n_e at higher powers was already discussed in section 4.1. However, in O_2 plasma n_e is lower than in Ar plasma particularly for powers between 10 - 30 W where the difference can be up to 6 - 8 fold. This could be attributed to the generation of negative ions by attachment reactions in O_2 plasma which will lower n_e.

The measured T_{eff} in O_2 plasma is greater than in Ar plasma when the discharge is operated in the α mode. This is attributed to a higher collisional heating by the rf electric field due to the much lower n_e in O_2 plasma in the power range of 3 - 50 W since $E \propto J_O/n_e$. However at higher powers collisional heating appears to more significant in Ar plasma which results in a higher T_{eff}. This is consistent with finding by Lee *et al* [93].

4.2.2 Power transfer to electrons in O_2 and Ar plasma at 10 and 400 W.

Collisional heating is dependent on momentum transfer collisions which randomizes the direction of the electrons momentum and allows kinetic energy to be gained from the rf electric fields within the plasma bulk. The physical mechanisms responsible for power transfer to electrons (collisionally) is investigated to better interpret the Langmuir probe measurements of n_e, T_{eff} and the EEPF in O_2 and Ar plasma operated at 100 mTorr and 10 and 400

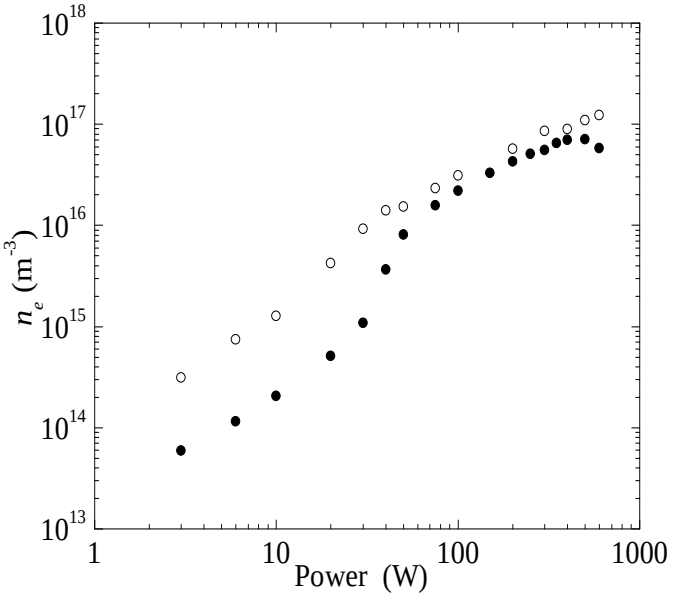

Figure 4.8: Comparison of n_e measured in argon (○) and oxygen (●) plasma as function of applied power, the gas pressure was 100 mTorr.

W. The time averaged power, $\overline{P}_{ohm}$, per unit area transferred to electrons by collisional heating is given by [3]

$$\overline{P}_{ohm} = \frac{1}{2} J_O^2 \frac{L_{bulk} m_e \overline{\nu}_{en}}{e^2 n_e} \tag{4.1}$$

where J_O is the discharge current density, L_{bulk} is the length of the bulk of the discharge and $\overline{\nu}_{en}$ is the average electron-neutral collision frequency. The ohmic power transferred to electrons can also be written in terms of the rf electric field, E, instead of J_O [3], thus $\overline{P}_{ohm}$ is also proportional to E. Therefore, the kinetic energy gained by electrons by collisional heating is proportional to L_{bulk}, $\overline{\nu}_{en}$ and $1/n_e$ for a given J_O or E.

The momentum transfer collision cross-section at low electron energies ($\approx$ 0.2 eV) for O_2 is over one order of magnitude higher than for argon atoms. This abnormally low electron-atom collision probability is intrinsic to argon

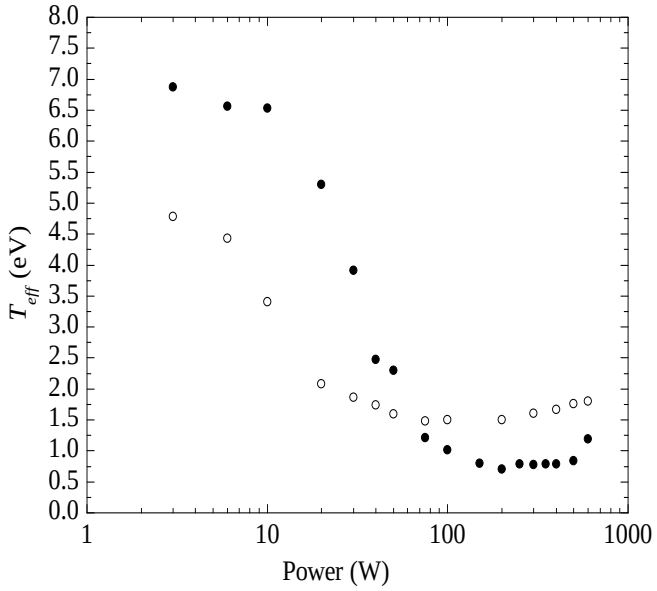

Figure 4.9: Comparison of T_{eff} measured in argon (○) and oxygen (●) plasma as function of applied power, the gas pressure was 100 mTorr.

and other rare gases and is known as the Ramsauer effect. As a consequence, argon has a low electron-atom collision frequency, ν_{en}, compared to oxygen. The electron-atom collision frequency can be calculated by

$$\nu_{en}(\varepsilon) = \sigma_{en}(\varepsilon) v(\varepsilon) n_g \tag{4.2}$$

where σ_{en} is the momentum transfer collision cross-section, $v(\varepsilon)$ is the electron velocity and n_g is the neutral gas density. Figure 4.10 shows ν_{en} for Ar and O_2 for a neutral density corresponding to a gas pressure of 100 mTorr and 300 K.

A clear minimum in ν_{en} was observed for Ar atoms at energies close to the Ramsauer minimum (≈ 0.2 eV). Hence, low energy electrons are inefficiently heated in Ar plasma when compared to O_2 plasma. It is necessary to use the average electron-neutral collision frequency, $\overline{\nu}_{en}$, which takes an energy

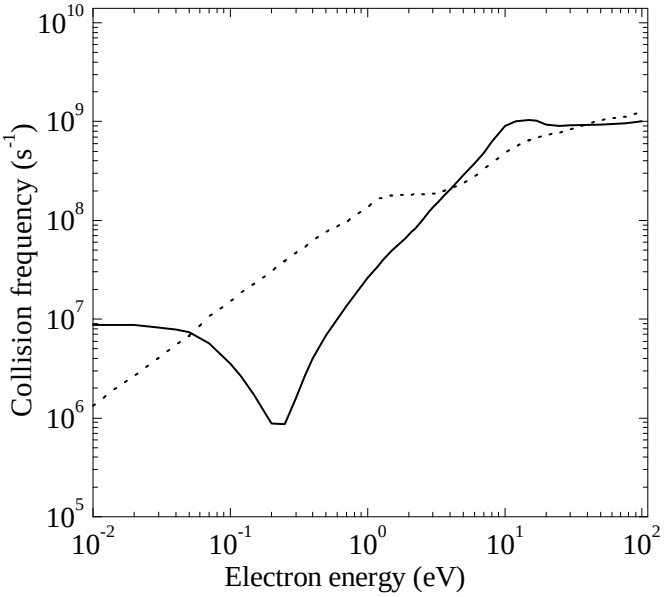

Figure 4.10: Momentum-transfer collision frequency (ν_{en}) for argon atoms ($-$) and oxygen molecules ($\cdots$) for a pressure of 100 mTorr.

distribution of electrons into account when comparing $\overline{\nu}_{en}$ for particular O_2 and Ar plasma conditions. The average electron-neutral collision frequency was calculated over an energy range determined by the dynamic range of the EEDF $\approx$ 0 - 15 eV by

$$\overline{\nu}_{en} = n_g \int_0^\infty f_e(\varepsilon)\sigma_{en}(\varepsilon)v_e(\varepsilon) \tag{4.3}$$

where $f_e(\varepsilon)$ is the normalized EEDF, σ_{en} is the electron-neutral collision cross-section and $v_e(\varepsilon)$ is the electron velocity. The momentum transfer collision cross-sections for argon and oxygen were taken from Vehedi *et al* [97]. It is possible that $\overline{\nu}_{en}$ will be underestimated due to the probes inability to sufficiently resolve the low energy portion of the EEDF due to the limited energy resolution ($\triangle\varepsilon \approx 0.4$ eV) of the probe system. However, it is most likely to affect $\overline{\nu}_{en}$ evaluated for O_2 due to the larger cross-section in the low

energy range.

Table 4.1 shows the calculated $\overline{\nu}_{en}$, n_e and the ratio $\overline{\nu}_{en}/n_e$ for various powers and pressure in O_2 and Ar plasma. For 10 W the ratio $\overline{\nu}_{en}/n_e$ is higher in O_2 plasma by approximately one order of magnitude. This indicates that the power (collisional) transferred to electrons is higher in O_2 plasma compared to Ar plasma which is predominately due to the lower n_e in O_2 plasma as $\overline{\nu}_{en}$ increased by $\approx$ 13 % at 10 W. The ratio $\overline{\nu}_{en}/n_e$ at 400 W in Ar plasma was lower than in O_2 plasma despite the higher T_{eff}. This suggests that an additional heating mechanism is present or that the assumptions of a constant J_O and E are not valid.

This simple analysis shown on Table 4.1 provides only a crude understanding of the mechanisms responsible for the EEPF formation in O_2 and Ar plasma since several assumptions are made that will affect the outcome of such conclusions if invalid. For example, it is possible that the current density or electric field are different in each plasma for a given power and pressure. Furthermore, L_{bulk} is a function of the sheath width, s_o, where s_o is also a function of n_e, T_e and the sheath potential which is unknown. It is clear that these measurements obtained with the Langmuir probe provide a useful insight into various discharge heating processes. However, the exact mechanisms involved require a more detailed investigation.

4.3 Investigation of electron kinetics as a function of gas pressure in O_2 plasma.

Transitions in the dominant electron heating mechanisms are also observed when changes in the gas pressure occur [7, 60, 95, 98, 99]. Collisionless

Table 4.1: Important parameters for ohmic heating

Conditions	$\overline{\nu}_{en}$ (s^{-1})	n_e (m^{-3})	$\overline{\nu}_{en}/n_e$ ($s^{-1}\cdot m^3$)	T_{eff} (eV)
Ar 10 W	3.69×10^{8}	1.29×10^{15}	2.89×10^{-7}	3.4
O_2 10 W	4.23×10^{8}	1.74×10^{14}	2.43×10^{-6}	6.5
Ar 400 W	1.33×10^{8}	8.84×10^{16}	1.51×10^{-9}	1.7
O_2 400 W	1.29×10^{8}	3.69×10^{16}	3.24×10^{-9}	0.8

(stochastic) electron heating is observed at low pressures where the electron-neutral mean free path, λ_{en}, is comparable or greater than the discharge length i.e. $\lambda_{en} > L_{bulk}$. Thus, electrons can reach the oscillating sheaths where kinetic energy is gained to ionize the background gas. Associated with the collisionless electron heating regime is an EEPF which is characterized by two distinct low and high energy electron groups (bi-Maxwellian). However, at high pressures the electron mean free path is small and electrons collide more frequently with the background gas instead of the sheaths i.e. $\lambda_{en} < L_{bulk}$. Thus, the discharge is said to be in the collisional (ohmic) heating regime when this occurs as the electrons gain energy for ionization by interaction with the small rf electric field in the plasma bulk.

When the discharge makes a transition from the collisionless to collisional heating regime, abrupt changes in electron characteristics such as the EEPF, n_e and T_{eff} occur. Transitions in the heating mode (with pressure) can also have a considerable affect on the spatial distributions of the electron heating rate, EEPF, n_e and T_{eff}. These parameters are investigated with use of a Langmuir probe. The pressure evolution of the EEPF, n_e and T_{eff} in O_2 plasma is reported for fixed applied powers of 30 and 200 W corresponding

to regimes where secondary electrons have different significances.

4.3.1 Pressure evolution of the EEPF, n_e and T_{eff} at 30 W.

The pressure evolution of the EEPF and the corresponding n_e and T_{eff} in O_2 CCP operated at 30 W is shown on figures 4.11 and 4.12 respectively.

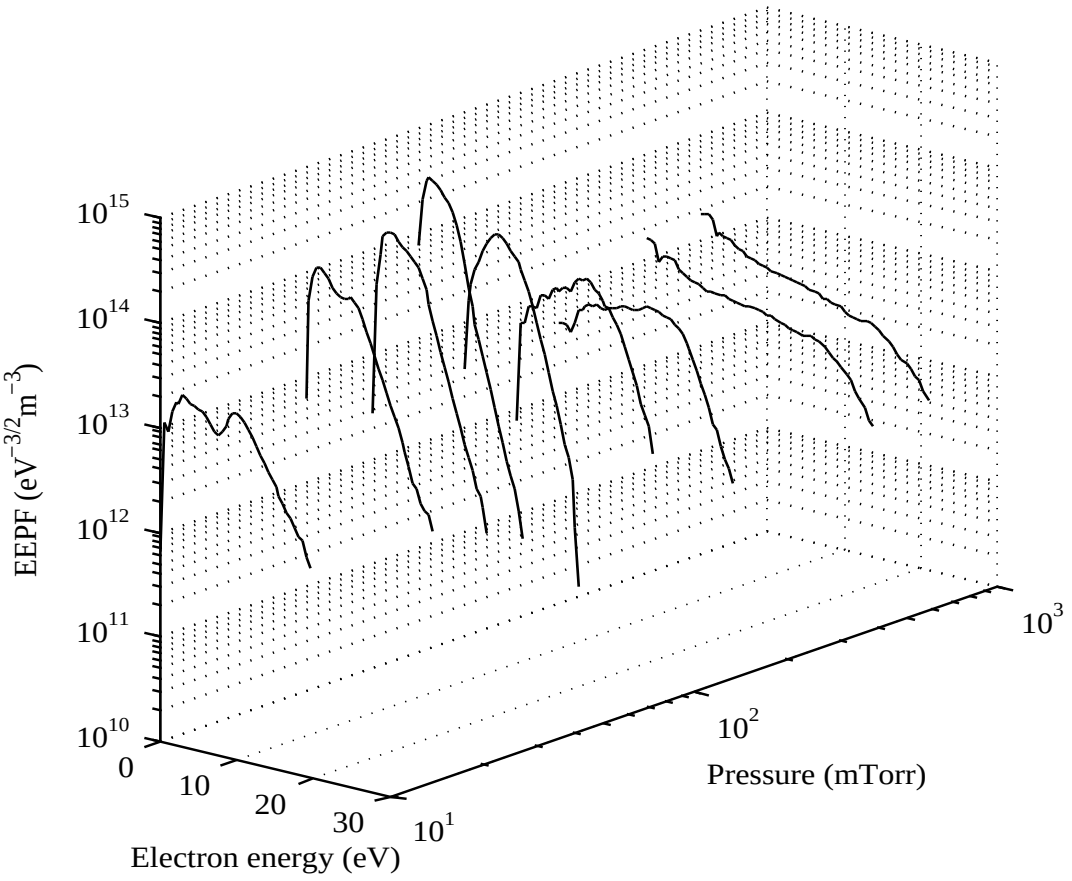

Figure 4.11: Pressure evolution of the EEPF in O_2 plasma operated at 30 W.

The tail of the EEPF in the energy range close to the O_2 ionization

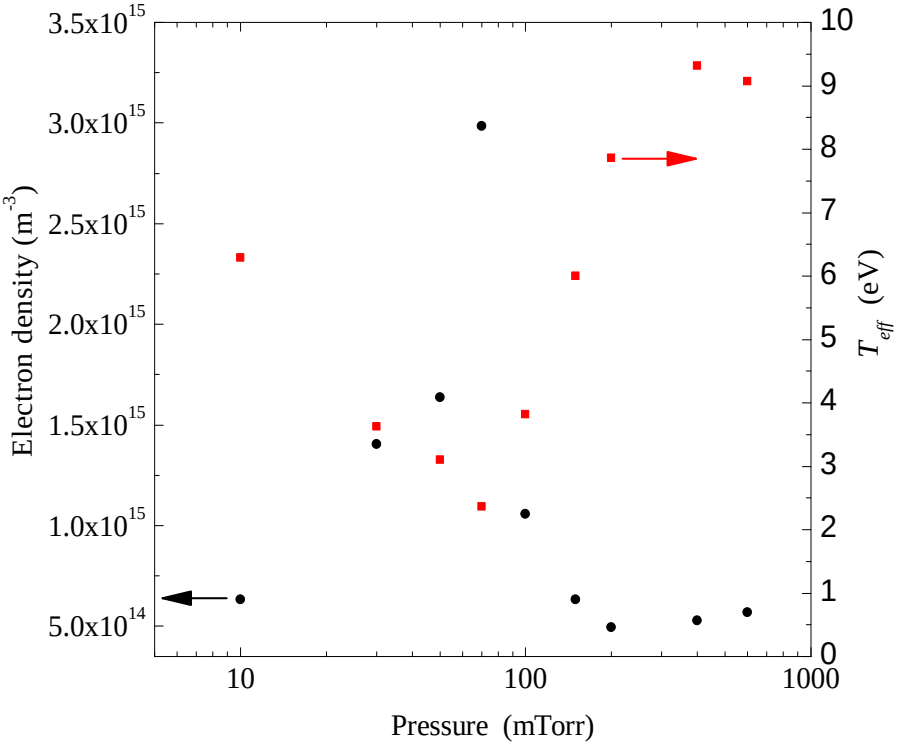

Figure 4.12: Pressure evolution of n_e (black circles) and T_{eff} (red squares) in O_2 plasma operated at 30 W.

potential ($\approx$ 12 eV) decreased significantly with increasing gas pressure (10 - 70 mTorr). This is consistent with the inverse relationship between the ionization rate constant and neutral gas density as derived from the particle balance equation [3],

$$\frac{k_{ion}}{u_B} = \frac{1}{n_g d_{eff}} \tag{4.4}$$

where k_{ion} is the ionization rate constant evaluated using the normalized EEDF, ionization cross-section and electron velocity, u_B is the Bohm velocity, n_g is the neutral gas density and d_{eff} is the effective plasma size which accounts for the edge to centre density ratio in both the radial and axial directions. k_{ion} is sensitive to changes in the EEDF or T_e (for a Maxwellian

distribution) and can vary by several orders of magnitude for changes in T_e in the range of 1 - 5 eV, however, u_B is less sensitive to T_{eff} and has a $T_{eff}^{1/2}$ dependence. Thus, the ionizing tail of the EEPF should decrease with increasing pressure provided negligible changes in d_{eff}.

λ_{en} for the low energy electron group and for low pressures of 10, 30 and 50 mTorr is $\approx$ 207, 70 and 40 mm respectively. These electrons have a mean free path much larger than the plasma half-width (12 - 15 mm), however, they can not reach the oscillating sheath as they are confined in the bulk by the dc ambipolar potential barrier. The corresponding λ_{en} for the high energy electron group for the same pressures is $\approx$ 37, 14 and 8 mm respectively which is comparable to the plasma half-width. These electrons, particularly for 30 and 50 mTorr effectively ionizes neutrals in the bulk to sustain the discharge. These electrons have enough energy to over come the dc ambipolar potential well in the bulk to reach the plasma boundary. Their energy which is lost by inelastic collisions is compensated by energy gained at the sheaths.

Associated with conditions favorable for stochastic heating is a bi-Maxwellian electron energy distribution with a characteristic low bulk electron temperature ($\approx$ 0.5 eV) and a high tail electron temperature ($\approx$ 3 eV). However, an EEPF with such characteristics was not observed at low pressures corresponding to the collisionless regime (10 and 30 mTorr). It is possible that the stochastically heated high energy electrons dissipated most of their energy at the plasma-sheath boundary and therefore such characteristics are not observed in the discharge centre. The EEPFs at 50 and 70 mTorr shown on figure 4.11 exhibit a bi-Maxwellian shape with the low energy group characterized by a higher temperature than the temperature of the high energy electron group. This is due to the increasing importance of ohmic heating as the pressure rises. As discussed in section 4.1 the threshold power for the

transition into the γ mode in O_2 plasma at 100 mTorr was observed at 50 W. Hence, at 30 W and for moderate pressures (50 - 70 mTorr) the discharge is likely to have a ohmic heating component where a characteristic higher electron temperature for the bulk electrons occurs in the discharge centre.

An unusual structure in the EEPF was observed at 10 and 30 mTorr. These distributions had a doubled peak feature and the peaks appeared at energies in the region of 3 and 10 eV respectively for 10 mTorr. The dip appearing between the peaks was located at 7 eV and could be due to the loss of electrons through an inelastic collisional process such as vibration or rotational excitation of O_2 molecules with a particularly large cross-section or a maximum in the cross-section at an energy which corresponds to the location of the dip. Structure or a so called 'dip' or 'hole' of this kind is not usually observed in EEPFs in O_2 plasma. Although, it has often been reported in N_2 plasma with a dip located in the energy range of 2 - 4 eV which correlates to the maximum in the cross-section for vibrational excitation of $N_2(X^1\sum_g^+)$ [95, 98, 100]. The structure observed at 30 mTorr was similar except the peaks and dip appeared at lower energies. An unusual double peaked structure of the EEPF was reported in N_2 ICP [101] using a Langmuir probe. Similarly, the energy location of these peaks were also displacement as a function of operating conditions (power/pressure) [101]. Structure was also observed on the Langmuir probe measured EEPFs in H_2 capacitively-coupled plasma by Mahony *et al* [102].

The EEPF makes an another transformation as the pressure was further increased. The ionizing tail of the EEPF increased as the pressure increased from 70 - 600 mTorr, this behaviour is opposite to observations between 10 - 70 mTorr. The EEPF extended out towards high energies and consequently T_{eff} increased up to a maximum of $\approx$ 9 eV which is particularly high for

low pressure capacitive discharges. A similar increase in T_{eff} with increasing pressure was reported elsewhere for non-Maxwellian EEPFs resulting from collisional heating of low energy electrons [7, 60, 87, 95]. Although, such findings do not necessarily violate the inverse relationship between the ionization rate constant, k_{ion}, and the neutral gas density given by the particle balance equation since the bulk electrons largely determines T_{eff}, and T_{eff} is only proportional to k_{ion} for a Maxwellian EEDF. The findings shown on 4.11 differ from other findings since the number of electrons with energies higher than the ionization potential of O_2 is generated, thus, resulting in a higher k_{ion} with increasing gas pressure which is contrary to the particle balance equation.

The marked enhancement of energetic electrons with increasing pressure is better illustrated by a two dimensional plot of the EEPFs (normalized) shown on figure 4.13. This figure shows the EEPF in O_2 plasma for pressures of 100, 200, 400 and 600 mTorr and for a constant power of 30 W.

T_{eff} for 100, 200 and 400 mTorr was 3.8, 7.8 and 9.3 eV respectively which corresponds to a substantial increase in the ionization rate constant 6.6×10^{-18}, 2.4×10^{-16} and 4.8×10^{-15} $m^3 \cdot s^{-1}$ respectively. A significant reduction in the effective plasma size is required according to Eqn.(4.4) to produce such a large variation in k_{ion}. For example, d_{eff} needs to be a factor of ≈ 53 less at 200 mTorr compared to 100 mTorr to produce such a change in k_{ion}. Furthermore, d_{eff} must be ≈ 1930 less at 400 mTorr compared to d_{eff} at 100 mTorr in order to increase k_{ion} by several orders of magnitude. Such a significant reduction in the plasma size with increasing pressure seems dramatic in order to satisfy 4.4. However, visual observations of the glow with increasing pressure did indicate a change in the confinement of the plasma. At low pressures the glow filled a significant volume of the chamber, how-

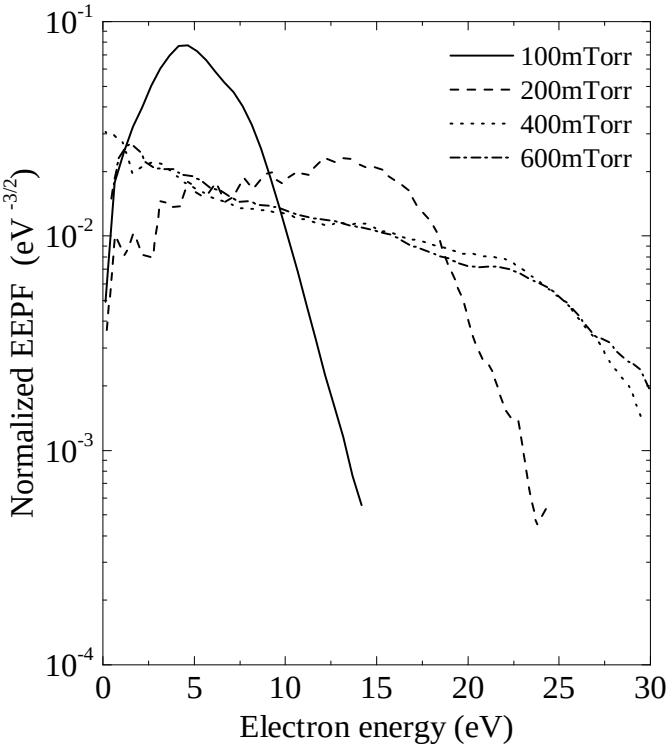

Figure 4.13: Normalized EEPFs for several gas pressures at a constant applied power of 30 W. A significant enhancement of energetic electrons was produced with increasing pressure.

ever, at higher pressures the glow was restricted to small distance ($\approx$ 5 mm) from the driven electrode and a lesser glow at the grounded plasma-sheath region. A similar observation was observed in N_2 plasma for similar conditions; in addition the EEPF showed a similar dependence to that observed in O_2 plasma as shown in figure 4.11. This usual effect was only observed in O_2 and N_2 plasma as the ionization rate constant decreased with increasing pressure over identical conditions in Ar plasma. Table 4.2 summarizes these parameters such as k_{ion} and d_{eff}.

It is possible that other particle loss mechanisms may exist due to

Table 4.2: Parameters for the particle balance law.

Pressure (mTorr)	k_{ion} ($m^3 \cdot s^{-1}$)	T_{eff} (eV)	u_b ($m \cdot s^{-1}$)	d_{eff} (m)
100	6.6×10^{-18}	3.8	3.4×10^{3}	1.7×10^{-1}
200	2.4×10^{-16}	7.9	4.8×10^{3}	3.1×10^{-3}
400	4.8×10^{-15}	9.3	5.3×10^{3}	8.6×10^{-5}

many complex collisional processes in electronegative molecular discharges. In addition, alternative electron heating mechanisms may exist such as super-elastic collisions for a sufficiently high density of electronic metastables states. Previous reports have shown that super-elastic collisions can play an important role in the formation of the EEPF [103, 104]. Furthermore, it is possible that ohmic heating field is particularly high in the bulk. For the higher pressures examined (100 - 600 mTorr) i.e. collisional regime the EEPF is a local function of the electric field, E. As shown on figure 4.12 the electron densities are particularly low for these pressures $\approx 5\times10^{14}$ m^{-3} which increases E since $E \propto n_e^{-1}$. Finally, spatial variation of the power deposited to electrons as a function of pressure may cause an abnormally high T_{eff} measured in the discharge centre. The discharge sustained by both collisional heating of bulk electrons and by energetic secondary electrons at 30 W. Thus, local electron power dissipation at plasma-sheath boundary will affect the overall ionization balance which can lead to an increase in T_{eff} in the centre of the discharge. The $\alpha - \gamma$ transition discussed in section 4.1 is a good example of the how the spatial redistribution of the electron power rate affects parameters such as n_e, T_{eff} and the EEPF in the discharge centre. An example of significant spatial variations in T_e and n_e for various pressure and voltages have

been reported by Lisovskiy [105]. Despite the various possible explanations discussed, the exact mechanisms responsible for the unusual enhancement of energetic electrons (ionizing) is still unclear. A more detailed investigation of this phenomena is clearly required to better interpret these observations.

4.3.2 Pressure evolution of the EEPF, n_e and T_{eff} at 200 W.

The investigation of n_e and T_{eff} and the EEPF as a function of gas pressure in the range of 10 - 600 mTorr is discussed in this section. These parameters are investigated for a fixed applied power of 200 W which corresponds to a power associated with the γ mode as discussed in section 4.1. The pressure variation of the EEPF is shown on figure 4.14 and the corresponding n_e and T_{eff} can be seen on figure 4.15.

The most significant change in these plasma parameters occurs as the discharge evolves from collisionless to collisional i.e. between 10 - 50 mTorr and when the plasma is very collisional i.e. 600 mTorr, $\lambda_{en} \approx 0.6$ mm. The high energy tail of the EEPF significantly decreased as the pressure increased from 10 to 30 mTorr, this resulted in a $\approx$ four-fold decrease in T_{eff}. This reduction in the concentration of high energy (ionizing) electrons as a function of increasing gas pressure is consistent with the expected reduction in the ionization rate constant with increasing neutral gas density (for a fixed effective plasma size) as given by (4.4). This $k_{ion} \propto (n_g d_{eff})^{-1}$ dependence was satisfied over a wider range of pressures (10 - 200 mTorr) when compared to 30 W (10 - 70 mTorr) reported in section 4.3.1.

Figure 4.16 shows a clearer comparison of several normalized EEPFs for pressures of 100, 200, 400 and 600 mTorr.

An additional transformation of the EEPF occurs at higher pressures

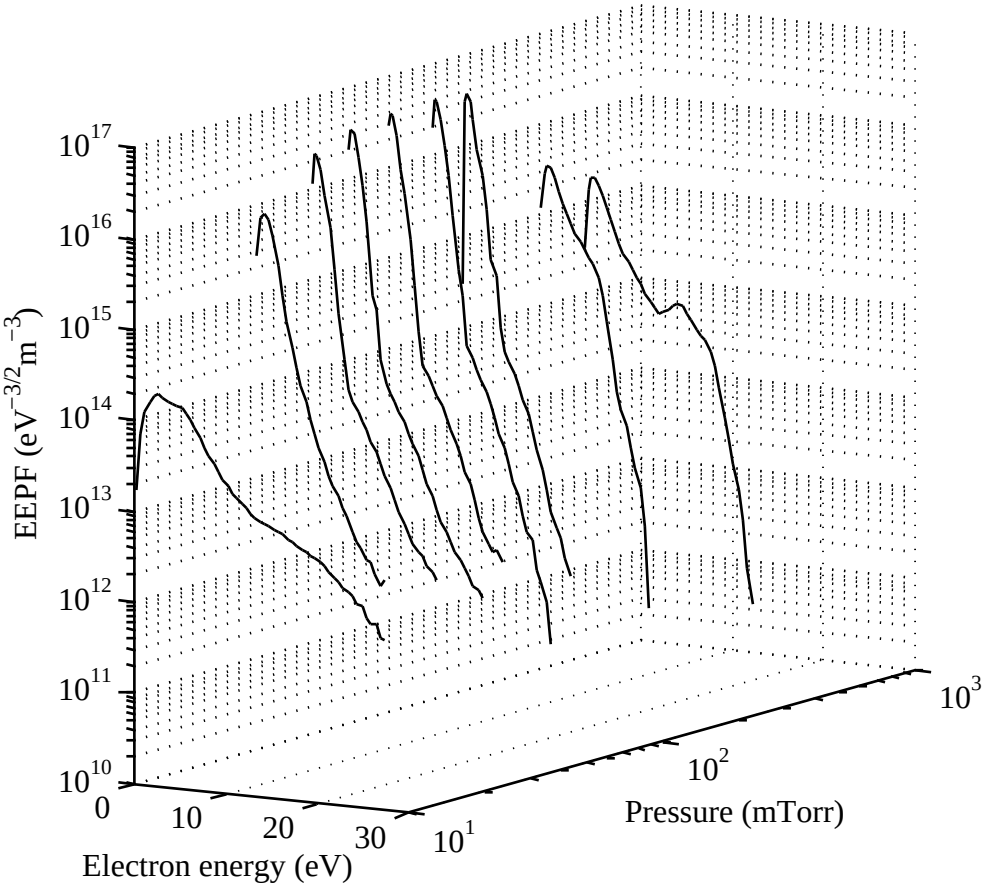

Figure 4.14: Pressure evolution of the EEPF in O_2 plasma operated at 200 W.

which is similar to the findings shown in section 4.3.1 for a given power of 30 W. Collisional heating of low energy electrons becomes important at 400 mTorr as indicated by the EEPF, this broadening of the EEPF (in the elastic region) resulted in an increase in T_{eff} by $\approx$ 1 eV and no significant changes in the high energy tail occurred which is unlike the observations at 30 W. Although, the high energy tail of the EEPF dramatically increased by several orders of magnitude when the pressure was further increased up to 600

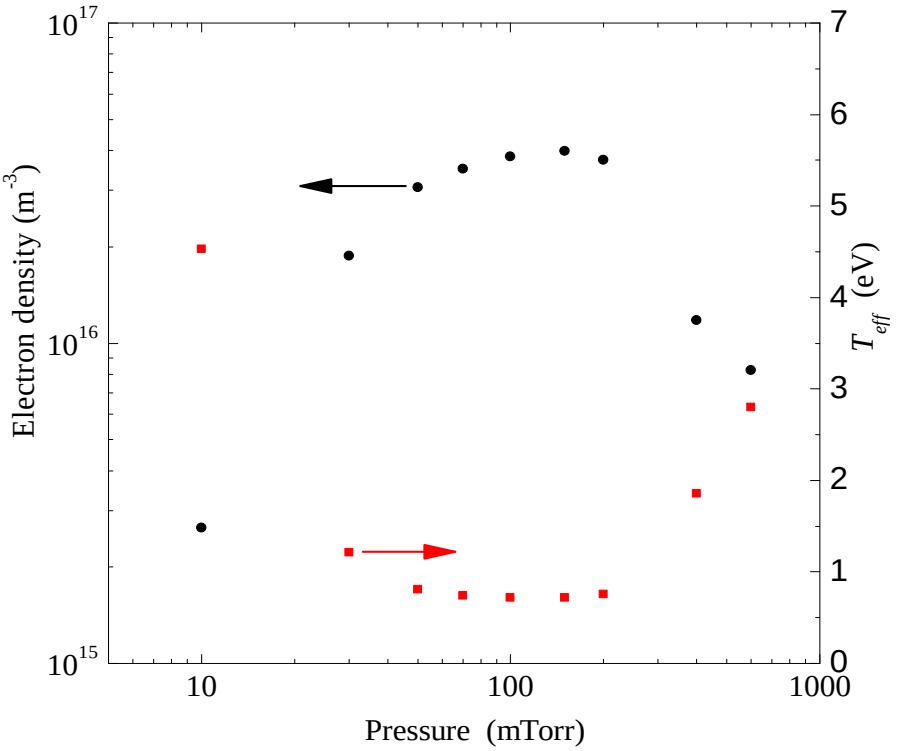

Figure 4.15: Pressure variation of n_e (black circles) and T_{eff} (red squares) in O_2 plasma operated at 200 W. The error bars are too small to indicate.

mTorr.

A similar increase in T_{eff} was observed by Godyak *et al* [7, 54], although, such these findings are a consequence of an EEPF transition in the inelastic region and not the ionizing tail of the EEPF, thus their findings are consistent with the particle balance equation. Abdel-Fattah *et al* [95] also observed the same trend in T_{eff} versus pressure in N_2 CCP, however, the EEPFs were only measured up to 400 mTorr where the tail of the EEPF decreased with increasing pressure. No EEPF was shown for pressures above 400 mTorr which is where this interesting production of energetic electrons is observed in this work. Unfortunately, very few studies of the EEPFs exist for capacitively-

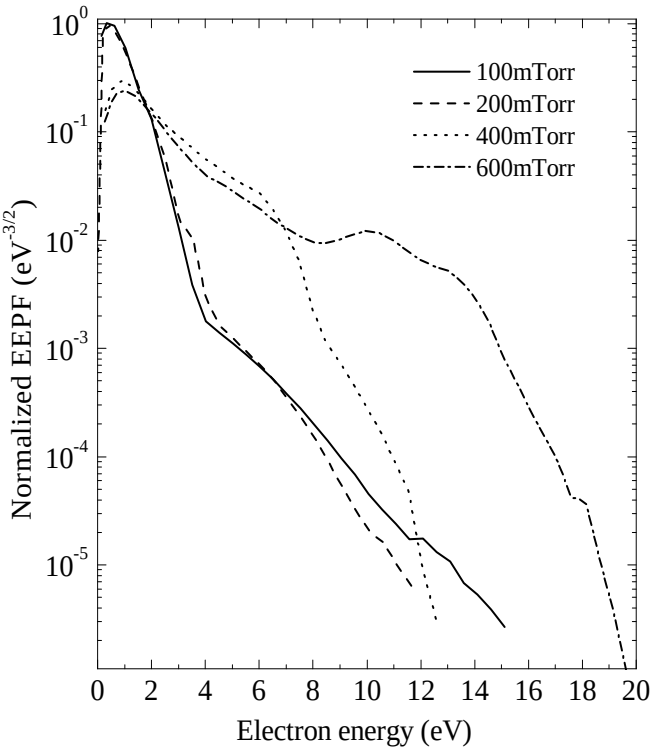

Figure 4.16: Normalized EEPFs for several pressures (100, 200, 400, 600 mTorr), the power was 200 W.

coupled molecular discharges such as O_2 and N_2 for comparison. Lee *et al* [93] reported the pressure evolution of the EEPF but pressures above 100 mTorr were not examined.

Structure was observed on the EEPFs at 400 and 600 mTorr. It is possible that such structure is an effect of super-elastic collisions which is known to produce additional peaks on the electron energy distribution [103, 104]. The low T_{eff} ($\approx$ 0.7 eV) measured in the moderate pressure regime (50 - 200 mTorr) is characteristic of CCP in the γ mode and is consistent with other studies also in the γ mode [7]. The power transferred to the secondary electrons is predominately dissipated in plasma-sheath boundary, thus the

ionization rate is at a maximum there. Consequently, the bulk rf electric field is reduced to prevent further ionization. Secondary electrons cannot penetrate in the centre of the discharge and a minimum in the ionization rate and T_{eff} occurs in the plasma bulk. Such affects was observed experimentally by spatially resolved Langmuir probe measurements by Lisovskiy [105].

This chapter reports on the electron kinetics in an O_2 and Ar capacitively-coupled plasma with the use of a Langmuir and hairpin probe. Various transitions in the electron heating mechanisms were investigated by measuring key electron plasma parameters as a function of external operating conditions such as power and pressure. The $\alpha - \gamma$ mode transition was investigated in both an O_2 and Ar plasma operated at 100 mTorr. Low energy electrons were preferentially heated in the γ mode of an Ar plasma compared to the same mode in O_2 plasma. It was shown that the electron densities were comparable in the γ mode of each discharge, however, n_e was between 6 - 8 times lower in O_2 plasma compared to Ar plasma in the α mode. The collisionless to collisional mode transition was examined in an O_2 plasma by investigating the pressure evolution of the EEPF, n_e and T_{eff}. The measured EEPFs did not agree with the expected dependence with pressure given by the particle balance equation. It was shown that the ionizing tail of the EEPF and thus the ionization rate constant increased with increasing pressure above a given threshold pressure which was power dependent i.e. greater than 70 mTorr at 30 W and greater than 200 mTorr at 200 W. The exact mechanisms responsible for such unexpected observations are unclear at present and require further investigation. Furthermore, structure was observed on the measured EEPFs which can indicate the presence of super-elastic collisions which is known to enhance the ionizing tail of the EEPF.

CHAPTER 5

Investigation of atomic fluorine density in a capacitively-coupled SF_6/Ar and $SF_6/O_2/Ar$ plasma

Atomic fluorine plays a pivotal role in plasma etching due to its ability to remove Si atoms from SiO_2 substrate to produce volatile species such as SiF_2. Atomic fluorine also participates in side wall passivation, so that the concentration of fluorine atoms, as well as other species (Si, O, O_2, SiF_x) governs the overall outcome of the nano-scale etch profile. Thus, the development of reliable diagnostic techniques is pivotal for quantifying such important plasma species in order to investigate the complex chemistry in processing plasmas and further develop plasma processing within industry. Appearance potential mass spectrometry (APMS) is a versatile plasma diagnostic technique that can be used to detect many plasma species. It is particularly useful for detection of atomic fluorine as optical based methods are challenging due to the probe radiation required which is in the $\approx$ 95 nm region for resonant

absorption or $\approx$ 175 nm for TALIF.

This chapter discusses the determination of absolute atomic fluorine density detected using (APMS) in SF_6 based plasma. The power variation of [F] was investigated in $SF_6/O_2/Ar$ plasma operated at 40 mTorr. [F] and the fractional dissociation ($[F]/[SF_6]$) in SF_6/Ar and $SF_6/O_2/Ar$ plasma was also examined with particular focus on the affects of the addition of O_2 to the feedstock. The addition of O_2 to an SF_6 plasma resulted in a marked enhancement in [F] and this effect was further investigated by monitoring the time evolution of the F^+ signal (mass spectrometer) with and without O_2 in the feedstock. Finally, the applicability of detection of relative changes in atomic fluorine density using actinometry was investigated. The power variation of [F] in $SF_6/O_2/Ar$ plasma (40 mTorr) measured with actinometry was examined and compared to APMS. In addition, the time variation evolution of [F] measured with actinometry with and without O_2 in the feedstock was also examined for comparison to a similar experiment using APMS.

5.1 Mass spectrometry (RGA spectra)

Detection of neutral species using mass spectrometry can be achieved using appearance potential mass spectrometry (APMS) or standard residual gas analysis (RGA). The APMS technique uses electrons with selective energies for the ionization of neutral species, whereas RGA uses electrons with a fixed energy of typically 70 eV. APMS is most suitable for detection of atomic radicals under conditions where the radical measured is in the background of the abundant parent molecule, consequently, processes such as dissociative ionization complicates the signal analysis (refer to section 2.4.1 for more details). However, APMS can be used to measure directly ionized radicals only,

therefore, neglecting the dissociative ionization component of the measured signal.

RGA is useful for plasma characterization but interpreting the signals for determining the density of radical species is complicated due to occurrence of several processes which can produce a signal with a given mass to charge ratio (m/e). This section will briefly discuss some of the complications with standard RGA signals and also some useful information (chemistry) which can be obtained from RGA mass spectra. Shown on figures 5.1 and 5.2 are RGA mass spectra of $SF_6/O_2/Ar$ gas (discharge off) and $SF_6/O_2/Ar$ plasma (50 W) respectively, the gas pressure for both spectra was 40 mTorr and the mixture was 85/10/5 % and the electron beam ionization energy was 70 eV. The peaks in these spectra can be generated through several processes, these are direct ionization of atoms and molecules, direct ionization of species fragmented by the electron beam, double ionization, plasma generated species and dissociative ionization of parent molecules.

The peaks at $m/e = 127$, 108, 89, 70 and 51 corresponding to SF_5^+, SF_4^+, SF_3^+, SF_2^+, and SF^+ respectively are generated by fragmentation of SF_6 molecules by the electron beam. These peaks were significant in magnitude when the discharge was off and decreased slightly when the plasma was on. A slight decrease in the intensity of these peaks indicates gas heating. Similarly, peaks at $m/e = 20$, 32, 35 and 54 which correspond to Ar^{++}, O_2^+, SF_2^{++}, Ar^+ and SF_4^{++} respectively also showed a slight decrease when the plasma was on. A signal at $m/e = 146$ from SF_6^+ was not detected as this ion is unstable. A small peak at $m/e = 38$ from F_2^+ was detected without plasma. However, the signal from F_2^+ did increase by a factor of 13 when the plasma was switched on and was probably formed through recombination of fluorine atoms in the plasma. Indeed, the signal at $m/e = 38$ was found to be proportional to the

[F] density.

A particular example of valuable information that can be acquired with RGA is the appearance of peaks at $m/e = 83$, 86, 102 and 105 from SO_2F^+, SOF_2^+, $SO_2F_2^+$, and SOF_3^+ on figure 5.2. These peaks are entirely a result of gas-phase chemistry in the plasma since these signals were not detected when the discharge was off. The appearance of such peaks with the discharge on is particularly useful for identification of plasma produced species and investigating various gas-phase processes. In addition, standard RGA can be useful for investigating plasma-surface interactions. For example, volatile species from silicon etch processes such as SiF_x can be readily detected since such species are only present when the discharge is on and is free from any background signals caused by fragmentation.

A peak at $m/e = 85$ was detected which is likely to be from SiF_3^+; this molecule was probably formed through etching of the quartz clamp plate or optical viewports as no such peak was detected with the plasma off. This is consistent with RGA mass spectra recorded in a waferless CF_4 plasma by Tserepi *et al* [106]. No other peaks from etch byproducts such as SiF, SiF_2 and SiO were detected since there was no major source of silicon present in a waferless discharge. A peak at $m/e = 44$ (SiO^+) was observed but was also present with the plasma off. Therefore, this peak is not from SiO^+ and is probably from CO_2^+. Additional peaks from other various contaminants such as H_2O and N_2 at $m/e = 18$ and 28 were also detected with and without plasma. F^+ and O^+ ($m/e = 16$ and 19) were detected but their signal was dominated by dissociative ionization of their parent molecule since their intensities were significant with the plasma off. It is possible that the signals from SO_2F^+ and $SO_2F_2^+$ with $m/e = 83$ and 102 respectively could also be S_2F^+ and $S_2F_2^+$. These molecules have been detected in SF_6 and SF_6/O_2

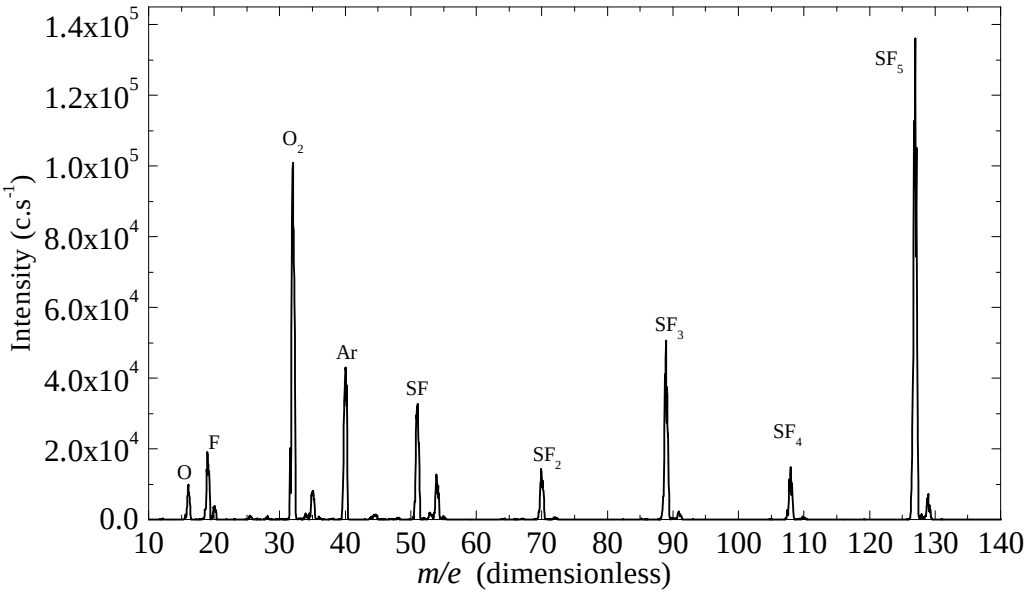

Figure 5.1: Mass spectrum of $SF_6/O_2/Ar$ mixture at 40 mTorr (no discharge).

plasma [107].

5.2 Power variation of absolute fluorine density in $SF_6/O_2/Ar$ plasma.

Discussed in this section is the power variation of absolute atomic fluorine densities measured using APMS. The gas pressure was fixed at 40 mTorr and the feedstock mixture was $SF_6/O_2/Ar$ (85/10/5%), the nominal input power was varied from 50 to 300 W. The discharge ran for $\approx$ 20 minutes to allow the walls to thermally stabilize before each measurement was recorded. The atomic fluorine density increased with increasing power with a slight decrease above 250 W as shown on figure 5.3. The errors bars shown on figure 5.3 were calculated using the standard error on the slope of a linear fit to the F^+

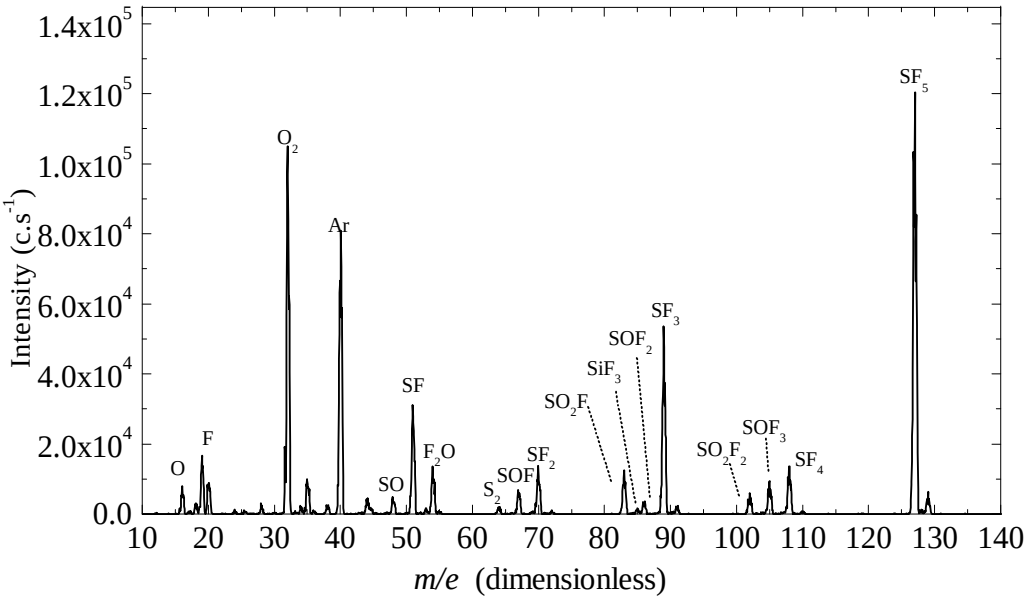

Figure 5.2: Mass spectrum of $SF_6/O_2/Ar$ plasma at 40 mTorr (discharge on).

signal versus electron energy and correspond to the 95 % confidence interval. Another source of error arises from the uncertainty in the measured ionization cross-section for fluorine atoms which is ± 20 % [50] this is not indicated on the figure as it is a source systematic error. Due to the spatial location of the measurement, these results are considered to be a under estimate of the atomic fluorine concentration in the discharge centre. This is due to the expected decrease in the plasma density in the radial direction where the mass spectrometer sampling head is located. This was not confirmed with measurements but a dim glow in this boundary region was clearly apparent with respect to the intense glow in the centre of the discharge.

It should be expected that [F] increases with increasing power [106], this is due to the increase in n_e with increasing power. A [F] $\propto P_{rf}$ dependence would be satisfied provided negligible changes in wall recombination/gas-phase reaction rates and no significant change in the EEDF as function of

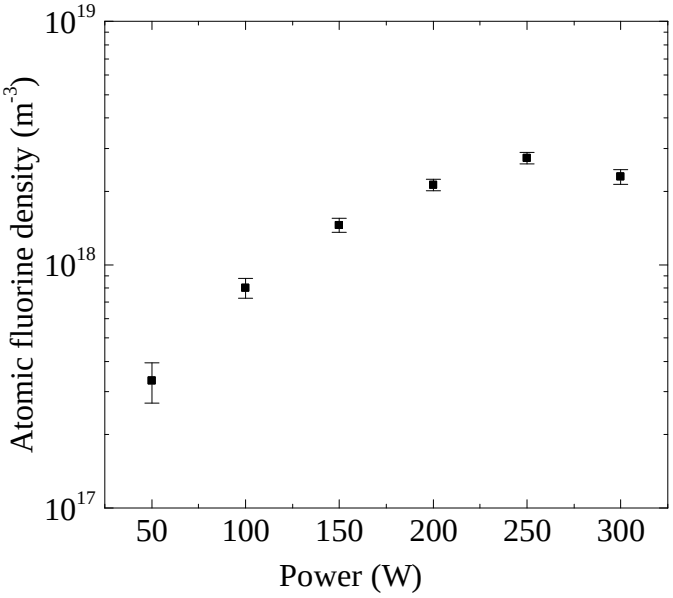

Figure 5.3: The power variation of absolute atomic fluorine density detected using APMS in $SF_6/O_2/Ar$ (85/10/5%) discharge operated at 40 mTorr.

power. The latter is a reasonable assumption between 50 - 300 W based on the results presented in section 4.1, however, a reshaping of the EEDF is expected for powers below 50 W. Thus, increasing the power will increase the electron impact production rate of fluorine atoms. Figure 5.4 shows the measured electron density, n_e, as a function of power for conditions for $SF_6/O_2/Ar$ (85/10/5%) at 40 mTorr. The electron density was measured with a hairpin probe as discussed in 2.6. As expected, n_e increases with increasing power, therefore [F] should also increase with power provided the EEDF and wall loss/gas-phase reaction rates remain approximately constant with RF power. Although, this is not always the case and sometimes the concentration of reactive species can decrease with increasing power if these conditions are not satisfied [108].

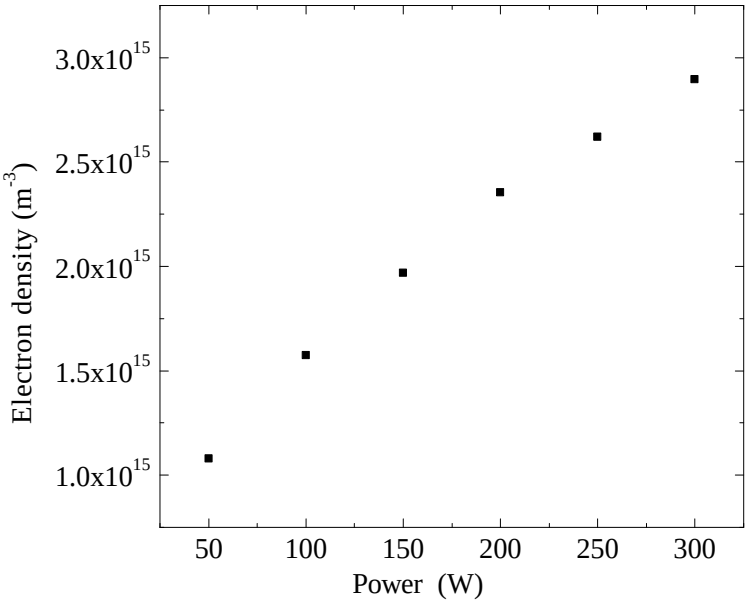

Figure 5.4: The variation of the electron density measured using a hairpin probe in $SF_6/O_2/Ar$ (85/10/5%) discharge operated at 40 mTorr. The error bars are too small to indicate.

5.2.1 Dissociation fractions in $SF_6/O_2/Ar$ and SF_6/Ar plasma

The dissociation fraction, $D = [F]/[SF_6]$, was evaluated using absolute [F] measured by APMS. [F] and D were determined for four plasma conditions to investigate effects of varying the power and feedstock mixture on such parameters, these results are found on table 5.1. D increased by a factor of $\approx$ 2.4 as the power increased from 150 W to 240 W for the SF_6/Ar mixture at 20 mTorr. This is consistent with an increase in the electron impact atomic fluorine production rate with increasing power. Similarly, D also increased with increasing power for the $SF_6/O_2/Ar$ mixture at 40 mTorr. However, the increase of D for this mixture was less compared to the SF_6/Ar mixture.

In this case D increased by a factor of ≈ 1.6 as the power increased over a wider range (150 - 300 W), however, a similar factor was found over the same power range i.e. a factor of ≈ 1.7 between 150 - 240 W.

A possible explanation for the smaller change in D for the $SF_6/O_2/Ar$ mixture is by a decrease in the effective electron temperature as the pressure increased from 20 to 40 mTorr. This would result in lower electron impact dissociation rate constant and consequently a lower production rate of fluorine atoms provided that n_e and the rate of change of n_e with power was similar for both cases. Langmuir probe measurements showed that both n_e and the power variation of n_e was similar for both the $SF_6/O_2/Ar$ mixture (40 mTorr) and the SF_6/Ar mixture (20 mTorr) over the same power range.

A more interesting observation from table 5.1 is the relative difference in

Table 5.1: This table contains atomic fluorine densities and dissociation fractions (D) for different plasma conditions to investigate affects of power and feedstock mixture.

Pressure	Feedstock	RF Power	[F]	[F] error	D
mTorr	(%)	(W)	(m^{-3})	(m^{-3})	(a.u.)
20	SF_6/Ar (95/5)	150	3.4×10^{16}	1.2×10^{16}	5.5×10^{-5}
20	SF_6/Ar (95/5)	240	8.6×10^{16}	1.8×10^{16}	1.3×10^{-5}
40	$SF_6/O_2/Ar$ (85/10/5)	150	1.5×10^{18}	9.7×10^{16}	1.3×10^{-3}
40	$SF_6/O_2/Ar$ (85/10/5)	300	2.3×10^{18}	1.6×10^{17}	2.1×10^{-3}

both [F] and D for each of the feedstock mixtures. A marked increase in [F] and D was observed as the discharge conditions changed from 20 mTorr SF_6/Ar (95/5%) to 40 mTorr $SF_6/O_2/Ar$ (85/10/5%) at a power of 150 W. This resulted in a variation of [F] and D by a factor of ≈ 44 and 24, re-

spectively. This large variation of [F] and D is surprising and uncommon considering the degree of changes in the plasma operating conditions. There are several explanations for these findings: Firstly, the enhancement of [F] and D could occur by a change in the atomic fluorine production rate which depends on both the EEDF, n_e and [SF_6] assuming neutral dissociation is the main production channel for fluorine atoms i.e. $SF_6 + e \rightarrow F + SF_5 + e$. A decrease in T_{eff} would occur for an increase in pressure as already mentioned, however, this drop in T_{eff} was canceled out by the addition of O_2 to the feedstock. This was concluded with Langmuir probe measurements. T_{eff} was 7.3 eV and 6.6 eV at 150 W and 240 W respectively in the SF_6/Ar mixture (20 mTorr) and T_{eff} was 7.8 eV and 6.6 eV for 150 W and 300 W respectively for the SF_6/O_2/Ar mixture (40 mTorr). Previous measurements on this reactor [48] and elsewhere [71, 73] also showed an increase in T_{eff} with the addition of O_2 to the feedstock. Small changes in n_e will have a considerable affect on [F] considering SF_6 dominated plasmas are often characterized by high electron temperatures ($\approx$ 4 - 14 eV) [48, 71, 109]. However, no significant change in n_e was observed based on Langmuir probe measurements in each mixture, therefore changes in [F] and D via electronic dissociation can be ignored.

Secondly, the significant increase in [F] in the SF_6/O_2/Ar mixture could be a result of a change in surface conditions. For example oxygenation of the reactor surfaces would block the chemisorbed sites for fluorine atoms to react with. As a result, the fluorine atom concentration in the plasma increases. It is well known that surface recombination of fluorine atoms can have a significant effect on [O] [63–66] and was also observed on this plasma chamber using TALIF [48]. Therefore the reverse of this process is probable given the reactive nature of oxygen atoms.

A third explanation for these findings is an enhanced production for fluorine atoms by gas-phase reactions. Examples of typical gas-phase reactions for fluorine atom production and their corresponding rates are given on table 5.2. Furthermore, the species involved (reactants and products) in such reactions listed in table 5.2 were readily detected in $SF_6/O_2/Ar$ plasma as shown on figure 5.2.

Table 5.2: This table contains gas-phase reactions for the production of atomic fluorine and their corresponding rate constants taken from [110].

Reaction	Rate constant ($cm^3 \cdot s^{-1}$)
$SF + O \rightarrow SO + F$	1.7×10^{-10}
$SF_2 + O \rightarrow SOF + F$	1.1×10^{-10}
$SOF + O \rightarrow SO_2 + F$	7.9×10^{-11}
$SF_3 + O \rightarrow SOF_2 + F$	2.0×10^{-11}
$SOF_3 + O \rightarrow SO_2F_3 + F$	5.0×10^{-11}
$SF_5 + O \rightarrow SOF_4 + F$	2.0×10^{-11}

5.2.2 Time evolution of the F^+ signal with/without O_2

A significant enhancement of [F] and D was observed as the discharge conditions changed from 20 mTorr SF_6/Ar (95/5%) to 40 mTorr $SF_6/O_2/Ar$ (85/10/5%) as already reported in section 5.2.1. This marked effect of O_2 on [F] and D is further investigated in this section using mass spectrometry. Only relative detection of [F] was necessary for this investigation, no absolute densities were determined. This was achieved by monitoring the time variation of the F^+ signal for a fixed electron energy (21 eV) with and without

O_2 in the feedstock. This signal is proportional to [F] because the electron energy is set below the dissociative ionization potential. The F^+ signal was monitored with time (for a fixed power and pressure) as the O_2 flow was switch on and off allowing relative variations of [F] to be observed while the feedstock mixture changed from pure SF_6 to SF_6/O_2 (90/10%) and back to SF_6. This result is shown on figure 5.5, the gas pressure and nominal input power was fixed at 60 mTorr and 500 W respectively.

A significant increase in the F^+ signal was observed when the O_2 flow was

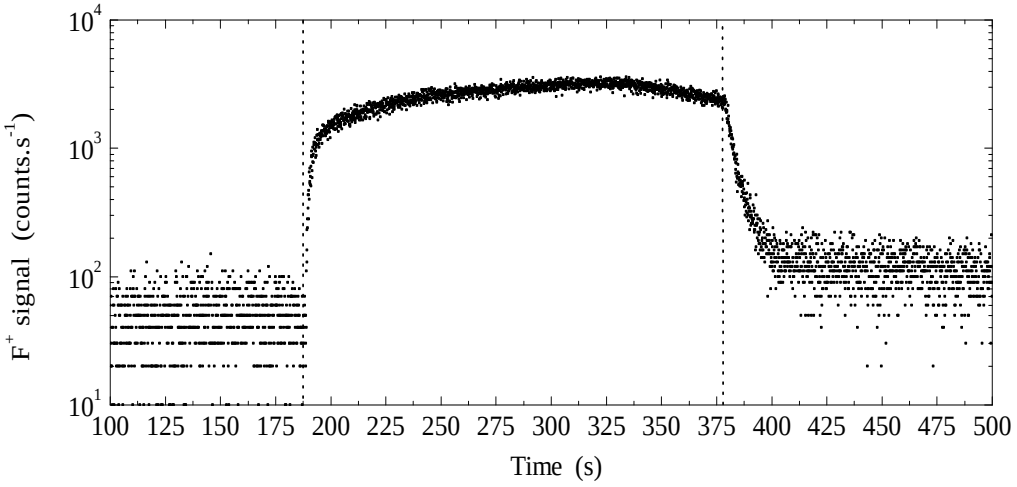

Figure 5.5: Time evolution of the F^+ signal (21 eV) which is proportional [F]. The signal between 100 - 190 seconds and 380 - 500 seconds was measured in pure SF_6 plasma and the signal between 190 - 380 is in an SF_6/O_2 plasma. The power and pressure was kept constant at 500 W and 60 mTorr respectively. The dashed vertical lines indicate the points when the O_2 flow was switched on and off.

turned on at $\approx$ 190 seconds (which is indicated by the first vertical dashed line). The relative difference in the magnitude of the signal upon adding O_2 is a factor of $\approx$ 60. This difference in the F^+ signal is of a similar order to the

difference in [F] shown on table 5.1. The F^+ signal rapidly decreased when the O_2 flow was stopped at ≈ 380 seconds as indicated by the second vertical dashed line. The possible mechanisms responsible for this dramatic effect on the F^+ signal and thus [F] are as discussed in section 5.2.1. To add to these explanations; it is possible that passivating layers such as SiO_xF_y are deposited on the reactor surfaces. Although no silicon wafer was in the discharge, such molecules can still be produced by etching of the quartz clamp plate and optical viewports. The optical emission was also recorded over the same conditions as shown in figure 5.5 in order to investigate relative changes in [F] actinometry, these results are presented in section 5.3.1.

5.3 Fluorine actinometry in $SF_6/O_2/Ar$ plasma.

In this section relative variations of [F] measured with actinometry i.e. I_F/I_{Ar} are compared to [F] measured with APMS. Both data sets are normalized by their maximum value and are shown on figure 5.6. APMS and actinometry both show that the fluorine atom concentration increases with increasing power. However, the actinometry result shows only a two fold increase in [F] while the absolute fluorine density increased by a factor of 10 over the same power range. There are three possible explanations for the discrepancy; firstly, the optical emission from I_F at 703 nm may be generated by alternative means other than direct excitation from ground state. One such process that can lead to the same emission at 703 nm is dissociative excitation from the parent molecule e.g. $e + SF_6 \rightarrow e + SF_5 + F^*$. A cross-sections for a dissociative excitation process involving SF_6 with emission at 703 nm can be found elsewhere [111]. It is not known if other dissociative excitation

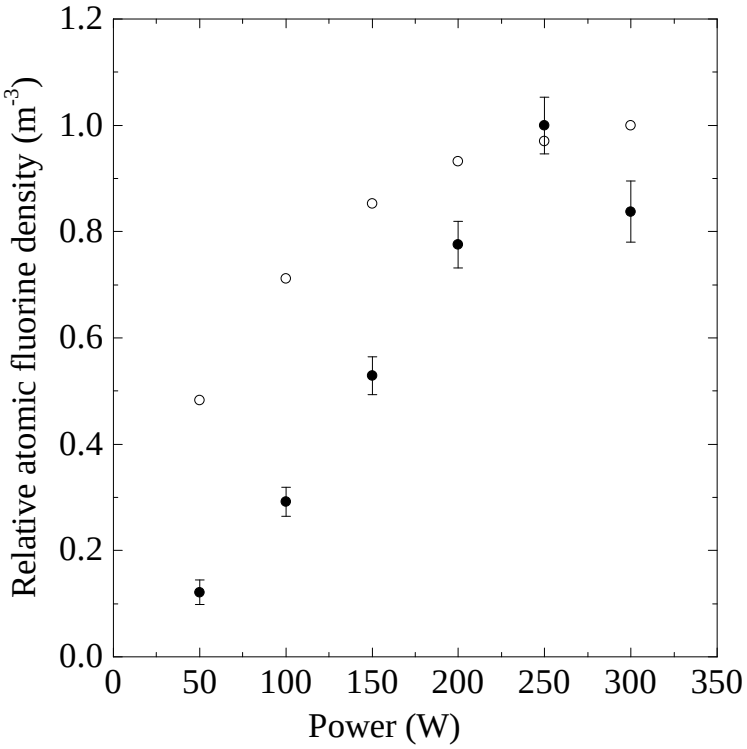

Figure 5.6: A comparison of [F] measured with actinometry (∘) and APMS (•), the gas pressure was 40 mTorr of $SF_6/O_2/Ar$ (85/10/5%). The statistical variation of the OES data was insignificant and the error bars are too small to show.

processes with emission at 703 nm exist with alternative fluorine containing molecules such as F_2, SF and SF_5 etc. If the emission at 703 nm has a significant dissociative excitation contribution using I_F/I_{Ar} to monitor [F] would then be unreliable and correcting for this process would require improving the classic fluorine actinometry model to take dissociative excitation into account. This requires knowledge of the dissociative excitation cross-sections, the EEDF and the dissociative partner involved i.e. SF_6 or F_2.

Secondly, it is possible that dissociative excitation is negligible and K

(where $K{=}k_e^{\mathrm{Ar(2p_1)}}/k_e^{\mathrm{F(3p)}}$) is varying over the explored parameter range violating the assumption of negligible change in the EEDF with power. Without taking this into account, using $I_{\mathrm{F}}/I_{\mathrm{Ar}}$ for monitoring relative changes in the fluorine atom concentration would also be unreliable. The value of K would experience a variation with discharge conditions if a transition in the heating mode occurs. When this transition occurs, the EEDF is reshaped and the ratio $k_e^{\mathrm{Ar(2p_1)}}/k_e^{\mathrm{F(3p)}}$ will change. An example of such a transition in a CCP is the well known α-γ transition [7, 8, 86, 109]. This transition was observed in O_2 and Ar plasma on this plasma system and was discussed in section 4.1. Thirdly, the validity of the argon 750 nm emission line as an actinometer has been questioned by several authors [82, 83, 112, 113]. For example, Chabert *et al* [113] showed diverging trends between I_{Ar} and both the electron density and temperature in SF_6 helicon discharge. This unpredictable behavior of I_{Ar} under certain conditions could also result in dubious [F] measured with actinometry particularly with the argon 750 nm emission line.

The $\mathrm{Ar(2p_1)}$ 750 nm emission line intensity (I_{Ar}) was monitored as function of power in $SF_6/O_2/\mathrm{Ar}$ (85/10/5%) and compared to n_e in order to investigate the relationship between n_e, I_{Ar} and $k_e^{\mathrm{Ar(2p_1)}}$. Assuming that the $\mathrm{Ar(2p_1)}$ level is populated by direct electron impact of ground state only, then the line intensity can be written as $I_{\mathrm{Ar}} = an_e k_e^{\mathrm{Ar(2p_1)}}[\mathrm{Ar}]$, where a is a constant which depends on the optical detection system, transition probability and the photon energy, n_e is the electron density, $k_e^{\mathrm{Ar(2p_1)}}$ is the direct electron impact excitation rate constant and [Ar] is the argon number density. Figure 5.7 indirectly investigates a possible change in parameters such as $k_e^{\mathrm{Ar(2p_1)}}$ by comparing several measured parameters. These are n_e and I_{Ar} (normalized by their maximum value) and also I_{Ar} normalized by n_e. $I_{\mathrm{Ar}} \propto n_e$ provided a and $k_e^{\mathrm{Ar(2p_1)}}$ are constant. However, this is not fully satisfied by their trends

shown on figure 5.7. Both I_{Ar} and n_e show a similar gradual increase with increasing power (although n_e shows a steeper increase). Whereas, I_{Ar}/n_e decreases with increasing power which is indicative of a decrease the excitation rate provided no significant change in [Ar]. It is possible that [Ar] changes due to gas heating since [Ar]$\propto T_g^{-1}$ for a fixed pressure, however, correcting for gas heating effects would further emphasize the discrepancy between I_{Ar} and n_e. This suggests that there is a change in the EEDF, and hence, $k_e^{\mathrm{Ar}(2\mathrm{p}_1)}$ over the conditions explored on figure 5.7 which means that the actinometric ratio, alone, can not be used to reliable monitor relative variations of [F].

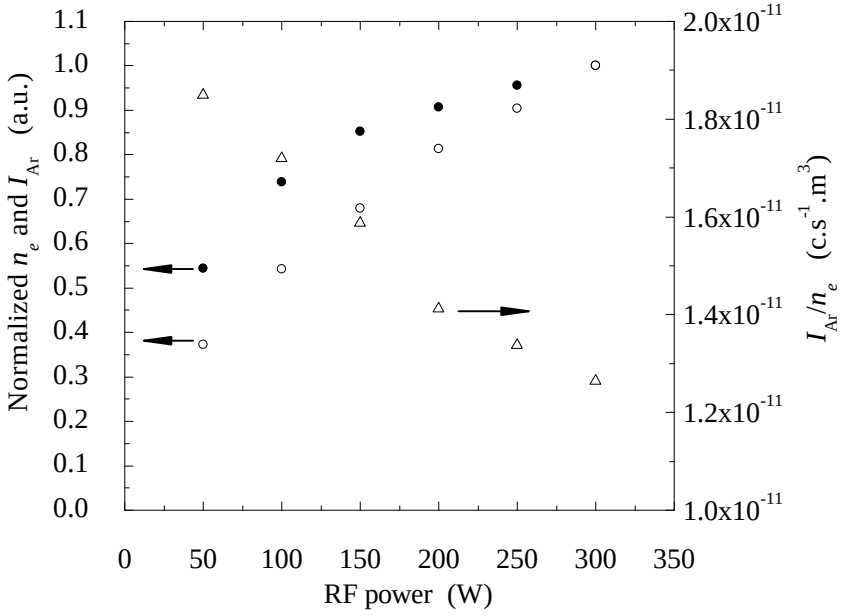

Figure 5.7: A comparison of the power variation of normalized n_e ($\circ$), I_{Ar} ($\bullet$) and the ratio I_{Ar}/n_e ($\triangle$). A decrease of I_{Ar}/n_e with increasing power indicates a decrease in $k_e^{\mathrm{Ar}(2\mathrm{p}_1)}$.

5.3.1 Time evolution of the actinometric signal.

Section 5.2.2 reported on the relative changes in the atomic fluorine density with and without the addition of O_2 in the feedstock, a dramatic enhancement in [F] was observed in a SF_6 plasma containing O_2. The applicability of fluorine actinometry was further examined by also monitoring relative changes in [F] i.e. I_F/I_{Ar} with and without the addition of O_2 in the feedstock. The time evolution of I_F, I_{Ar} and I_F/I_{Ar} was monitored for similar conditions as shown in figure 5.5 i.e. SF_6/Ar (95/5%) plasma between 190 - 380 s and SF_6/O_2/Ar (85/10/5%) plasma between 380 - 500 s and a pressure and power of 60 mTorr and 500 W respectively. I_F/I_{Ar} was scaled by 1×10^4 for comparison with I_{Ar} and I_{Ar}. These results are shown in figure 5.8, I_F/I_F rapidly increased when the O_2 flow was switched on at $\approx$ 190 s and decreased rapidly when the O_2 flow was switched off $\approx$ 380 s. These findings are similar to those shown in figure 5.5 using APMS, however, the magnitude of the I_F/I_{Ar} variation was much less than that observed with APMS. [F] increased by a factor of $\approx$ 60 as shown by APMS whereas [F] detected using actinometry only showed an increase of $\approx$ 3 when O_2 was added to the discharge. The Ar 750 nm line intensity decreased by $\approx$ 30 % when O_2 was added to the discharge, the reason for this is not understood at present. Changes in the excitation rate constant caused by changes in the EEDF can be ignored as Langmuir probe measurements indicated no significant change in the EEDF, n_e or T_{eff} when O_2 was added to the discharge. Such discrepancy between relative [F] measured with actinometry and APMS is due to a significant dissociative excitation contribution since the excitation dynamics remain unaffected over the conditions explored. It can be concluded that the classic actinometry model for detection of relative [F] was unreliable over the conditions explored in this work. The use of an adapted actinometry model

which accounts for dissociative excitation is clearly required.

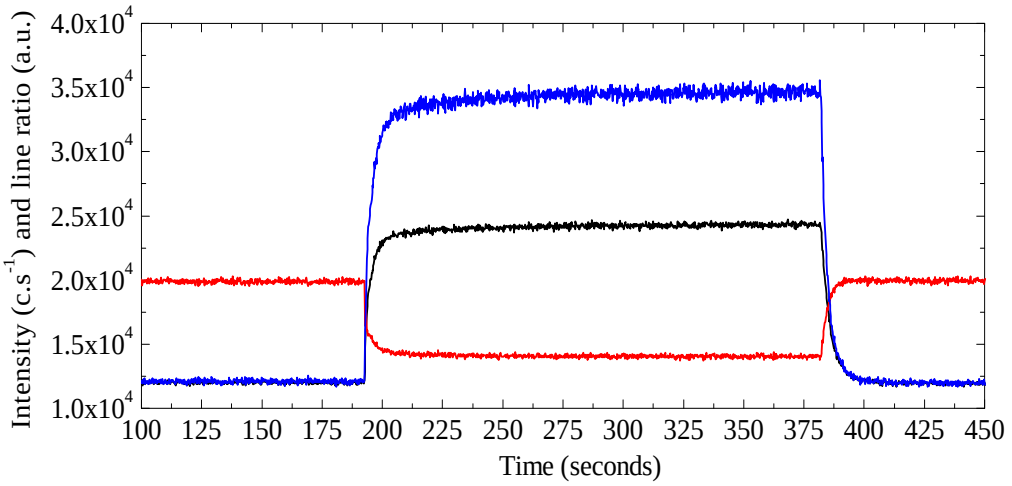

Figure 5.8: Time evolution of I_{F} (black), I_{Ar} (red) and $I_{\mathrm{F}}/I_{\mathrm{Ar}}$ (blue). Between 100 - 190 s and 380 - 500 s was pure SF_6/Ar (95/5%) plasma and between 190 - 380 s was an SF_6/O_2/Ar (85/10/5%) plasma. The power and pressure was kept constant at 500 W and 60 mTorr respectively.

This chapter reports on the use of appearance potential mass spectrometry for the detection of [F] in SF_6/Ar and SF_6/O_2/Ar plasma. It was shown that an SF_6/Ar plasma was weakly dissociated in comparison to an SF_6/O_2/Ar plasma. The presence of O_2 in the feedstock dramatically enhanced the concentration of atomic fluorine in an SF_6 dominated plasma. [F] increased by a factor of ≈ 60 when O_2 was added to an SF_6 plasma. The actinometric signal (which is also used to monitor changes in [F]) also showed an enhanced [F] as O_2 was added to an SF_6 plasma, however, only a 3 fold increase was observed. Therefore, the fluorine actinometric signal was found to be unreliable for monitoring relative changes in [F] under the conditions explored in this work.

CHAPTER 6

Conclusion

This thesis reports on the investigation of a parallel-plate (asymmetric) capacitively-coupled plasma (CCP) operated at 13.56 MHz. Important plasma parameters and plasma phenomenon were investigated for various plasma operating conditions with the use of well established plasma diagnostic techniques such as two-photon laser-induced fluorescence spectroscopy (TALIF), appearance potential mass spectrometry (APMS), optical actinometry, Langmuir and hairpin probes. The plasma investigated in this work contained gases that are typically found in processing plasmas within industry; these are O_2, SF_6, Ar and various mixtures of each. These techniques were used to investigate parameters and processes relevant for plasma etching and process control; an example of these are reactive species concentration i.e. [F] and [O] and key processes which influence the density of these reactive species i.e. electron impact dissociation and surface chemistry. The applicability of acti-

nometry for monitoring [F] and [O] was examined and benchmarked against more reliable methods; this technique has practical qualities for industrial use.

Absolute atomic oxygen density measured with TALIF showed an abrupt increase (five-fold) upon adding 5 - 10 % SF_6 to the feedstock. This increase was attributed to two key processes: an increase in the rate of dissociation of oxygen molecules and a decrease in the wall loss rate for oxygen atoms due to fluorination of the reactor surfaces. Langmuir probe measurements showed that the effective electron temperature varied from approximately 1 to 8 eV as the plasma became more electronegative with increasing SF_6 content. Consequently the radical production rate increased by over a factor of three due to this large shift in the effective electron temperature. The reactor walls were fluorinated by running O_2/SF_6 plasma, it was found that relative [O] after the fluorination process was over three times higher than a reference [O] measured in O_2 dominated plasma. This verified that fluorination of the reactor walls was partly responsible for the five-fold increase of [O] when O_2 plasma was diluted with SF_6.

CCP can exist in various modes which are defined by dominant electron heating mechanisms. These are the stochastic, α and γ modes and are significantly influenced by the discharge operating conditions such as power, pressure and gas. Transitions in the discharge mode has profound effects on the spatial dependence of the electron heating and ionization rates and also the electron temperature and density, which in turn, governs two key processes in plasma etching i.e. chemical reaction rates and ion transport to the driven electrode. A Langmuir probe was used to measure the electron energy probability function (EEPF), electron density (n_e), and the effective electron temperature (T_{eff}) in the axial and radial center of a CCP. The

objectives was to investigate electron heating mechanisms in O_2 plasma such as the $\alpha - \gamma$ mode transition and the collisionless-collisional heating mode transition. Upon increasing the applied power to an O_2 plasma operated at 100 mTorr; the EEPF evolved from a Druyvesteyn distribution characterized by a high T_{eff} (6.53 eV) to a distinctly bi-Maxwellian distribution characterized by a low T_{eff} (0.80 eV). A rapid decrease of T_{eff} and increase in n_e was observed as the power increased from 10 - 100 W. These findings were attributed to the $\alpha - \gamma$ mode transition. This occurs when secondary electrons become important in sustaining the discharge (γ mode), the switch from the α mode (ohmic) into the γ mode dramatically effects the ionization balance and various electron plasma parameters (EEPF, n_e and T_{eff}). A similar transition was observed in Ar plasma operated at 100 mTorr. Although, some differences to the same mode transition in O_2 plasma was observed. Firstly, the threshold power for the γ mode was 50 W in O_2 plasma whereas a lower threshold of 20 W was observed in Ar plasma. Secondly, collisional heating of low energy electrons was more significant in the γ mode of Ar plasma when compared to O_2 plasma in the same mode. This was apparent based on the comparison of the EEPFs for a given power and pressure in each plasma, the EEPF in Ar plasma was characterized by a Druyvesteyn distribution with a higher low energy electron temperature than in O_2 plasma. Also, T_{eff} in Ar plasma in the α mode was lower by $\approx$ 2 - 3 eV compared to the α mode of an O_2 plasma. The most likely reason for this is due to a lower n_e in O_2 plasma at low powers, and thus higher rf electric 'heating' field since $E \propto n_e^{-1}$.

Unusual behavior with the electron kinetics was observed whilst investigating the pressure evolution of the EEPF and T_{eff} for a constant applied power of 30 W. Initially, the ionizing tail of the EEPF decreased as the pressure was increased (10 - 70 mTorr) which is consistent with the inverse relationship

between the ionization rate constant and the neutral gas density (particle balance equation). However, the ionizing tail of the EEPF increased significantly and extended out towards higher energies as the pressure was increased greater than 70 mTorr. Consequently, the ionization rate constant varied by several orders of magnitude over the pressure range of 100 - 400 mTorr. This unexpected behavior is not clearly understood at present and requires further analysis.

The pressure evolution of the EEPF, n_e and T_{eff} was also examined at a higher applied power of 200 W. In this case, the $k_{ion} \propto (n_g d_{eff})^{-1}$ dependence was satisfied for a wider range of pressures (10 - 200 mTorr) compared to the same investigation at 30 W. Low energy electrons were heated as the pressure increased to 400 mTorr and consequently T_{eff} increased. A significant enhancement of the EEPF tail and thus, ionization rate constant was observed at 600 mTorr which again is contrary to the expected relationship given by the particle balance. The surprising presence of hot electrons in the moderate to high pressure regime for both powers investigated is an interesting but poorly understood observation. One possibility is that super-elastic collisions is responsible for the generation of these hot electrons. Super-elastic collisions are known to dramatically effect the tail on the EEPF and also produce structure on the electron energy distribution. Such structure on the EEPF was observed in the present study.

APMS was used to investigate the variation of atomic fluorine density for various operating conditions such as applied power (50 - 300 W), pressure (20 and 40 mTorr) and gas mixture. The applicability of actinometry for relative [F] detection i.e. $I_{\mathrm{F}}/I_{\mathrm{Ar}}$ was also investigated and compared to [F] determined with APMS. It was found that the dissociation fraction varied from 2.9×10^{-4} - 2.1×10^{-3} over a power range of 50 - 300 W in $SF_6/O_2/Ar$

plasma. The dissociation fraction was over 22 times higher in $SF_6/O_2/Ar$ plasma (40 mTorr) compared to SF_6/Ar plasma (20 mTorr). The time variation of the F^+ signal (m/e =19) was monitored with and without O_2 in the feedstock. The F^+ signal varied by up to a factor of 60 depending if O_2 was present in the feedstock. However, actinometry did not predict this significant enhancement of [F] when O_2 was added to an SF_6 plasma as I_F/I_{Ar} increased by only a factor of ≈ 3. No change in the electron kinetics was observed due to the addition of O_2 to the feedstock, therefore such a dramatic discrepancy between these atomic fluorine detection methods is due to a significant dissociative excitation contribution to the emission at 703 nm. In addition, actinometry predicted only a two fold increase in [F] while absolute [F] increased a factor of 10 over a given power range in a $SF_6/O_2/Ar$ plasma operated at 40 mTorr. The discrepancy is due to a variation of the EEDF and proportionality constant (K) with increasing power and also by a dissociative excitation contribution to the emission at 703 nm.

The possibility of implementing actinometry as a sensor for real-time, closed-loop control within industry is an interesting concept particularly due to the practical advantage it has over alternative technique such as TALIF and APMS. However, it was shown in this work that actinometry is unreliable for certain conditions and requires careful interpretation as a method for monitoring changes in radical densities. Finally, the use of experimental data is often used to benchmark various theoretical models such as global models [73]. While the use of global models can also be useful in understanding underlying physics of plasma aided phenomena. The author of this thesis would welcome any comparisons of findings reported in this thesis to theoretical models.

Bibliography

[1] G. Cunge, D. Vempaire, R. Ramos, M. Touzeau, O. Joubert, P. Bodard, and N. Sadeghi, "Radical surface interactions in industrial silicon plasma etch reactors," *Plasma Sources Science and Technology*, vol. 19, no. 3, p. 034017, 2010.

[2] G. Cunge, N. Sadeghi, and R. Ramos, "Influence of the reactor wall composition on radicals densities and total pressure in Cl_2 inductively coupled plasmas: I. without silicon etching," *Journal of Applied Physics*, vol. 102, no. 9, pp. 093305–093305–11, 2007.

[3] M. Lieberman and A. Lichtenberg, *Principles of Plasma Discharges and Materials Processing*. John Willey & Sons, Inc., 1994.

[4] N. R. Rueger, J. J. Beulens, M. Schaepkens, M. F. Doemling, J. M. Mirza, T. E. F. M. Standaert, and G. S. Oehrlein, "Role of steady state fluorocarbon films in the etching of silicon dioxide using CHF_3 in an

inductively coupled plasma reactor," *Journal of Vacuum Science and Technology A*, vol. 15, no. 4, 1997.

[5] J. W. Coburn and H. F. Winters, "Ion and electron assisted gas-surface chemistry an important effect in plasma etching," *Journal of Applied Physics*, vol. 50, no. 5, 1979.

[6] J. W. Coburn and H. F. Winters, "Plasma etching - a discussion of mechanisms," *Journal of Vacuum Science and Technology*, vol. 16, no. 2, 1979.

[7] V. A. Godyak, R. B. Piejak, and B. M. Alexandrovich, "Measurement of electron energy distribution in low-pressure rf discharges," *Plasma Sources Science and Technology*, vol. 1, no. 1, p. 36, 1992.

[8] V. Lisovskiy and V. Yegorenkov, "Alpha - gamma transition in rf capacitive discharge in low-pressure oxygen," *Vacuum*, vol. 74, no. 1, pp. 19 – 28, 2004.

[9] M. M. Turner, "Collisionless electron heating in an inductively coupled discharge," *Phys. Rev. Lett.*, vol. 71, pp. 1844–1847, Sep 1993.

[10] M. M. Turner, "Pressure heating of electrons in capacitively coupled rf discharges," *Phys. Rev. Lett.*, vol. 75, pp. 1312–1315, Aug 1995.

[11] M. M. Turner, "Collisionless heating in radio-frequency discharges: a review," *Journal of Physics D: Applied Physics*, vol. 42, no. 19, p. 194008, 2009.

[12] "Oxford Instruments." http://www.oxford-instruments.com/.

[13] K. Niemi, V. S. von der Gathen, and H. F. Dobele, "Absolute calibration of atomic density measurements by laser-induced fluorescence

spectroscopy with two-photon excitation," *Journal of Physics D: Applied Physics*, vol. 34, no. 15, p. 2330, 2001.

[14] H. F. Dobele, T. Mosbach, K. Niemi, and V. S. von der Gathen, "Laser-induced fluorescence measurements of absolute atomic densities concepts and limitations," *Plasma Sources Science and Technology*, vol. 14, no. 2, p. S31, 2005.

[15] H. F. Dobele, "Generation of coherent vuv radiation and its application to plasma diagnostics," *Plasma Sources Science and Technology*, vol. 4, no. 2, p. 224, 1995.

[16] R. Loudon, *The Quantum Theory of Light*. Oxford: Clarendon Press, second ed., 1983.

[17] A. D. Tserepi, E. Wurzberg, and T. A. Miller, "Two-photon-excited stimulated emission from atomic oxygen in rf plasmas detection and estimation of its threshold," *Chemical Physics Letters*, vol. 265, pp. 297 – 302, 1997.

[18] N. Sadeghi, D. W. Setser, A. Francis, U. Czarnetzki, and H. F. Dobele, "Quenching rate constants for reactions of $Ar(4p[1/2]_0$,$4p[1/2]_0$,$4p[3/2]_2$, and $4p[5/2]_2)$ atoms with 22 reagent gases," *The Journal of Chemical Physics*, vol. 115, no. 7, 2001.

[19] J. Amorim, G. Baravian, and J. Jolly, "Laser-induced resonance fluorescence as a diagnostic technique in non-thermal equilibrium plasmas," *Journal of Physics D: Applied Physics*, vol. 33, no. 9, p. R51, 2000.

[20] J. Amorim, G. Baravian, M. Touzeau, and J. Jolly, "Two photon laser

induced fluorescence and amplified spontaneous emission atom concentration measurements in O_2 and H_2 discharges," *Journal of Applied Physics*, vol. 76, pp. 1487–1493, Aug 1994.

[21] A. Goehlich, T. Kawetzki, and H. F. Dobele, "On absolute calibration with xenon of laser diagnostic methods based on two-photon absorption," *The Journal of Chemical Physics*, vol. 108, no. 22, 1998.

[22] K. Niemi, V. S. von der Gathen, and H. F. Dobele, "Absolute atomic oxygen density measurements by two-photon absorption laser-induced fluorescence spectroscopy in an rf-excited atmospheric pressure plasma jet," *Plasma Sources Science and Technology*, vol. 14, no. 2, p. 375, 2005.

[23] M. Geigl, S. Peters, O. Gabriel, B. Krames, and J. Meichsner, "Analysis and kinetics of transient species in electrode near plasma and plasma boundary sheath of rf plasmas in molecular gases," *Contributions to Plasma Physics*, vol. 45, no. 5-6, pp. 369–377, 2005.

[24] R. P. Saxon and Eichler, "Theoretical calculation of two-photon absorption cross sections in atomic oxygen," *Phys. Rev. A*, vol. 34, pp. 199–206, Jul 1986.

[25] K. Behringer and U. Fantz, "Spectroscopic diagnostics of glow discharge plasmas with non-maxwellian electron energy distributions," *Journal of Physics D: Applied Physics*, vol. 27, no. 10, p. 2128, 1994.

[26] M. V. Malyshev and V. M. Donnelly, "Trace rare gases optical emission spectroscopy nonintrusive method for measuring electron temperatures in low-pressure, low-temperature plasmas," *Phys. Rev. E*, vol. 60, pp. 6016–6029, Nov 1999.

[27] H. R. Griem. Cambridge University Press, 1997.

[28] H. H. Yue, S. J. Qin, J. Wiseman, and A. Toprac, "Plasma etching endpoint detection using multiple wavelengths for small open-area wafers," *Journal of Vacuum Science and Technology A*, vol. 19, no. 1, 2001.

[29] J. Schulze, E. Schungel, Z. Donko, D. Luggenholscher, and U. Czarnetzki, "Phase resolved optical emission spectroscopy a non-intrusive diagnostic to study electron dynamics in capacitive radio frequency discharges," *Journal of Physics D: Applied Physics*, vol. 43, no. 12, p. 124016, 2010.

[30] J. W. Coburn and M. Chen, "Dependence of F atom density on pressure and flow rate in CF_4 glow discharges as determined by emission spectroscopy," *Journal of Vacuum Science and Technology*, vol. 18, no. 2, 1981.

[31] R. R. Laher and F. R. Gilmore, "Updated excitation and ionization cross sections for electron impact on atomic oxygen," *Journal of Physical and Chemical Reference Data*, vol. 19, no. 1, pp. 277–305, 1990.

[32] V. Puech and L. Torchin, "Collision cross sections and electron swarm parameters in argon," *Journal of Physics D: Applied Physics*, vol. 19, no. 12, p. 2309, 1986.

[33] M. B. Schulman, F. A. Sharpton, S. Chung, C. C. Lin, and L. W. Anderson, "Emission from oxygen atoms produced by electron-impact dissociative excitation of oxygen molecules," *Phys. Rev. A*, vol. 32, pp. 2100–2116, Oct 1985.

[34] Y. Kawai, K. Sasaki, and K. Kadota, "Comparison of the fluorine atom density measured by actinometry and vacuum ultraviolet absorption

spectroscopy," *Japanese Journal of Applied Physics*, vol. 36, no. 9A, p. L1261, 1997.

[35] "Horiba Jobin Yvon Instrument Response Corrections Technical Note 203 Optical Spectroscopy Diversion." http://www.horiba.com/.

[36] U. Fantz, "Basics of plasma spectroscopy," *Plasma Sources Science and Technology*, vol. 15, no. 4, p. S137, 2006.

[37] H. H. Gaigales A, Wang L and D. P, "Procedures for wavelength calibration and spectral response correction of CCD array spectrometers," *Journal of Research of the National Institute of Standards and Technology*, vol. 114, no. 4, p. 215, 2009.

[38] "Hiden analytical." http://www.hidenanalytical.com/.

[39] H. Singh, J. W. Coburn, and D. B. Graves, "Mass spectrometric detection of reactive neutral species: Beam-to-background ratio," *Journal of Vacuum Science and Technology A*, vol. 17, no. 5, 1999.

[40] H. Singh, J. W. Coburn, and D. B. Graves, "Appearance potential mass spectrometry discrimination of dissociative ionization products," *Journal of Vacuum Science and Technology A*, vol. 18, no. 2, pp. 299–305, 2000.

[41] S. Agarwal, G. W. W. Quax, M. C. M. van de Sanden, D. Maroudas, and E. S. Aydil, "Measurement of absolute radical densities in a plasma using modulated-beam line-of-sight threshold ionization mass spectrometry," *Journal of Vacuum Science and Technology A*, vol. 22, no. 1, 2004.

[42] J. Benedikt, A. Hecimovic, D. Ellerweg, and A. von Keudell, "Quadrupole mass spectrometry of reactive plasmas," *Journal of Physics D: Applied Physics*, vol. 45, no. 40, p. 403001, 2012.

[43] Y.-K. Kim and J.-P. Desclaux, "Ionization of carbon, nitrogen, and oxygen by electron impact," *Phys. Rev. A*, vol. 66, p. 012708, Jul 2002.

[44] Y. Itikawa, "Cross Sections for Electron Collisions with Nitrogen Molecules," *Journal of Physical and Chemical Reference Data*, vol. 35, p. 31, 2006.

[45] M. V. V. S. Rao and S. K. Srivastava, "Cross sections for the production of positive ions by electron impact on," *Journal of Physics B: Atomic, Molecular and Optical Physics*, vol. 29, no. 9, p. 1841, 1996.

[46] G. Herzberg and K. Huber, *Molecular spectra and molecular structure.* No. IV in Molecular Spectra and Molecular Structure, Van Nostrand, 1979.

[47] L. G. Christophorou and J. K. Olthoff, "Electron interactions with SF_6," *Journal of Physical and Chemical Reference Data*, vol. 29, no. 3, pp. 267–330, 2000.

[48] S. Kechkar, P. Swift, J. Conway, M. Turner, and S. Daniels, "Investigation of atomic oxygen density in a capacitively coupled O_2/SF_6 discharge using two photon absorption laser induced fluorescence spectroscopy and a langmuir probe," *Plasma Sources Science and Technology*, vol. 22, no. 4, p. 045013, 2013.

[49] C. E. Moore, *Atomic energy levels: as derived from the analyses of optical spectra; 2nd ed.* Washington, DC: US. Nat. Bureau Stand., 1971.

[50] T. R. Hayes, R. C. Wetzel, and R. S. Freund, "Absolute electron-impact-ionization cross-section measurements of the halogen atoms," *Phys. Rev. A*, vol. 35, pp. 578–584, Jan 1987.

[51] R. C. Wetzel, F. A. Baiocchi, T. R. Hayes, and R. S. Freund, "Absolute cross sections for electron-impact ionization of the rare-gas atoms by the fast-neutral-beam method," *Phys. Rev. A*, vol. 35, pp. 559–577, Jan 1987.

[52] H. C. Straub, P. Renault, B. G. Lindsay, K. A. Smith, and R. F. Stebbings, "Absolute partial cross sections for electron-impact ionization of H_2, N_2, and O_2 from threshold to 1000 ev," *Phys. Rev. A*, vol. 54, pp. 2146–2153, Sep 1996.

[53] J. Pulpytel, F. Arefi-Khonsari, and W. Morscheidt, "Threshold ionization mass spectrometry study of singlet molecular oxygen in the deposition of SnO_2 by PACVD," *Journal of Physics D: Applied Physics*, vol. 38, no. 9, p. 1390, 2005.

[54] V. A. Godyak, R. B. Piejak, and B. M. Alexandrovich, "Probe diagnostics of nonmaxwellian plasmas," *Journal of Applied Physics*, vol. 73, no. 8, 1993.

[55] C. Steinbruchel, "A new method for analyzing langmuir probe data and the determination of ion densities and etch yields in an etching plasma," *Journal of Vacuum Science Technology A*, vol. 8, no. 3, 1990.

[56] "Scientific Systems." http://www.scisys.com//.

[57] R. R. J. Gagn and A. Cantin, "Investigation of an rf plasma with symmetrical and asymmetrical electrostatic probes," *Journal of Applied Physics*, vol. 43, no. 6, 1972.

[58] N. S. J. Braithwaite, N. M. P. Benjamin, and J. E. Allen, "An electrostatic probe technique for RF plasma," *Journal of Physics E: Scientific Instruments*, vol. 20, no. 8, p. 1046, 1987.

[59] M. B. Hopkins, "Langmuir probe measurements in the gaseous electronics conference rf reference cell," *Journal of Reesearch of the National Institute of Standards and Technology*, vol. 100, pp. 415–425, July-August 1995.

[60] C. Deegan, "Characterisation of the heating mechanisms in a capacitively coupled argon rf discahrge.," *PhD Thesis, School of Physical Sciences, Dublin City University*, July 1999.

[61] R. B. Piejak, V. A. Godyak, R. Garner, B. M. Alexandrovich, and N. Sternberg, "The hairpin resonator: A plasma density measuring technique revisited," *Journal of Applied Physics*, vol. 95, no. 7, 2004.

[62] C. Gaman, "Mass-spectroscopy and modelling of hydrogen capacitive discharge," *PhD Thesis, School of Physical Sciences, Dublin City University*, June 2011.

[63] J. P. Booth, O. Joubert, J. Pelletier, and N. Sadeghi, "Oxygen atom actinometry reinvestigated comparison with absolute measurements by resonance absorption at 130 nm," *Journal of Applied Physics*, vol. 69, no. 2, 1991.

[64] G. Hancock and M. J. Toogood, "Laser-induced fluorescence of oxygen atoms in a plasma reactor," *Applied Physics Letters*, vol. 60, no. 1, 1992.

[65] R. E. Walkup, K. L. Saenger, and G. S. Selwyn, "Studies of atomic

oxygen in O_2 + CF_4 rf discharges by two photon laser-induced fluorescence and optical emission spectroscopy," *The Journal of Chemical Physics*, vol. 84, no. 5, 1986.

[66] J. P. Booth and N. Sadeghi, "Oxygen and fluorine atom kinetics in electron cyclotron resonance plasmas by time resolved actinometry," *Journal of Applied Physics*, vol. 70, no. 2, 1991.

[67] S. Gomez, P. G. Steen, and W. G. Graham, "Atomic oxygen surface loss coefficient measurements in a capacitive and inductive radio-frequency plasma," *Applied Physics Letters*, vol. 81, no. 1, 2002.

[68] E. J. H. Collart, J. A. G. Baggerman, and R. J. Visser, "On the role of atomic oxygen in the etching of organic polymers in a radio frequency oxygen discharge," *Journal of Applied Physics*, vol. 78, no. 1, 1995.

[69] A. D. Tserepi and T. A. Miller, "Spatially and temporally resolved absolute O atom concentrations in etching plasmas," *Journal of Applied Physics*, vol. 77, no. 2, 1995.

[70] M. W. Kiehlbauch and D. B. Graves, "Inductively coupled plasmas in oxygen: Modeling and experiment," *Journal of Vacuum Science Technology A*, vol. 21, no. 3, 2003.

[71] R. S. Pessoa, L. L. Tezani, H. S. Maciel, G. Petraconi, and M. Massi, "Study of SF_6 and SF_6/O_2 plasmas in a hollow cathode reactive ion etching reactor using langmuir probe and optical emission spectroscopy techniques," *Plasma Sources Science and Technology*, vol. 19, no. 2, p. 025013, 2010.

[72] J. L. Alexander, "Characterization of boron trichloride, sulfur hexafluoride, and boron trichloride/sulfur hexafluoride plasmas using langmuir

probe measurements," 2009. Copyright - ProQuest, UMI Dissertations Publishing 2009.

[73] A. Pateau, A. Rhallabi, M.-C. Fernandez, M. Boufnichel, and F. Roqueta, "Modeling of inductively coupled plasma $SF_6/O_2/Ar$ plasma discharge effect of O_2 on the plasma kinetic properties," *Journal of Vacuum Science and Technology A*, vol. 32, no. 2, p. 021303, 2014.

[74] M. V. Malyshev, V. M. Donnelly, A. Kornblit, and N. A. Ciampa, "Percent dissociation of Cl_2 in inductively coupled, chlorine-containing plasmas," *Journal of Applied Physics*, vol. 84, no. 1, 1998.

[75] K. J. Nordheden, K. Upadhyaya, Y. S. Lee, S. P. Gogineni, and M. Y. Kao, "GaAs etch rate enhancement with SF6 addition to BCl_3 plasmas," *Journal of The Electrochemical Society*, vol. 147, no. 10, pp. 3850–3852, 2000.

[76] P. J. Chantry and C. L. Chen, "Ionization and temperature dependent attachment cross section measurements in C_3F_8 and C_2H_3Cl.," *Journal of Chemical Physics*, vol. 90, no. 5, p. 2585, 1989.

[77] A. E. Belikov, O. V. Kusnetsov, and R. G. Sharafutdinov, "The rate of collisional quenching of .." *The Journal of Chemical Physics*, vol. 102, no. 7, 1995.

[78] M. B. Faist and R. B. Bernstein, "Computational study of elastic and electronically inelastic scattering of Br by ground state I atoms: Role of potential curve crossing," *The Journal of Chemical Physics*, vol. 64, no. 7, 1976.

[79] G. Dilecce, M. Capitelli, and S. De Benedictis, "Electron-energy distribution function measurements in capacitively coupled rf discharges," *Journal of Applied Physics*, vol. 69, pp. 121–128, Jan 1991.

[80] H. Singh and D. B. Graves, "Measurements of the electron energy distribution function in molecular gases in an inductively coupled plasma," *Journal of Applied Physics*, vol. 87, no. 9, 2000.

[81] D. Gahan, B. Dolinaj, and M. B. Hopkins, "Comparison of plasma parameters determined with a langmuir probe and with a retarding field energy analyzer," *Plasma Sources Science and Technology*, vol. 17, no. 3, p. 035026, 2008.

[82] S. E. Savas, "Observations of argon emission lines used for fluorine atom actinometry in low power rf discharges," *Applied Physics Letters*, vol. 48, no. 16, 1986.

[83] M. S. Brown, B. N. Ganguly, and A. Garscadden, "Resonance enhanced deactivation of argon 4p'$[1/2]^o$ state by atomic oxygen and its impact on actinometry," *Plasma Sources Science and Technology*, vol. 11, no. 2, p. 190, 2002.

[84] A. Melzer, R. Flohr, and A. Piel, "Comparison of probe measurements and emission spectroscopy in a radiofrequency discharge," *Plasma Sources Science and Technology*, vol. 4, no. 3, p. 424, 1995.

[85] V. A. Godyak, R. B. Piejak, and B. M. Alexandrovich, "Evolution of the electron-energy-distribution function during rf discharge transition to the high-voltage mode," *Phys. Rev. Lett.*, vol. 68, pp. 40–43, Jan 1992.

[86] C. M. Deegan, J. P. Goss, D. Vender, and M. B. Hopkins, "Measurement of the electron energy distribution function in an argon radio-frequency discharge in the γ mode," *Applied Physics Letters*, vol. 74, no. 14, 1999.

[87] V. A. Godyak and R. B. Piejak, "Abnormally low electron energy and heating-mode transition in a low-pressure argon rf discharge at 13.56 mhz," *Phys. Rev. Lett.*, vol. 65, pp. 996–999, Aug 1990.

[88] J. T. Gudmundsson, T. Kimura, and M. A. Lieberman, "Experimental studies of O_2/Ar plasma in a planar inductive discharge," *Plasma Sources Science and Technology*, vol. 8, no. 1, p. 22, 1999.

[89] J. T. Gudmundsson, A. M. Marakhtanov, K. K. Patel, V. P. Gopinath, and M. A. Lieberman, "On the plasma parameters of a planar inductive oxygen discharge," *Journal of Physics D: Applied Physics*, vol. 33, no. 11, p. 1323, 2000.

[90] M. Tuszewski, J. T. Scheuer, and J. A. Tobin, "Composition of the oxygen plasmas from two inductively coupled sources," *Journal of Vacuum Science Technology A*, vol. 13, no. 3, 1995.

[91] M. S. Barnes, J. C. Forster, and J. H. Keller, "Electron energy distribution function measurements in a planar inductive oxygen radio frequency glow discharge," *Applied Physics Letters*, vol. 62, no. 21, 1993.

[92] A. Schwabedissen, E. C. Benck, and J. R. Roberts, "Langmuir probe measurements in an inductively coupled plasma source," *Phys. Rev. E*, vol. 55, pp. 3450–3459, Mar 1997.

[93] M.-H. Lee, H.-C. Lee, and C.-W. Chung, "Comparison of pressure dependence of electron energy distributions in oxygen capacitively and inductively coupled plasmas," *Phys. Rev. E*, vol. 81, p. 046402, Apr 2010.

[94] J. Pulpytel, W. Morscheidt, and F. Arefi-Khonsari, "Probe diagnostics of argon-oxygen-tetramethyltin capacitively coupled plasmas for the deposition of tin oxide thin films," *Journal of Applied Physics*, vol. 101, no. 7, p. 073308, 2007.

[95] E. Abdel-Fattah, M. Bazavan, and H. Sugai, "Langmuir probe diagnostics of electron energy distributions with optical emission spectroscopy in capacitively coupled rf discharge in nitrogen," *Journal of Applied Physics*, vol. 110, no. 11, p. 113303, 2011.

[96] E. Abdel-Fattah and O. F. Farag, "Alpha to gamma mode transition in hydrogen capacitive radio-frequency discharge," *Canadian Journal of Physics*, vol. 91, no. 12, pp. 1062–1067, 2013.

[97] V. Vahedi and M. Surendra, "A monte carlo collision model for the particle-in-cell method: applications to argon and oxygen discharges," *Computer Physics Communications*, vol. 87, no. 12, pp. 179 – 198, 1995. Particle Simulation Methods.

[98] J. Scanlan, "Langmuir probe measurements in 13.56 MHz discharges," *PhD Thesis, School of Physical Sciences, Dublin City University*, September 1991.

[99] M. M. Turner, R. A. Doyle, and M. B. Hopkins, "Measured and simulated electron energy distribution functions in a low pressure radio

frequency discharge in argon," *Applied Physics Letters*, vol. 62, no. 25, 1993.

[100] M. M. Turner and M. B. Hopkins, "Anomalous sheath heating in a low pressure rf discharge in nitrogen," *Phys. Rev. Lett.*, vol. 69, pp. 3511–3514, Dec 1992.

[101] H. Li, "Measurements of electron energy distribution function and neutral gas temperature in an inductively coupled plasma.," *Masters Thesis, Department of Physics and Engineering Physics, University of Saskatchewan Saskatoon*, August 2006.

[102] C. M. O. Mahony, J. McFarland, P. G. Steen, and W. G. Graham, "Structure observed in measured electron energy distribution functions in capacitively coupled radio frequency hydrogen plasmas," *Applied Physics Letters*, vol. 75, no. 3, 1999.

[103] M. Capitelli, G. Colonna, O. D. Pascale, C. Gorse, K. Hassouni, and S. Longo, "Electron energy distribution functions and second kind collisions," *Plasma Sources Science and Technology*, vol. 18, no. 1, p. 014014, 2009.

[104] J. Amorim, J. Lino, J. Loureiro, M. Lima, and F. da Paixo, "Superelastic collisions of electrons with the c$\prod_u$ metastable state in hydrogen dc positive column," *Chemical Physics*, vol. 246, no. 13, pp. 275 – 282, 1999.

[105] V. Lisovskii, "Features of the - transition in a low-pressure rf argon discharge," *Technical Physics*, vol. 43, no. 5, pp. 526–534, 1998.

[106] A. Tserepi, W. Schwarzenbach, J. Derouard, and N. Sadeghi, "Kinetics of F atoms and fluorocarbon radicals studied by threshold ionization

mass spectrometry in a microwave CF_4 plasma," *Journal of Vacuum Science Technology A: Vacuum, Surfaces, and Films*, vol. 15, pp. 3120–3126, Nov 1997.

[107] R. J. M. M. Snijkers, J. F. Coulon, and G. Turban, "Mass spectrometric detection...," *Journal of Physics D: Applied Physics*, vol. 24, no. 7, p. 1098, 1991.

[108] J. Conway, S. Kechkar, N. O. Connor, C. Gaman, M. M. Turner, and S. Daniels, "Use of particle in cell simulations to improve the actinometry technique for determination of absolute atomic oxygen density," *Plasma Sources Science and Technology*, vol. 22, no. 4, p. 045004, 2013.

[109] V. Lisovskiy, J.-P. Booth, J. Jolly, S. Martins, K. Landry, D. Douai, V. Cassagne, and V. Yegorenkov, "Modes of rf capacitive discharge in low-pressure sulfur hexafluoride," *Journal of Physics D: Applied Physics*, vol. 40, no. 22, p. 6989, 2007.

[110] K. Ryan and I. Plumb, "A model for the etching of silicon in SF_6/O_2 plasmas," *Plasma Chemistry and Plasma Processing*, vol. 10, no. 2, pp. 207–229, 1990.

[111] K. A. Blanks, A. E. Tabor, and K. Becker, "Absolute cross sections for fluorine $3p \rightarrow 3s$ line emissions following single electron impact on NF_3, CF_4, and SF_6," *The Journal of Chemical Physics*, vol. 86, no. 9, 1987.

[112] M. L. Passow, J. T. P. Pender, M. L. Brake, K. T. Sung, Y. Liu, S. W. Pang, and M. E. Elta, "Relative fluorine concentrations in radio frequency/electron cyclotron resonance hybrid glow discharges," *Applied Physics Letters*, vol. 60, no. 7, 1992.

[113] P. Chabert, R. W. Boswell, and C. Davis, "Investigation of a SF_6 helicon plasma," *Journal of Vacuum Science Technology A*, vol. 16, no. 1, 1998.